Bayesian γ-ray Light Curve Analysis of TANAMI Sources

Masterarbeit aus der Physik

vorgelegt von

Christoph Bürkel

23. Januar 2015

Dr. Karl Remeis-Sternwarte Bamberg
Astronomisches Institut
Friedrich-Alexander-Universität
Erlangen-Nürnberg

1. Gutachter: Prof. Dr. Jörn Wilms
2. Gutachter: Prof. Dr. Matthias Kadler

Contents

Abstract

The method of Bayesian blocks was applied in order to determine variations and flares in light curves. Bayesian blocks are a statistical method to find variations in respect of the given errors. A routine for Poisson and Gaussian distributed data was implemented in *s-lang*.
The light curves for the analysis were derived from γ-ray observation with Fermi/LAT, a space telescope, which continuously observes active galactic nuclei (AGN). The source list for the analysis is based on the TANAMI source list and contains 55 sources that can be associated with the 2FGL-catalogue. In twenty sources Bayesian blocks were detected. In nine sources there are indications for short flares.
The results of the analysis show that the variability of the flux is in the most cases connected to the variability of the spectral properties. Some sources purvey hints for positive correlation between the flux and the spectral index. In some other sources there are signs for negative correlation.
In regard of the large number of upper limits in some light curve a workaround is presented that allows for a better picture of these sources. The results of the spectral analysis can be used to recalculate the light curves to get a more realistic picture of the real flux evolution.
In this thesis it has been demonstrated that the method works well with γ-ray light curves and for further studies the method of Bayesian blocks can be applied to other wavelengths to get a more detailed picture of the variability of AGN.

Zusammenfassung

In dieser Masterarbeit wird die Methode der bayesischen Blöcke angewandt um Varationen in Lichtkurven zu finden. Die bayesischen Blöcke sind eine statistische Methode, die Variation unter der Berücksichtigung der Fehler der Daten bestimmen kann. Ein Routine für Poisson- und gaußverteilte Daten wurde in *s-lang* implementiert.
Die Lichtkurven für die Analyse wurden aus Daten des Weltraumteleskopes Fermi/LAT berechnet. Das Fermi-Teleskop misst kontinuierlich die Gamma-Strahlung von kosmischen Objekten, wie Aktive Galaxienkernen (AGN). Die TANAMI Quellliste bildet die Grundlage für die analysierten Quellen. 55 Quellen der TANAMI liste konnte eine Quelle im 2FGL-Katalogue zugeordnet werden, von diesen Quellen besitzen 20 bayesische Blöcke. In 9 dieser Quellen wurde außerdem Hinweise für kurze Gamma-Strahlungsausbrüche gefunden.
Das Ergebnis der Analyse zeigt neben der Flussvariabilität, auch eine Variation der spektralen Komponenten. Es wurden Hinweise auf einen Zusammenhang zwischen Fluss und spektralem Index in einigen Quellen gefunden. Manche zeigen eine positive, andere jedoch eine negative Korrelation.
Wegen der großen Anzahl von Upper-Limits in einigen Quellen, ein Weg vorgeschlagen, wie man dieses Problem lösen kann, um ein besseres Verständnis dieser Quellen zuerhalten. Die spektralen Ergebnisse können weiterhin für eine Neuberechnung der Lichtkurven verwendet werden, um ein realistischeres Bild des Flussverlaufes zu erhalten.
In dieser Arbeit wird demonstriert, dass die Methode der bayesischen Blöcke für Fermi-Lichtkurven funktioniert und für weitere Untersuchungen benutzt werden kann, um ein besseres Verständnis der Aktiven Galaxienkerne zu bekommen.

1 Introduction

1.1 Active Galactic Nuclei

The first active galactic nucleus (AGN) was discovered in 1908 by Edward Fath (1909). He discovered optical emission lines in a spiral galaxies. These lines are an evidence for hot ionised gas in those galaxies. In 1918 Curtis (1918) discovered the first extra galactic jet in the elliptical galaxy M87. Carl Seyfert discovered galaxies with a very bright point like source, which look like a bright single star in the centre (Seyfert, 1943). The detailed study of these objects showed that the galaxies have strong emission lines in their central region, like the galaxies of Fath. He discovered two different types of those objects, some objects show broad and narrow emission lines and other objects only showed narrow lines. A few years later in the 1960's strong radio emission of quasi stellar objects (QSO) was detected (Matthews and Sandage, 1963). The first proposed explanations for this strong radio emission requested a very large mass up to $10^8 M_\odot$ in the centre of these objects (Woltjer, 1959). The first determination of the red shift showed that these objects a very far away, $z = 0.158$ (~ 2.2 billion light years)(Schmidt, 1963). That a super massive black hole (SMBH) which accretes matter was proposed by Salpeter (1964) as an explanation for such a high point like central mass. According to this the jet in M87 could be explained too. Later the objects with an active core were combined to the class of AGN (Antonucci, 1993).
With the investigations of the 3C[1] sources more jets were found in sources with bright and faint radio emission, even such galaxies Seyfert discovered (Boettcher, 2012). It became clear that these objects are just the same astronomical objects. But the sub types we can see on the sky just depends on the angle we look at them.

1.1.1 General Properties

All different AGN types are assumed to be one picture of the same phenomenon(Antonucci, 1993). The general mechanism of AGN is accretion, the most effective way to gain energy in the universe. A super massive black hole (SMBH) in the centre of AGN with a mass of around $10^6\, M_\odot$ up to $10^9\, M_\odot$ accretes matter and powers the whole system. The luminosity of an AGN is directly related to the mass of the SMBH and the maximum luminosity is a result of the equation of radiation pressure and gravitation. The maximum luminosity is given by the Eddington luminosity

$$L_{\mathrm{Edd}} = \frac{4\pi G M m_p c}{\sigma_T} \simeq 1.3 \cdot 10^{38} \frac{M}{M_\odot}\,\mathrm{erg\,s^{-1}} \tag{1.1}$$

where M is the mass of the SMBH, $M_\odot$ the mass of the sun. For a typical SMBH of $10^6\, M_\odot$ a maximum luminosity of $L = 1.3 \cdot 10^{44}\,\mathrm{erg\,s^{-1}} = 10^{11} L_\odot$ can be expected. Compared to a normal galaxy with around 10^{11} stars, the AGN core is as bright as the whole normal galaxy.

The SMBH is surrounded by an accretion disk with radius of around $\sim 10^{-3}\,\mathrm{pc}$ (Fig. 1). In the same plane in a distance of $\sim 1 - 10\,\mathrm{pc}$ a dusty torus of colder material is formed around the central part. Perpendicular to the plane of the accretion disk a collimated jet with relativistic outflow material can be seen in radio-loud AGN. After long investigation of X-ray

[1] Third Cambridge Catalogue of Radio Sources

observation, the conclusion came up that the AGN torus is made of clumpy structures, like dust clouds. This was discovered by time variable absorption due to eclipses when a cloud moves through the line of sight (Markowitz et al., 2014). At a distance of $0.01 - 0.1\,\mathrm{pc}$ a dense and fast rotating medium form the broad line region (BLR) followed by the narrow line region (NLR, $r \sim 100 - 1000\,\mathrm{pc}$) of low density medium.
The jet inclination has a big influence of the system in the radio loud AGN case. Concerning relativistic boosting the high relativistic outflows of blazars appear as one-sided jets. These jets can outshine the whole emission of the system, therefore the other parts of an AGN are not visible.

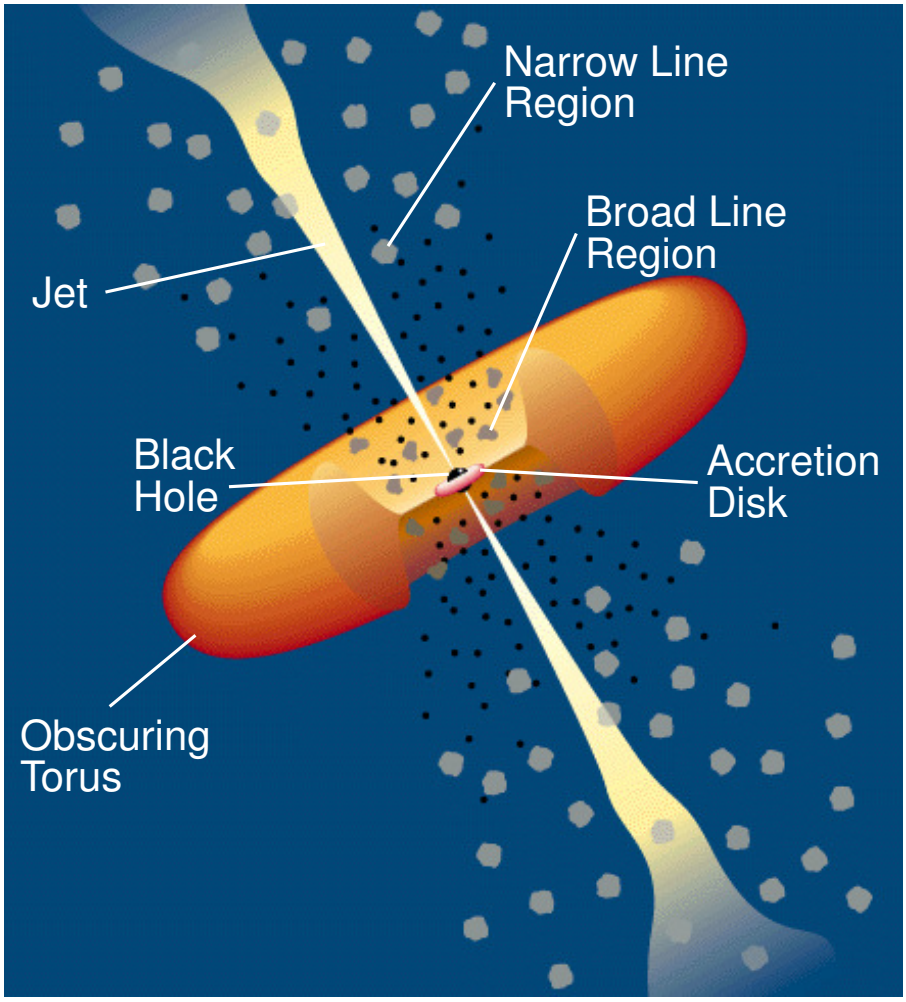

Figure 1: Illustration of the unified AGN model (Urry and Padovani, 1995).

1.1.2 Subtypes of AGN

All subtypes are the result of the same phenomenon (Antonucci, 1993). The AGN can separated in two major categories radio loud and radio quiet AGN. The separation follows,

$$R_{r-o} = \frac{F(6\,\mathrm{GHz})}{F(4400\,\mathring{A})} \tag{1.2}$$

Radio loud AGN show a ratio of $R_{r-o} = 10 - 1000$ and features jets, whereas radio quiet AGN have a ratio $R_{r-o} \leq 1$ and typically show just weak jets.
Beside this the AGN can additionally be separated in certain categories which depend on the viewing angle. The subtypes are listed in Tab. 1 and briefly explained in the following after Peterson (1997), Krolik (1999) and Karttunen (2007).

Table 1: Unification scheme (Urry and Padovani, 1995)

inclination	**radio quiet**	**radio loud**
small	Seyfert I	BL Lac
	radio-quite quasar	radio-loud quasar
great	Seyfert II	NLRG (FR I & II)
	radio-quite quasar	radio-loud quasar

Radio Quiet AGN

Seyfert Galaxies Seyfert galaxies appear just like normal spiral galaxies however with a very bright central core. This core shows strong optical emission lines. These emission line also features some lines of highly ionized ionized elements. The Seyfert galaxies can also be divided into two different classes, Seyfert I and Seyfert II galaxies (Khachikian and Weedman, 1974).The selection criteria is related to shape of the emission lines. In Seyfert I galaxies AGN system is seen face on and broad and narrow emission lines can be detected, in contrast in Seyfert II galaxies only the torus is visible and show only narrow lines, which are forbidden. This is caused by the inclination of the AGN system. A comparison between the two spectral types is shown in Fig. 2. Through the Doppler-shift of broad lines the velocity of the emission region can be determined to $10^3 - 10^4$ km/s. The intermediate states between Seyfert I and II are often classified as Seyfert 1.5 or Seyfert 1.7.

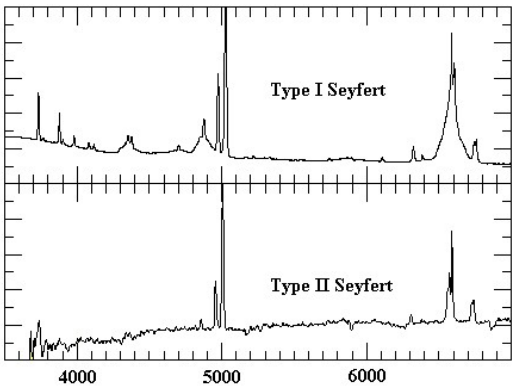

Figure 2: Optical spectra of a Seyfert I (above) and a Seyfert II galaxy (blow). Seyfert I show broad and narrow line, Seyfert II only narrow lines. (Credit: `http://www.uni.edu/morgans/astro/course/Notes/section3/seyfertspectra.gif`)

QSO (Radio Quiet) Quasi stellar objects are also called quasars. They are among the brightest sources in the sky. Their bolometric luminosity can reach an absolute magnitude of $M = -21.5\,\mathrm{mag}$. The appearance in the optical is nearly the same like the Seyfert galaxies, they also show a optical spectrum featured emission lines. The difference between Seyfert galaxies and quasars is that the surrounding host galaxy of the AGN is not visible for a quasar caused by the bright central region. Hence, they got the name QSO. There are also radio loud QSO's on the sky but this population is smaller than the radio quiet QSO's.

Radio Loud AGN

Radio Galaxies Radio galaxies are the counter part of the Seyfert galaxies in the radio loud regime. These galaxies features a jet in the radio. Fanaroff and Riley (1974) classified two different types of these galaxies, Fanaroff-Riley I (FR I) and Fanaroff-Riley II (FR II) which is the more luminous type. FR I types show a compact radio emission near the core region, in contrast the FR II types the emission is dominant in the radio lobes. Similar to the Seyfert galaxies both FR types can show broad optical emission lines, then they are called broad-line radio galaxies (BLRG) and in the case if they show only narrow optical lines, then they are named narrow-line radio galaxies (NLRG).

Blazars The class of blazars consists of two different AGN, *BL Lac objects* and *flat spectrum radio-quasars (FSRQ)* the companion to the radio quiet quasars. In most blazars the host galaxy is not detected. In the spectrum no optical lines can be found and the broadband spectrum is dominated by non-thermal radiation. Blazars are the brightest subclass of AGN and emitting light over the hole electro-magnetic spectrum from radio up to very high γ-ray radiation. They are very variable in all wavelength and the radiation is often highly polarized.

1.2 Broadband emission

Multiwavelength observations showed that an AGN emits photons in a broad energy range, from radio to γ-ray and even very high γ-rays. Especially the jets are a very bright source of the broad non-thermal radiation which is dominated by synchrotron radiation and the inverse Compton effect. In the following the theoretical background of these processes is briefly summarised and combined to the spectral energy distribution of an AGN.

1.2.1 Low Energy Emission

The main component of the non-thermal radiation in the lower energy regime from radio to X-rays the synchrotron radiation. A charged particle deflected in a magnetic field emits photons by the synchrotron effect. This effect can also be understood in general as the Compton scattering off virtual photons from the magnetic field. The following brief description of the derivation of the resulting spectrum can be found in detail in Blumenthal and Gould (1970). The energy loss of an electron, for other charged particles the calculation is nearly the same, by synchrotron interaction can be described as

$$\left(\frac{\mathrm{d}E_e}{\mathrm{d}t}\right)_{\mathrm{Sy}} = -\frac{2r_e^2}{3c}\gamma^2 B^2 v^2 \sin^2\theta \tag{1.3}$$

with the classical electron radius r_e, the Lorentz factor γ, the velocity v, the magnetic flux density B and the angle θ between the magnetic field and the direction of motion of the electron.

With the definition of a critical frequency

$$\nu_c = \frac{3eB\gamma^2}{4\pi m_e c} \sin\theta \tag{1.4}$$

we can derive an equation for the spectral energy density with the assumption that the electron energies are isotropically distributed:

$$\left(\frac{\mathrm{d}W}{\mathrm{d}\nu \mathrm{d}t}\right)_{\mathrm{Sy}} = \frac{4\pi k e^3 B^{(p+1)/2}}{m_e c^2} \left(\frac{3e}{4\pi m_e c}\right)^{(p-1)/2} a(p)\nu^{-(p-1)/2} \tag{1.5}$$

If the constant terms are neglected the dependence of the frequency becomes visible

$$\left(\frac{\mathrm{d}W}{\mathrm{d}\nu \mathrm{d}t}\right)_{\mathrm{Sy}} \propto \nu^{-(p-1)/2} \tag{1.6}$$

with spectral index $\alpha = \frac{1-p}{2}$ for the index p of the particle energy distribution.
If the seed particles are highly relativistic the emitted photons are boosted in a cone with an opening angle $\alpha_{\mathrm{boost}} \simeq \gamma^{-1}$. The whole synchrotron effect is very efficient for light particles like electrons and less efficient fore much heavier ones like protons, concerning the mass.
Low energy synchrotron photons can be absorbed by their synchrotron emitting parent electrons, this effect is called Synchrotron self-absorption. The absorption coefficient a can be expressed as (Boettcher, 2012)

$$a = -\frac{(p+2)}{18\pi m\nu^2} \left(\frac{3q}{4\pi mc}\right)^{p-2/2} \left(\frac{q^2}{mc^2}\right) B^{p+2/2}\nu^{p+4/2} \tag{1.7}$$

for a power law distribution of particles in a magnetic field. The resulting spectral shape depends on the photon energy, below a certain critical frequency the spectrum changes from $S_\nu \propto \nu^{-(p-1)/2}$ at higher frequencies to $S_\nu \propto B^{-1/2}\nu^{5/2}$ at lower frequencies.

1.2.2 High Energy Emission

In the high energy regime two different mechanism take place in the photon production. First the inverse Compton effect. The Compton effect describes photon scattering off low-energy particles, e.g. electrons in an atomic shell (Compton, 1923). The inverse Compton (IC) effect is the exact opposite of the Compton effect. It is the scattering of highly relativistic charged particles off low-energy photons. Both effects are related by a Lorentz transformation. In the AGN system there are several seed photons fields for the IC scattering, e.g. optical photons from the thermal emission of the accretion disk or radio photons from the synchrotron emission.

The same calculation as that done for the synchrotron radiation be applied to determine the spectral shape of the IC spectrum. Like the synchrotron spectrum the IC spectrum has two different parts. In the low energy-γ-ray regime the spectrum rises linear with frequency $S_\nu \propto \nu$ and after the maximum which is defined by the maximum energy gaining of the photons, the spectrum change to a power law $S_\nu \propto \nu^{-(p-1)/2}$ for high energy γ-rays (Blumenthal and Gould, 1970).
Beside external photon fields there is another photon field which originates from the synchrotron photons. If the synchrotron photon field is dense enough the parent seed particles can interact with these photons. The effect is called the synchrotron-self Compton effect (Marscher and Gear, 1985).

The second mechanism is the hadronic production of γ-rays. Since the AGN are candidates for ultra-high cosmic rays, hadrons have to be a part in the AGN system. High energy protons can reach the threshold for secondary particle production (Mannheim et al., 1992). The high frequency spectrum could be explained by the electromagnetic cascade produced of the decay of hadronic particles. These hadronic particles originates of proton-photon interactions in the jet. The interaction are typically photon-pion production $p + \gamma \rightarrow p + \pi^0$, $p + \gamma \rightarrow n + \pi^+$ and the Bethe-Heitler process of electron-positron pair production $p + \gamma \rightarrow p + e^+ + e^-$ (Bethe, 1934).
Photon-pion production also produces neutrinos through pion decay, if they are detected in AGN that would be an evidence for hadron emission in AGN jets.

1.2.3 Broadband spectral energy distribution

The different components like accretion disk, torus and jet form the overall spectrum of an AGN. The broadband spectrum is the result of the contribution of the different emission components through inclination and relativistic boosting effects. Nevertheless in radio-loud objects the synchrotron is the dominant part of the spectrum for the lower energies. The dominant part at higher energies is not known and an actual field of research. Due to multiwavelength monitoring of AGN the broadband spectra and its long term evolution is measured and provide the possibility to study the emission mechanisms and correlation of the spectral components in detail.

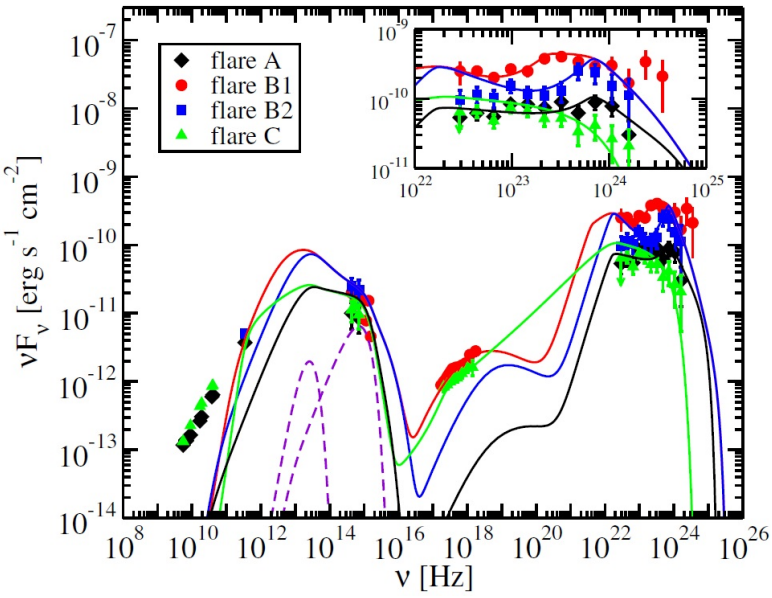

Figure 3: Example SED for four different flares detected from PKS 1424-418. The first hump dominated by synchrotron radiation and the second hump might be a composition of IC, SSC and hadronic emission.(Buson et al., 2014)

The broadband SED of blazars show a double-humped structure (Fig. 3). The maximum of the first hump peaks in the optical and is associated with the synchrotron emission. The second hump peaks in the in the X-rays or γ-rays due to the IC and hadronic emission. It is unclear which process is the dominate one in the high energy regime, several leptonic, hadronic and lepto-hadronic models can explain the shape of the second hump (Mücke and Protheroe, 2001).

1.2.4 Broadband variability

The features of blazars are their high variability throughout the spectrum and the correlation between different wavebands, e.g. radio and γ-rays. The variability time scales range from short variations of hours and days to longer variations of weeks to month, depends on the observed frequency band.

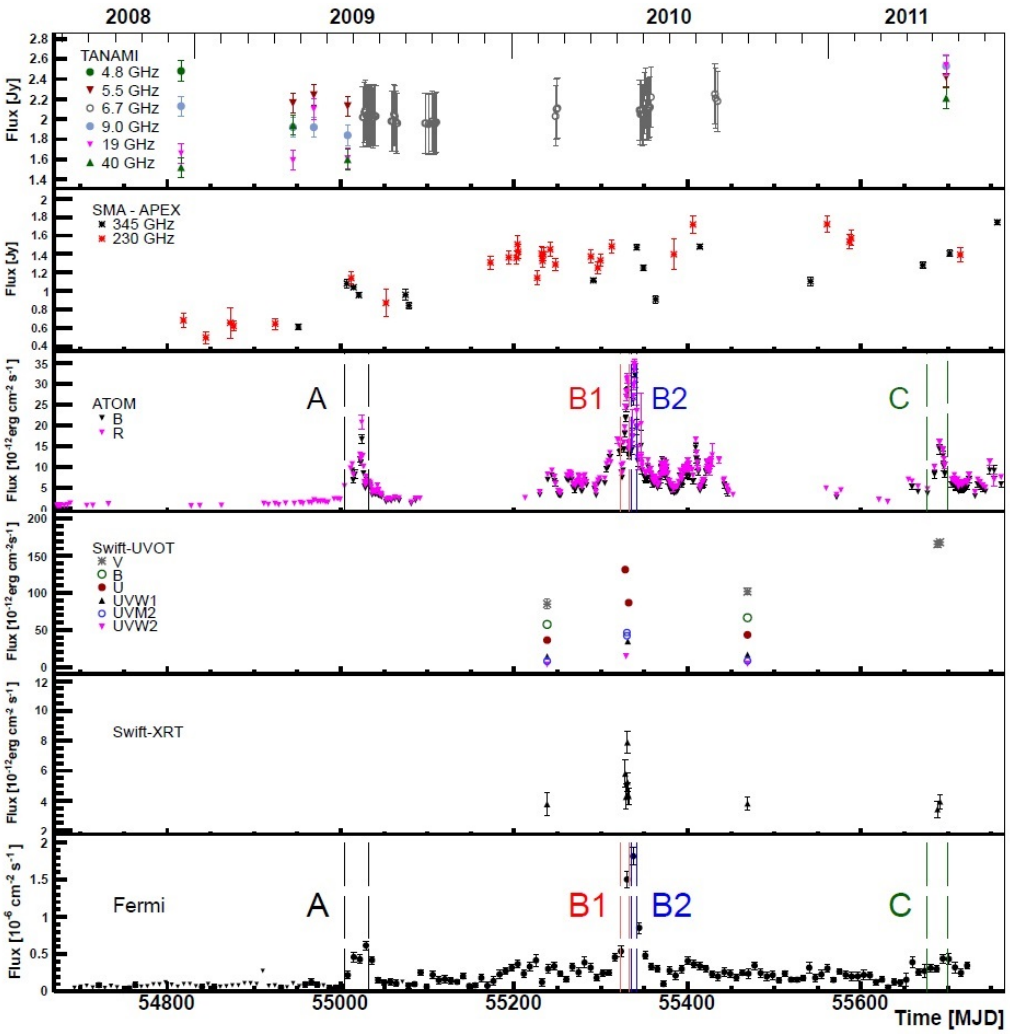

Figure 4: Multiwavelength light curve of PKS 1424-418. From top to bottom: The first panel displays radio data from TANAMI in several frequencies, the second panel displays radio data from SMA and APEX, the third panel displays optical data from ATOM in the R and B band, the forth panel displays UV data from Swift-UVOT, the fifth panel displays X-ray data from Swift-XRT and the sixth panel displays data from Fermi-LAT. Vertical lines denote prominent outbursts.(Buson et al., 2014)

The study of variation of these objects in different wavebands is one key to understand more of the complex emission mechanism and the leading components. The search for and the detection of variation is an important object of study. The interesting part of these variation is if these are just statistical variations or variations of the source itself. In following sections a modern ansatz is presented (Sec. 2.2) and the analyses can be done with it (Sec. 3 and Sec. 4).

2 Scientific Background

2.1 *Fermi*

The *Fermi* γ-ray Space Telescope is a γ-ray satellite launched on June the 11$^{\text{th}}$ 2008 by NASA (`http://fermi.gsfc.nasa.gov/`). The satellite contains two instruments to measure γ-ray radiation from all possible sources; terrestrial, galactic and extragalactic sources. Such sources can be flashes of thunderstorms, the sun, supernovae remnants, pulsars, Gamma Ray Bursts or AGN. The satellite is operated as an all sky monitor, thus the whole sky is detected every three hours and every source can be investigated through time variability. The next two sections show the techniques of the main instruments and the methods for getting light curves and spectra of γ-ray sources.

Figure 5: Artistic impression of the Fermi satellite. (Credit: NASA)

2.1.1 Technical Background

The two instruments are the Gamma-ray Burst Monitor (GBM) (Meegan et al., 2009) and the Large Area Telescope (LAT) (Atwood et al., 2009). The GBM data are not part of thesis and construction will mentioned just very briefly.

The GBM contains 12 sodium iodide scintillation counters who are able to detect γ-ray bursts or γ-ray flashes in an energy range from 10 keV to 1 MeV and two bismuth germanate scintillation counters which are sensitive for flares in an energy range from 1 MeV to 20 MeV (Meegan et al., 2009). Through the analysis of the signals of more detectors the position of the flare can be

determined with an error radius of three degrees.

The LAT is the main instrument on the FGST. The main goal of this instrument is monitoring

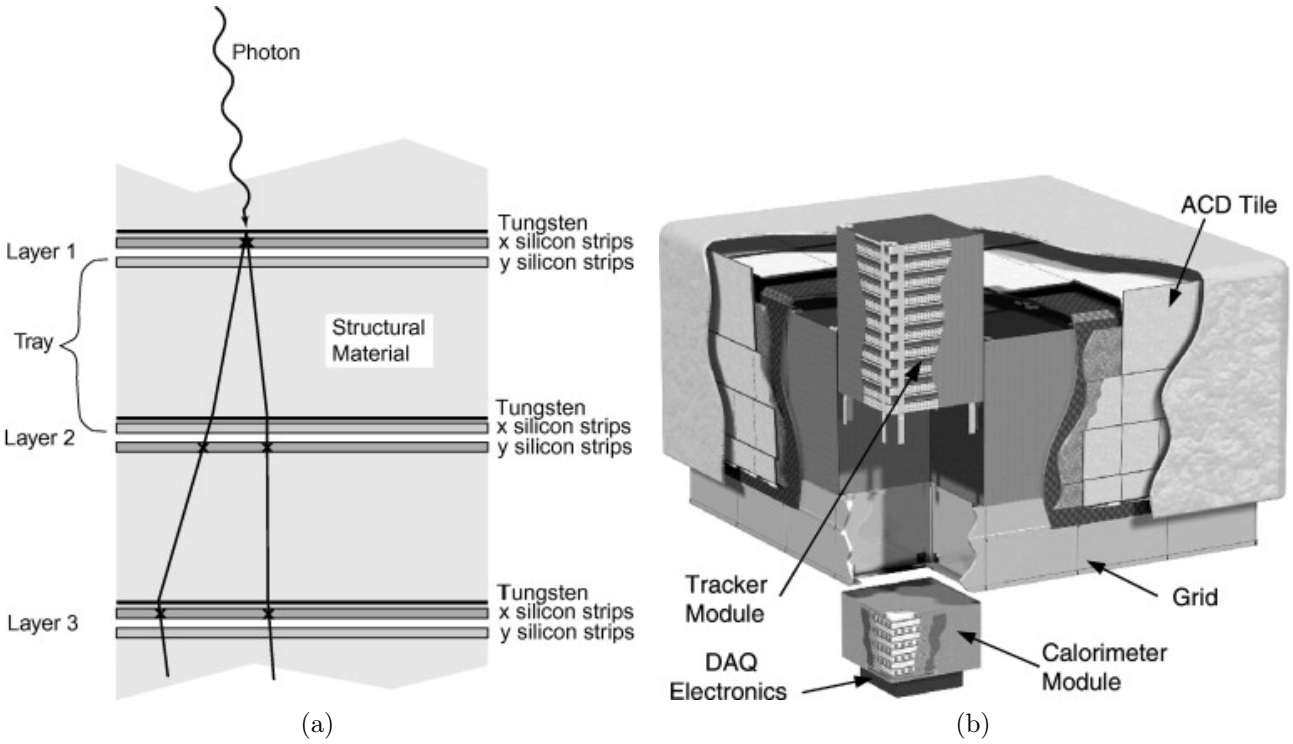

(a) (b)

Figure 6: Diagram of the functional concept of the LAT track detector (a) and an impression of the whole LAT detector (b). (Credit: NASA)

the sky, it sees 20 sr of the sky in an energy range from 20 MeV up to 300 GeV at any time. With its energy resolution, sensitivity, viewing angle and time resolution of 10 μs the LAT is much better than the previous instruments in space like *EGRET*[2] on *CGRO*[3]. The detector of LAT does not detect the incoming γ-ray photon but the produced the electron-positron pair caused by the photon. The detector is built out of 16 particle track detectors and a calorimeter to measure the energy of the e^+e^--pair. One particle track detector contains 18 semiconductor detectors separated by tungsten foils. The tungsten foils are needed for the pair production mechanism. With the semiconductor detectors the track reconstruction of the e^+e^--pair is possible.
The calorimeter is an electro-magnetic calorimeter which detects all particles of the electro-magnetic shower and determine the energy of the incoming photon. The calorimeter contains 96 caesium iodide scintillation counters arranged in 8 layers. Each counter is liked to a photo-diode to measure the scintillation light.
Track detector an calorimeter is shielded by an anticoincidence detector (ACD) in order to reduce background radiation. The main background components are hadronic particles from cosmic radiation and isotropic distributed secondary photons emitted from the particle showers in an energy range of $100 - 1000$ keV.
The data acquisition system (DAQ) collects the data of the track detectors and the calorimeter, labels them with a time mark and saves the spacecraft data. For more details see at Atwood et al. (2009).

[2]Energetic Gamma Ray Experiment Telescope
[3]Compton Gamma Ray Observatory, satellite launched by NASA

2.1.2 Creating light curves and Spectra

The raw data of the γ-ray events are downloaded from satellite every 3 hours, corresponding to 2 orbits. After a pre analysis chain the raw data can be downloaded for further investigation from the Fermi Science Support Center (FSSC) (`http://fermi.gsfc.nasa.gov/ssc/data/access/`). The possible ways to get the raw data are to download the weekly files or a special dataset of a certain region of interest of the sky and time. The weekly files are weekly updated photon files and spacecraft files. The photon files contains energy, coordinates, time and good time interval (GTI) of detected γ-ray events. The corresponding spacecraft file contains the spacecraft parameters like orientation, position, operation mode, data quality (Data_Qual) and configuration of the instrument (Lat_config) at certain time intervals. The scientific products of these raw data can be light curves and spectra, which can be investigated afterwards. In this thesis the Pass 7 reprocessed data (p7rep), the newest galactic interstellar emission model (gll_iem_v05_rev1) and the latest point source catalogue (gll_psc_v08) is used.

In this thesis the scripts of Cornelia Müller, Alica Schooley and Bill McConville are used on the Remeis Cluster to determine light curves and spectra. In the following the necessary steps are briefly described. For more details visit `http://fermi.gsfc.nasa.gov/ssc/`.
The light curve script uses the the weekly files to calculate a light curve for a source of interest. First the script selects with function *gtselect* the necessary photon events for the region of interest (ROI), the time interval and the energy range to reduce the size of the input event file. Then *gtmktime* filters the event file for GTI. Beside these steps the script creates an input model for the later on fitting process with the Fermi Science Tool *make2FGLxml*. The input model contains data for the sources in the ROI which are based on the result of the 2FGL-catalogue (Nolan et al., 2012).
The next step is the calculation of the diffuse source response for the ROI with *gtdiffrsp* if the calculation is needed. After that the calculation is divided into subprocesses for every data point of the light curve. In each subprocess the flux of the bin is calculated. The calculation is done with a maximum likelihood method by calculating the likelihood of each photon event to determine the real origin of the incoming photon and the possible connection of the source of interest. A likelihood function for Poisson data is required in this case,

$$\mathfrak{L} = \prod_{n=1}^{N} \frac{m_i^{n_i} e^{-m_i}}{n_i!} = e^{-N_{\exp}} \prod_{i=1}^{N} \frac{m_i^{n_i}}{n_i!} \tag{2.1}$$

where N is the total number of counts, m_i is the number counts of expected counts by the input model in bin i, n_i are the detected counts in bin i and $N_{\exp}$ is the total number expected counts. For testing the result a test statistic (TS) is calculated.

$$TS = -2 \ln \left(\frac{\mathfrak{L}_{\max,0}}{\mathfrak{L}_{\max}} \right) \tag{2.2}$$

$\mathfrak{L}_{\max,0}$ is the maximum likelihood for the model of the given data (null hypothesis), $\mathfrak{L}_{\max}$ is the maximum likelihood of the model and an additional source. TS give the significance of a possible detection of a source. After Mattox et al. (1996) the TS is comparable to the $\Delta\chi^2$ statistic and the simple estimation $\sigma \approx \sqrt{TS}$ can applied. The internal TS-threshold of the script is a value of 9, for values below the threshold upper limits are calculated. The results of each bin are copied to an ascii-file and be plotted (Fig. 7a).
An alternative method is to use the function *gtbin* to get non background subtracted light curve with counts over time.

Beside light curves, spectra are the other case for science investigation. Like the first the steps of the light curve-script the spectrum-script also calculates *gtselect*, *gtmktime* and *gtdiffrsp*. Then *gtltcube* and *gtexpmap* have to computed before the *gtlike*-function. Also the input model with *make2FGLxml* is created, but this model is updated through a likelihood fit with *gtlike* over the whole dataset. After this the scripts creates several energy bins and provide a likelihood fit to determine the spectrum of the source of interest. The output contains a spectrum (Fig. 7b), a spectral energy distribution, a test statistic and the spectral parameters. These parameters are related to the different fit models. The two most famous models for AGN are a powerlaw model $N(E) = N_0(E/E_0)^{\gamma}$, with a prefactor N_0, a spectral index γ and a reference energy E_0, and a logarithmic parabola model $N(E) = N_0(E/E_b)^{(\alpha+\beta\log(E/E_b))}$ with a spectral index α, a curvature β and a break energy E_b. The models can describe the SED of AGN in the γ-rays. The power law is the most common model to fit the SED. But for bright sources a curvature in model is needed to fit the SED, therefore the logarithmic parabola is used.

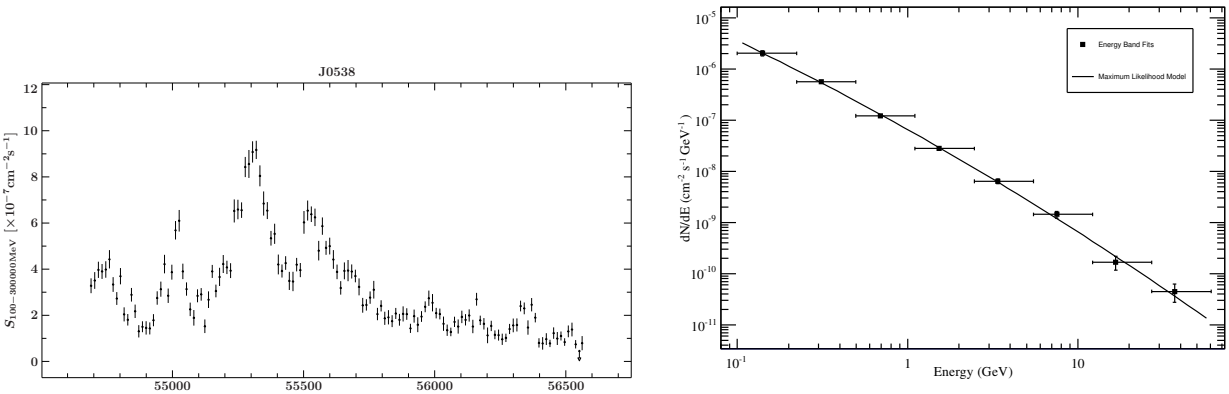

(a) (b)

Figure 7: Typical output of the light curve script (a) and the spectrum script (b).

2.2 Bayesian Blocks

The interesting point of light curves is variation of the flux over time. The evolution and their variation of the light curve properties can give information of emission features and emission models of AGN. It is very useful to define time ranges where the flux is constant. This can be done by hand, but this method is not very objective. A more objective method is finding change points by a mathematical method. Changes points are the points in a light curve where the constant flux changes to another constant value. A common mathematical method to determine change points is the use of Bayesian statistics, better know as Bayesian blocks, there were defined different blocks separated by change points of a constant flux value. This method out of the group of hypothesis tests. The Bayesian blocks can be used with different statistical distributions described in the following.

Some functions to calculate Bayesian blocks were already existing, Scargle (1998) published an algorithm for Poisson distributed data, e.g. counts over time. This algorithm is used in the tool of FSSC *gtburstfit* and in the ISIS-function of the sitar-package of Mike Nowak[4]. These functions only work with the non background subtracted light curves and not with the output of the light curve script.

[4] `http://space.mit.edu/CXC/analysis/SITAR/`

For handling Gaussian distributed data a new algorithm was invented by Scargle et al. (2013). This new algorithm can deal with both distributions Poisson and Gaussian.

2.2.1 Older Method - Poisson Blocks

At first the mathematical background of the new algorithm is explained with the Poisson distribution and results are compared with the output of the sitar-function. In the next subsection the mathematical background for Gaussian distribution is shown.

The ansatz for the Bayesian Blocks is the Bayes-theorem. The variable μ stands for the Poisson rate in the following.

$$p\left(\mu|\mathrm{I},\mathrm{D}\right) = \frac{p\left(\mu|\mathrm{I}\right)p\left(\mathrm{D}|\mu,\mathrm{I}\right)}{p\left(\mathrm{D}|\mathrm{I}\right)} \tag{2.3}$$

where μ is a constant Poisson rate, D is the given data and I the assumed model. The theorem deals with conditional probabilities which can be calculated. The interesting conditional probability is the one of the left side of the of the equation. It is the probability for a constant Poisson rate under the condition of the given data and the assumed model. To solve this problem it is necessary to determine the other conditional probabilities. Two of them have to be constant $p(\mathrm{D}|\mathrm{I})$ and $p(\mu|\mathrm{I})$. The third, $p\left(\mathrm{D}|\mu,\mathrm{I}\right)$, is often called the likelihood function $\mathfrak{L}^{(k)}(\mu)$ and is a product of independent distributions, in this case the Poisson distribution,

$$L_n = \frac{\left(\mu e_n W_n\right)^{N_n} e^{-\mu e_n W_n}}{N_n!}, \tag{2.4}$$

where N_n is the number of events in bin n, μ the event rate in counts per unit time, e_n is the exposure averaged over the bin and W_n is the bin width in time units. e_n and W_n can combined to the bin efficiency $w_n = e_n W_n$. The likelihood of all bins in block k is then:

$$\mathfrak{L}^{(k)}(\mu) = \prod_{n=1}^{M^{(k)}} L_n = \mu^{N^{(k)}} e^{-\mu w^{(k)}} \tag{2.5}$$

$M^{(k)}$ is the number of bins in block k,

$$w^{(k)} = \sum_{n=1}^{M^{(k)}} w_n \tag{2.6}$$

is the sum of the bin efficiency in the block and

$$N^{(k)} = \sum_{n=1}^{M^{(k)}} N_n \tag{2.7}$$

is the total event count in the block. The factor $(e_n W_n)^{N_n}/N_n!$ can be neglected because the product over all bin in all blocks is a constant. The other conditional distributions are:

$$p(\mu|\mathrm{I}) = \frac{1}{\mu_{max}}\,;\, 0 < \mu \leq \mu_{max} \tag{2.8}$$

$$p(\mathrm{D}|\mathrm{I}) = \int_0^\infty \mathrm{d}\mu p(\mu|\mathrm{I})\, p(\mathrm{D}|\mu,\mathrm{I}) \tag{2.9}$$

$$= \int_0^\infty \mathrm{d}(\mu e_n W_n) p(\mu|\mathrm{I})\, (\mu e_n W_n)^{N_n}\, e^{-\mu e_n W_n} \simeq N_n! \tag{2.10}$$

Only the equation 2.5 is not constant and the logarithm can be maximized to get the position of the different change points and resulting Bayesian blocks.
This step is done by the algorithm of Scargle et al. (2013). The algorithm uses the technique of dynamic programming from Jackson et al. (2003). Caused by the fact that the real number of change points is not know at the start of the algorithm a value called *ncp_prior* is defined.

$$ncp\_prior = 4 - \log\left(73.53 \cdot p_0 N^{-0.478}\right) \tag{2.11}$$

where p_0 is the false positive rate, the rate of a false change point detection. The equation for *ncp_prior* is a result of simulations to connect the *ncp_prior* to the number of data points. This equation provides a good estimation for the *ncp_prior*. If extreme values of *ncp_prior* are used this parameter give bad results in the form of clearly too few or too many blocks.
Scargle et al. (2013) published beside his theoretical paper a *matlab* code which was implemented in *s-lang* and is included in the ISIS-scripts as the function *bayesian_blocks* by Mathias Kühnel. My contribution was the debugging and the adjustment of the Gaussian option of the code to use it for the Fermi light curves.
To compare the old (Scargle, 1998) and the new (Scargle et al., 2013) algorithm the same light curve is analysed with the sitar function and the ISIS-script function to show the differences and similarities (Sec. 3.1).

2.2.2 New Method - Gaussian Blocks

The problem of the output of the light curve script is that the data not Poisson distributed, they follow a Gaussian distribution. This leads to the fact that the old algorithm can not be used. But in the new algorithm the solution for Bayesian blocks of Gaussian distributed data is included. The start of the calculation is still equation 2.3 but the parameter μ change to $x_n = \mu + \sigma_n$. This new expression is already a special solution of the general calculation. The assumption is that the noise σ is known but not constant for each bin. The input distribution is now the Gaussian distribution:

$$L_n = \frac{1}{\sigma_n\sqrt{2\pi}} e^{-\frac{1}{2}\left(\frac{x_n-\mu}{\sigma_n}\right)^2} \tag{2.12}$$

Then the conditional possibilities can be derived,

$$p(\mu|\mathrm{I}) = \frac{1}{\mu_H - \mu_L}\,;\, \mu_L < \mu \leq \mu_H \tag{2.13}$$

$$p(\mathrm{D}|\mathrm{I}) = \int_{\mu_L}^{\mu_H} \mathrm{d}\mu p(\mu|\mathrm{I})\, p(\mathrm{D}|\mu,\mathrm{I}) \tag{2.14}$$

$$p(\mathrm{D}|\mu,\mathrm{I}) = \mathfrak{L}^{(k)}(\mu) \tag{2.15}$$

The new likelihood function is still the product of the single distributions of each bin.

$$\mathfrak{L}^{(k)}(\mu) = \prod_n L_n = \frac{(2\pi)^{-\frac{N_k}{2}}}{\prod_m \sigma_m} e^{-\frac{1}{2}\sum_n \left(\frac{x_n-\mu}{\sigma_n}\right)^2} \tag{2.16}$$

where N_k is the number of bins in block k. Like in the Poisson case the maximum log likelihood is calculated, this function gets very simple,

$$\log \mathfrak{L}^{(k)}_{max}(\mu) = -\frac{1}{2}\sum_n \left(\frac{x_n - \frac{\sum_n \frac{x_n}{\sigma_n}}{\sum_n \frac{1}{\sigma_n}}}{\sigma_n} \right)^2 \tag{2.17}$$

It can be seen that the noise σ_n has a big effort of the number of blocks in the data sample. For the algorithm also in this case the variable *ncp_prior* is needed, but it is more difficult to derive the function. Through simulations for a fixed false positive rate $p_0 = 0.05$ a function be estimated as

$$ncp\_prior = 1.32 + 0.577 \log(N) \tag{2.18}$$

In this estimation the false positive rate appears not as an independent parameter (Fig. 8).

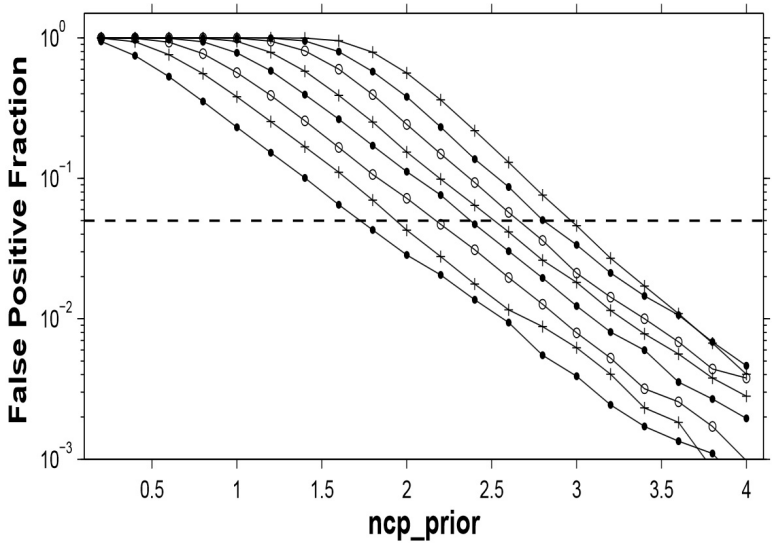

Figure 8: False positive fraction p_0 over value of *ncp_prior* with separated curves for the values $N = 8$, 16, 32, 64, 128, 256, 512 and 1024 (left to right; alternating dots, + and circles) (Scargle et al., 2013).

The change of the *ncp_prior* changes the false positive rate as well, if the change is very large, bad results appears in the form of too few or too many blocks. The influence of the *ncp_prior* to the number of blocks is shown in Sec. 3.3. With this informations the ISIS-script function *bayesian_blocks* can calculate Bayesian blocks for output data from the light curve script.

3 Bayesian Blocks of Fermi light curves

The Gaussian Bayesian block algorithm (Sec. 2.2.2) and the *Fermi* light curves (Sec. 2.1.2) can provide a better picture of the variation of light curves in time. In the following section the various parameters that have a big influence on the Bayesian blocks are shown and analysed. It is also demonstrated that the new algorithm works at least well as the old one. For the following demonstration the light curves of the blazar PKS 0537-441 are used, one of the later analysed sources (Sec. 4) and to verify the results of the real light curve the algorithm is tested with simulated light curves with a known number of blocks.

3.1 New Code - Better Code?

The new and the old algorithm can handle Poisson distributed data. To demonstrate that the new one is good enough to replace the old algorithm the same bolometric light curve is used. This light curve contains counts and is not background subtracted, in the following it shall be named a raw light curve. This raw light curve is generated with the *gtbin* tool of the Fermi tools.

The two algorithms find variation in the light curve. The input parameters are the same for both

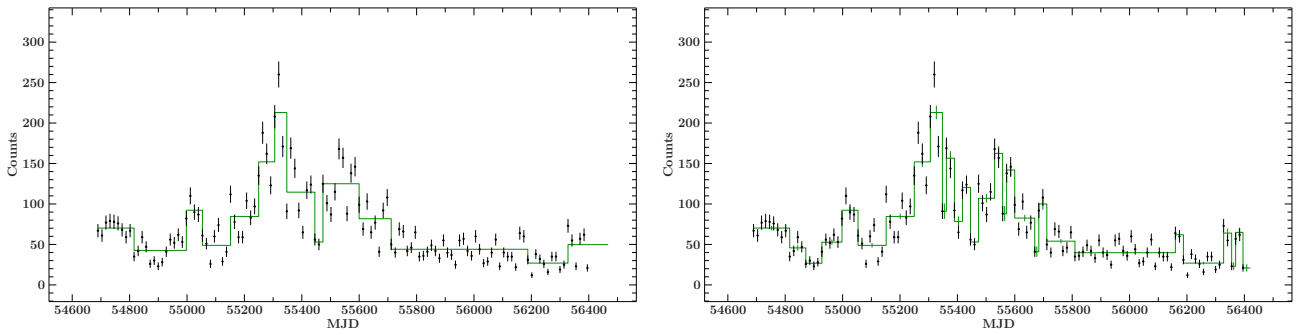

(a) sitar-function (b) new isis-function

Figure 9: Block representation determined by the sitar function (a) and the new isis-function *bayesian_blocks*(b).

functions, $ncp\_prior = 4.998$ and the false positive rate $fpr = 0.05$. The sitar-function finds 14 blocks and the Bayesian-blocks-function determines 29 blocks (Fig. 9). The new algorithm finds more blocks, this might be a result of the method of dynamic programming which is the basic method of the iteration mechanism of the new code (Scargle et al., 2013). Another reason could be that the new algorithm is more sensitive to this special light curve.

In addition to this, a constant light curve for Poisson distributed data is simulated and fake peaks or larger blocks with a different constant count rate are added to the light curve. Four different light curves with 5 peaks in each light curve and different bin size of the peaks, from one to four bins per peak, were calculated. Other light curves with two and two and three steps were also simulated. The simulated light curves were also analysed with both functions and the same input parameters, $ncp\_prior = 4.899$ and the false positive rate $fpr = 0.05$.

In all simulated light curve both functions find the same number of change points (Tab. 2). In the peak light curves both algorithms can not determine all pre defined peaks, the lowest two peaks with the smallest changes are neglected. The same picture is shown in the double peak

Table 2: Comparison between the new and the old algorithm in the number of blocks in different simulated light curves.

light curve	N_{Blocks} in light curve	N_{Blocks} new algorithm	N_{Blocks} old algorithm
5 peaks (1 bin)	11	3	3
5 peaks (2 bins)	11	7	7
5 peaks (3 bins)	11	7	7
5 peaks (4 bins)	11	7	7
2 peaks	9	5	5
2 steps	7	7	7
3 steps	9	7	7

light curve only the highest peak rate is detected, the wing blocks are neglected. In the case of broad blocks in the light curve both functions cannot detect a small dip in a broader block. But the two major blocks were found.

The light curve of 0537-441 and the simulated light curves show that the new algorithm (Scargle et al., 2013) can be compared to the old algorithm (Scargle, 1998). In the light curve of 0537-441 the new code finds more blocks but this is just a special case for this light curve. The simulated light curves showed that the new code finds the same blocks as the old one does. It is shown that the new code is as good as the old one in the case of Poisson distributed data.

3.2 Bin Size of Light Curves

The bin size of the light curve has a major influence on the number of blocks. The bin size is directly connected to the number of bins of each light curve if the light curve time range is constant. For example, if a 28-day binning is chosen the light curve contains 67 bins for the time range of 2008/08/04 to 2013/10/01 in respect to this a 14-day binned light curve contains 135 bins. The different number of bins per light curve is related to the value of *ncp_prior* (Eq. 2.18). When the number of bins increases the value of *ncp_prior* increases as well.
Four different light curves, each with a different binning, were produced in the same time range (2008/08/04 to 2013/10/01) to investigate the influence of different bin sizes to the number of of blocks. The same source as in the section before was used. The binning of 7, 14 ,21 and 28 days were chosen. In the default case the light curve is binned with 14 days, in some other cases a monthly binning is used (30 days), this binning is expressed by the 28 day binning.
The result (see Tab. 3, Fig. 10) shows that the number of blocks increases with the increase of the bin size, with the decrease of *ncp_prior* and the number of bins. At first this result appears strange, but the light curves are a result of single bin fits to determine the flux value of each bin. Hence, when the bin size is increased the static of the fits becomes better and the uncertainty (σ) is smaller. Beside the input parameters *ncp_prior* and fpr there are also intrinsic input parameters like the flux value and the associated uncertainty of the bin. However the bin size is not the dominant one, but in fact a larger bin size purveys a better picture. In contrast, short variations are neglected in these cases.

Table 3: The bin size influence on the number of bin N_{Bins}, *ncp_prior* and the number of blocks N_{Blocks}.

Bin size	7 days	14 days	21 days	28 days
N_{Bins}	270	135	90	67
ncp_prior	4.55	4.15	3.92	3.75
N_{Blocks}	17	19	20	21

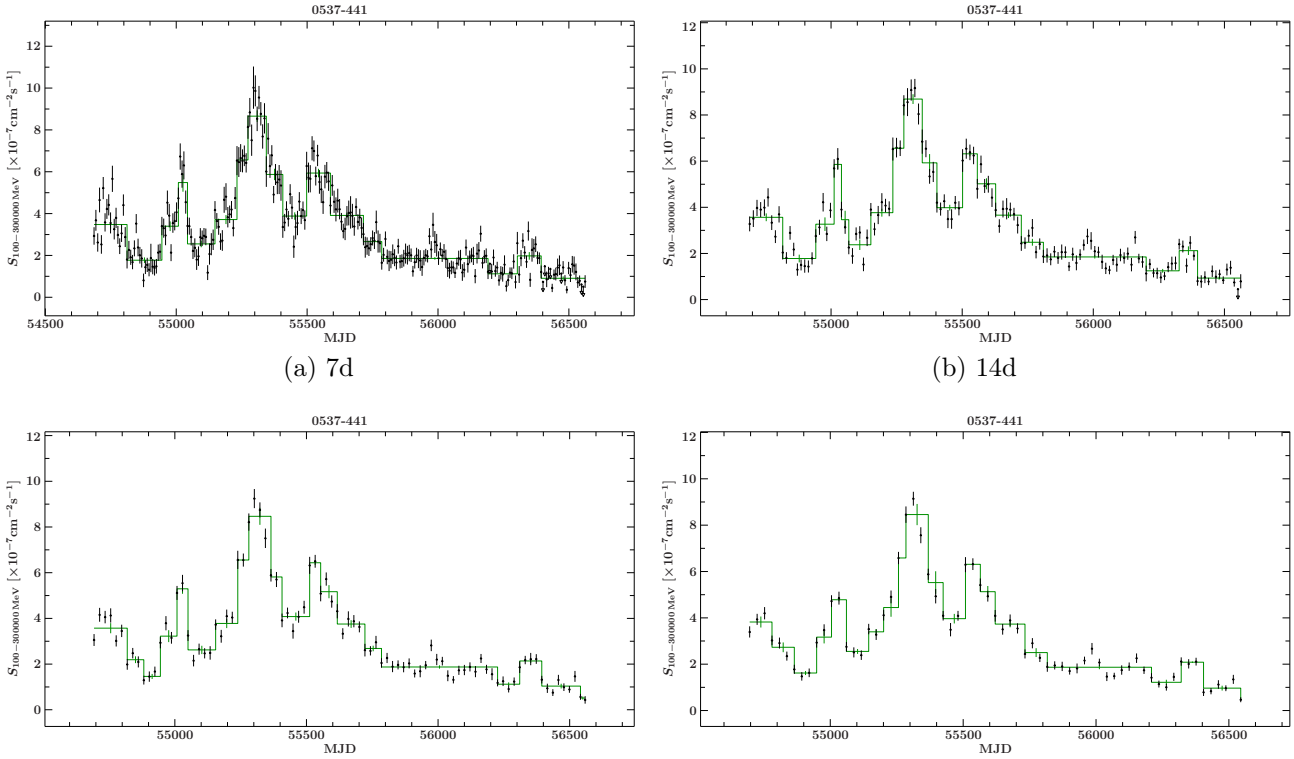

(a) 7d (b) 14d

(c) 21d (d) 28d

Figure 10: Light curves and their corresponding blocks with a different bin size of 7 days (a), 14 days (b), 21 days (c) and 28 days(d).

3.3 Influence of Input Parameters

The other parameters are going to be examined with a single light curve binned by 14 days and is taken in time range of more than five years (2008/08/04 to 2013/10/01).
At first different *ncp_prior* values are tested. The interesting point of this case is the influence of this value to the number of blocks, which is comparable to the number of change points after running the algorithm, $N_{\text{Blocks}} = N_{\text{CP}} + 1$. The main question is, how large is the influence of the priori number of change points on the real number of change points? Another question is whether *ncp_prior* is different from the intrinsic one from Eq. 2.18, which change points are new and which are neglected?
To answer these questions different *ncp_prior*, distributed around the intrinsic value, are chosen. In addition, a large value of *ncp_prior* is also chosen. Tab. 4 and Fig. 11 show that *ncp_prior* has an influence on the resulting number of blocks. The number of blocks increases by decreasing

Table 4: The *ncp_prior* influence of the number of blocks N_{Blocks} and change points N_{CP}.

ncp_prior	2.0	3.0	3.5	4.0	4.15	4.5	5.0	5.5	6.0	7.0	19.0
N_{Blocks}	24	20	20	19	19	19	18	17	17	15	7
N_{CP}	23	19	19	18	18	18	17	16	16	14	6

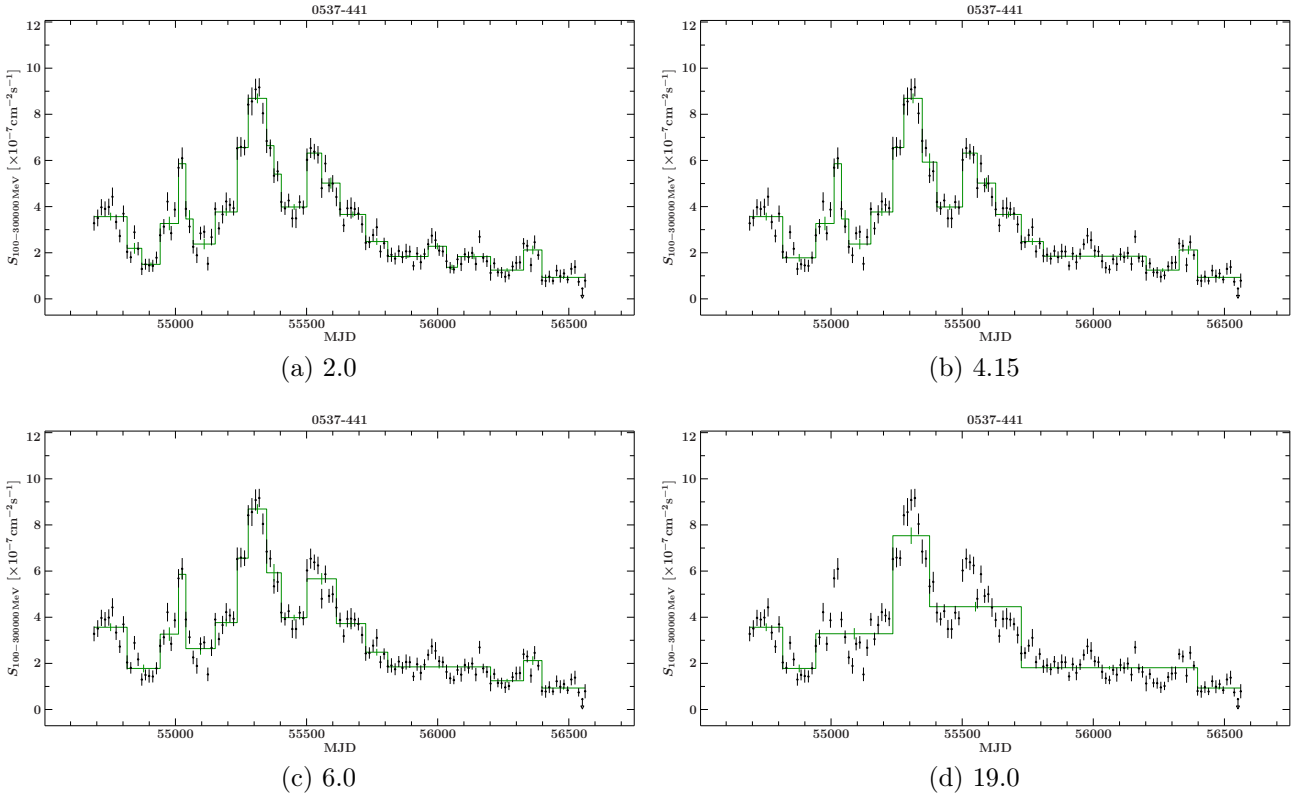

(a) 2.0 (b) 4.15

(c) 6.0 (d) 19.0

Figure 11: Light curves and their corresponding blocks with a different *ncp_prior* of 2.0 (a), 4.15 (b), 6.0 (c) and 19.0 (d).

the value *ncp_prior*. From Fig. 11a to Fig. 11d less tiny variation are represented by blocks. In Fig. 11a even small dips are detected which are already neglected in Fig. 11b (default parameters). In Fig. 11d at the highest *ncp_prior* value only the strong peak and remarkable changes in the light curve are found.

To verify this behaviour a constant Gaussian light curve was simulated and peaks and blocks were added to this light curve as in Sec. 3.1. Five different light curves with five peaks, one peak and one dip, one peak and four broad steps, six, nine and ten steps. For all light curves the *ncp_prior* is changed from 2 to 6 for this analysis. The constant simulated light curves with just white noise show the same result for all different values of *ncp_prior*, only a single block is detected. This means that the light curve is constant over whole time. In all other light curves the result is the same (Fig. 5), with a small value *ncp_prior* the number of change points is higher than with larger values. In the cases with small values the tiny steps are detected, in the case with larger values only the steps with the greatest changes in the light curve are detected.

This result is based on the fact that *ncp_prior* is not an independent parameter. Three parameters are related to each other, *ncp_prior*, the false positive rate and the number of bins

Table 5: The *ncp_prior* influence of the number of blocks N_{Blocks} for simulated light curves.

N_{Blocks} simulated	*ncp_prior*	2.0	2.5	3.0	3.5	4.0	4.5	5.0	5.5	6.0
1 (constant LC)	N_{Blocks}	1	1	1	1	1	1	1	1	1
7	N_{Blocks}	6	6	5	5	5	5	5	5	5
9	N_{Blocks}	7	7	5	3	3	3	3	3	3
11	N_{Blocks}	10	10	6	6	5	5	5	5	5
11	N_{Blocks}	10	8	8	8	8	8	8	8	8
10	N_{Blocks}	9	9	7	7	7	5	5	5	5
12	N_{Blocks}	14	14	12	11	11	10	10	10	10

(Fig. 8). If one parameter is fixed like the number of bins and *ncp_prior* is chosen to have a certain value, the value of fpr is determined by the value of *ncp_prior*. A different value as an input parameter is neglected by the algorithm.
The fpr has an influence on the *ncp_prior* function, see Eq. 2.18 for a $fpr = 0.05$. If the input value is changed to a different value the function and the result of *ncp_prior* is different for the same number of bins. For smaller fpr's the number of blocks decreases because no probably false blocks are detected, only the blocks with a large significance of 99.999%. For further analysis it is a good suggestion to use the default fixed fpr value of 0.05 and the related *ncp_prior*-function (Eq. 2.18), then the results can be easily reproduced without further studies of the input parameter to determine different *ncp_prior*-functions for other fpr values.

Finally we discuss the last parameter, the uncertainty σ, as an input parameter for the Gaussian likelihood function. This parameter depends solely on the output of the light curve-script and the executed likelihood analysis of the raw data. The light curve has a 14 day binning and the other input values are fixed at the default values. The size of σ is changed by multiplying a factor to the computed value. Small changes like 5% or 10% and larger ones, such as a factor of 2 or 0.5, are investigated.
In Tab. 6 the global result is very clear. When the uncertainty of the bins is just a third or half

Table 6: The influence of the size of the uncertainty σ on the number of blocks N_{Blocks}.

σ-factor	1/3	0.5	0.9	0.95	1	1.05	1.1	2
N_{Blocks}	59	37	20	19	19	19	17	7

of the original value more blocks are found (Fig. 12a) and if the uncertainty is larger only the significant changes in the light curve are recognised (Fig. 12d). A small uncertainty of the bin flux value leads to higher probability for an existing change point. For small changes of the uncertainties the effect from Sec. 3.2 can be seen. The number of blocks changes just around one or two blocks when the uncertainty changes by 10% (Fig, 12b and Fig. 12c). In addition to this, simulated Gaussian light curves were also multiplied with the same prefactors. The

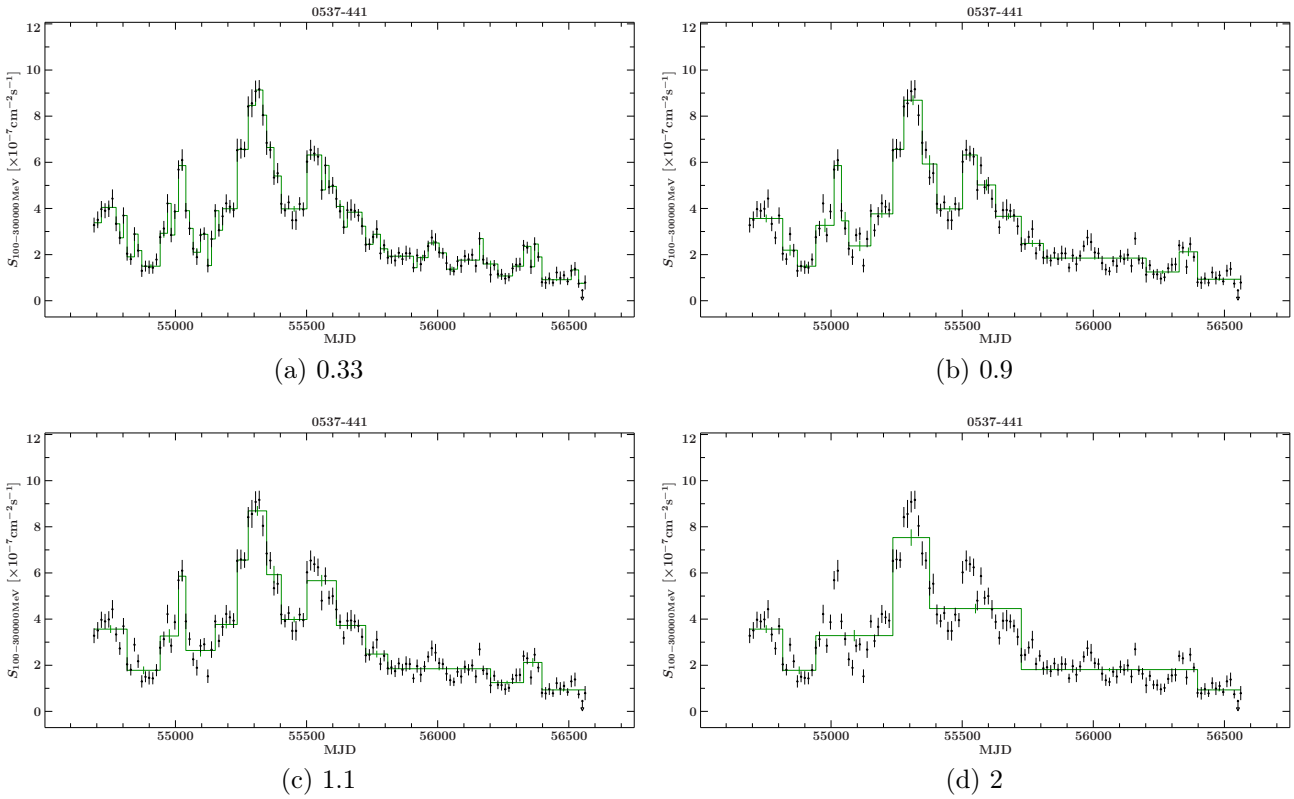

(a) 0.33 (b) 0.9

(c) 1.1 (d) 2

Figure 12: Light curves and their corresponding blocks with a different size of σ. 0.33σ (a), 0.9σ (b), 1.1σ (c) and 2σ (d).

constant light curve with just white noise shows that blocks can be detected if the uncertainties are very small, but these detected blocks are just a result of the white noise. The results of the other light curves show that besides known blocks the algorithm finds an additional number of blocks in the cases of small uncertainties. These additional blocks are a result of the covering white noise of the constant Gaussian light curve. In the most cases of the simulated light curves a small change of the uncertainties of the flux values does not affect the number of blocks, but if the uncertainties too large only the major features are represented by blocks (Tab. 7).

In this context a small uncertainty of the flux values can show a better picture of the variation,

Table 7: The influence of the size of the uncertainty σ on the number of blocks N_{Blocks} in simulated light curves.

N_{Blocks} simulated	σ-factor	1/3	0.5	0.9	0.95	1	1.05	1.1	1.5	2
1 (constant LC)	N_{Blocks}	26	5	1	1	1	1	1	1	1
7	N_{Blocks}	26	9	5	5	5	5	5	5	3
10	N_{Blocks}	24	14	7	7	7	7	5	5	5
11	N_{Blocks}	36	15	8	8	8	8	8	7	5
12	N_{Blocks}	36	18	12	11	10	10	10	10	8

but if the uncertainty is too small not all statistical variations can neglected.

4 Bayesian Analyse of Flaring Sources

4.1 Source Sample

The sources investigated in the scope of this thesis originate from the TANAMI[5] project. The TANAMI project is a radio monitoring campaign of radio-loud AGN on the southern hemisphere. The radio monitoring utilizes the VLBI[6] technique to get a picture of the inner parts of the AGN in milliarcsecond resolution (Müller et al., 2013). With this the inner parsec of the jet can be resolved. Besides the radio data, the TANAMI project takes other wavelengths such as optical, UV, X-ray and γ-ray into account in order to analyse the full electromagnetic spectrum (Ojha et al., 2010).
The basic sample sources are those TANAMI-sources which can be associated with sources from the 2FGL-catalogue. This relationship is inherent for 55 sources (Tab. 8). Müller (2014) analysed the sources in her PhD-thesis and calculated the values listed in Tab. 8. The energy range of this analysis is 1 GeV to 100 GeV, the best energy range of the LAT-instrument and in a time range of 2008/8/4 to 2010/8/4. Müller (2014) searched for short flaring sources to suggest possible source candidates for extra galactic neutrino emission. These source candidates from the ANTARES[7]-project are used to identify possible neutrino sources.
The marked sources in Tab. 8 were chosen according to the following short flare criteria:

- a source with flux bins greater than five times the four year averaged flux ($S_{4\mathrm{yrs}}$) is a flaring source
- the number of bins with the flux greater than the four year averaged flux plus 3σ, leads to the short criteria $1/N_{\mathrm{Bins}(S>S_{4\mathrm{yrs}})}$

With these two criteria 20 sources were found which showed short flares. In this analysis all flux upper limits were neglected.

In addition to the short flare criteria the Bayesian block criterion is applied in this thesis:

- sources with a positive detection of Bayesian blocks through the Bayesian block algorithm are sources which show statistical variations

The analysis showed that 20 sources have variation in respect of the Bayesian block algorithm, the upper limits are neglected as well. These sources are also marked in Tab. 8. If both criteria, the short flare and the Bayesian block criteria, are combined, only 9 sources out of the 55 TANAMI-2FGL sources are left. In the following the 9 sources and the other 11 Bayesian block sources are investigated and analysed.

[5] Tracking Active Galactic Nuclei with Austral Milliarcsecond Interferometry (`http://pulsar.sternwarte.uni-erlangen.de/tanami/`)
[6] Very Long Baseline Interferometry
[7] Astronomy with a Neutrino Telescope and Abyss environmental Research; Tscherenkow neutrino telescope in the Mediterranean sea

Table 8: γ-ray properties ($1 - 100\,\mathrm{GeV}$) of TANAMI sources (MJD 54689.65 – 56131.65) (Müller, 2014)

Name	2FGL Name	S_{max} $\left[\times 10^{-10}\,\mathrm{cm}^{-2}\,\mathrm{s}^{-1}\right]$	$S_{\mathrm{max}}/S_{4\mathrm{yrs}}$	$S_{4\mathrm{yrs}}$ $\left[\times 10^{-10}\,\mathrm{cm}^{-2}\,\mathrm{s}^{-1}\right]$	$\Gamma_{4\mathrm{yrs}}$ $(1 - 100\,\mathrm{GeV})$	short flare candidate	Bayesian blocks
0047-579	2FGLJ0049.75738	495.10	110.34	4.49± 0.92	2.12		
0055-328	2FGLJ0057.9-3236	60.15	4.47	13.47± 1.41	2.40		
0208-512	2FGLJ0210.7-5102	341.07	6.31	54.03± 2.52	2.64	X	X
0227-369	2FGLJ0229.3-3644	137.63	13.63	10.09± 1.33	2.85	X	
0244-470	2FGLJ0245.9-4652	234.19	4.90	47.82± 2.38	2.80		X
0302-623	2FGLJ0303.5-6209	62.66	6.54	9.59± 1.23	2.47		
0308-611	2FGLJ0310.0-6058	115.44	9.39	12.29± 1.36	2.50	X	
0332-376	2FGLJ0334.3-3728	155.13	4.85	31.96± 2.00	2.18		
0332-403	2FGLJ0334.2-4008	259.07	5.53	46.87± 2.34	2.34	X	X
0402-362	2FGLJ0403.9-3604	883.17	13.95	63.30± 2.72	2.59	X	X
0405-385	2FGLJ0407.3-3826	126.30	7.08	17.83± 1.61	2.53	X	
0412-536	2FGLJ0413.5-5332	110.21	12.32	8.95± 1.19	2.11	X	
0426-380	2FGLJ0428.6-3756	769.40	3.71	207.58± 4.67	1.60		X
0447-439	2FGLJ0449.4-4350	266.96	2.33	114.48± 3.41	1.88		X
0454-463	2FGLJ0456.1-4613	108.36	7.03	15.41± 1.56	2.69	X	
0516-621	2FGLJ0516.8-6207	96.22	3.12	30.81± 1.77	2.27		
0521-365	2FGLJ0523.0-3628	369.86	7.48	49.42± 2.53	2.65	X	X
0524-485	2FGLJ0526.1-4829	138.22	10.73	12.88± 1.56	2.22		
0537-441	2FGLJ0538.8-4405	1167.79	3.29	355.31± 5.87	1.84		X
0625-354	2FGLJ0627.1-3528	61.81	4.18	14.80± 1.60	1.90		
0637-752	2FGLJ0635.5-7516	105.35	8.02	13.14± 1.53	3.12	X	
0700-661	2FGLJ0700.3-6611	108.06	2.94	36.73± 2.14	2.15		
0717-432	2FGLJ0718.7-4320	75.69	2.86	26.47± 2.00	1.91		
0736-770	2FGLJ0734.2-7706	77.32	4.69	16.50± 1.84	2.42		
0745-330	2FGLJ0747.5-3305	201.42	5.50	36.62± 3.58	2.63	X	
0812-736	2FGLJ0811.1-7527	72.96	2.52	28.94± 2.03	1.93		
1057-797	2FGLJ1057.0-8004	185.60	5.03	36.90± 2.35	2.23	X	
1101-536	2FGLJ1103.9-5356	216.48	4.71	46.01± 2.72	2.32		X
1104-445	2FGLJ1107.2-4448	125.62	13.06	9.62± 1.59	2.98		
1144-379	2FGLJ1146.8-3812	76.69	4.44	17.27± 1.70	2.31		
1313-333	2FGLJ1315.9-3339	323.61	11.74	27.57± 2.18	2.39	X	X
1322-428	2FGLJ1325.6-4300	137.21	4.33	31.70± 2.66	2.42		
1323-526	2FGLJ1326.7-5254	206.92	6	34.50± 2.66	2.57	X	
1325-558	2FGLJ1329.2-5608	308.35	4.05	76.20± 3.63	2.38		X
1344-376	2FGLJ1347.7-3752	110.42	9.88	11.17± 1.57	2.46	X	
1424-418	2FGLJ1428.0-4206	1456.38	8.14	178.90± 4.61	1.92	X	X
1440-389	2FGLJ1443.9-3908	106.46	2.61	40.77± 2.46	1.86		
1454-354	2FGLJ1457.4-3540	468.96	6.24	75.20± 3.17	2.03	X	X
1501-343	2FGLJ1504.9-3433	54.46	5.52	9.86± 1.60	2.65		
1505-496*	2FGLJ1508.5-4957	-	-	13.78± 2.21	2.74		
1600-445	2FGLJ1604.5-4442	243.09	3.78	64.27± 3.79	2.69		X
1600-489	2FGLJ1603.8-4904	246.84	1.84	133.90± 5.23	2.18		
1606-667	2FGLJ1610.8-6650	94.78	3.64	26.07± 1.97	1.84		
1610-771	2FGLJ1618.2-7718	82.23	4.40	18.67± 1.85	2.94		
1646-506	2FGLJ1650.1-5044	197.25	2.66	74.18± 2.48	2.45		
1714-336	2FGLJ1717.7-3342	576.70	5.98	96.46± 5.40	1.93	X	X
1716-771	2FGLJ1725.1-7714	84.38	5.21	16.18± 1.84	2.91		
1759-396	2FGLJ1802.6-3940	507.60	4.68	108.48± 3.97	1.66		
1933-400	2FGLJ1937.2-3955	83.23	8.08	10.31± 1.65	2.35		X
1954-388	2FGLJ1958.2-3848	170.39	5.13	33.20± 2.32	2.69	X	
2005-489	2FGLJ2009.5-4850	141.42	3.55	39.83± 2.28	1.81		
2052-474	2FGLJ2056.2-4715	333.20	4.84	68.78± 4.22	2.65		X
2136-428	2FGLJ2139.3-4236	187.56	3.69	50.85± 2.55	2.28		X
2149-306	2FGLJ2151.5-3021	36.34	5.31	6.85± 1.37	4.00		
2155-304	2FGLJ2158.8-3013	507.45	2.23	227.30± 4.81	1.91		X
2204-540	2FGLJ2208.1-5345	167.88	15.10	11.12± 1.36	2.59	X	X
2326-477	2FGLJ2329.7-4744	69.39	16.07	4.32± 1.15	2.43		

Note: The columns give the TANAMI source name, 2FGL catalogue name, minimum/maximum γ-ray flux (1-100 GeV), the ratio to the 4 yrs averaged flux, the 4 yrs flux, the photon index. *The source PKS 1505-496 was not detected in the 14 day binned light curve.

4.2 Sample Analysis

The 20 sources of Bayesian block sample were analysed in the same way. A closer look was taken at the 9 sources of both selections. The detailed analysis can provide a better picture of the short flaring sources and their spectral properties in the different stages of activity. Flares are associated with high activity of AGN.

4.2.1 Method

Through the pre-selection during the check of the sample criteria light curves of all 55 sources were created. The light curve is the first step of this analysis. The energy range of these light curves is $1 - 100\,\mathrm{GeV}$ and is binned with 14 days. The ROI is 20° and the upper limit threshold was fixed to 9, equal to a source detection of 3σ. The time range is two years of data, from 2008/08/04 to 2010/08/04. Then the algorithm determines the Bayesian blocks of every single light curve. The default settings of the algorithm were used, the *ncp_prior* is based on Eq. 2.18 with a fpr of 0.05. All upper limits are neglected, this can lead to a low number of bins in weak γ-ray sources of the sample. The 2 year light curve contains 135 bins, the number of bins can differ by the number of upper limits of each source. The blocks are the next step of the analysis. The start and stop times of the blocks are the input parameters for the spectrum script. After computation of the spectra, the spectral properties can be analysed in time resolution based on the time size of the block. The block algorithm also determines the mean flux value of each block. This fact suggests it is good to analyse the mean values of the flux resulting from the spectrum script and the algorithm. Additionally, the mean flux can be compared with spectral components like the spectral index depending on the flux. This may be evidence for the change in the spectrum during different stages of activity in AGN. This can further lead to a more detailed understanding of the non-thermal radiation mechanism.

4.2.2 Results

The results of all sources are presented in this section. The sources are divided into two parts. The first part presents some selected sources with interesting results. The second part contains the other sources which, while also interesting, are more common. At last a global picture of the sources is shown.

At first, 8 sources are chosen subjectively to present their results in a detailed way. 0537-441, the source of the code testing section (Sec. 3) is also a part of the Bayesian sample but not one of the short flare samples. The light curve (Fig. 13, upper panel) shows clearly visible variations which can also be detected by the algorithm. The light curve shows a constant period of a few weeks, then the flux drops and rises again to the first small peak. After that the big flare rises rapidly in a few weeks and stays on the maximum flux $S_{1-100\,\mathrm{GeV}} = 1.07 \cdot 10^{-7}\,\mathrm{cm}^{-2}\mathrm{s}^{-1}$ for 8 weeks. Afterwards the flux declines around a half and peaks again. Subsequently the flux declines in 14 weeks over one block to a flux of $S_{1-100\,\mathrm{GeV}} = 0.16 \cdot 10^{-7}\,\mathrm{cm}^{-2}\mathrm{s}^{-1}$ which stays over a longer time to the end of the light curve.

The computed spectra of all blocks show the variation of the spectral components of the source. 0537-441 was fitted with a logarithmic parabola. The spectral index Γ also displays variation which can be combined with the light curve (Fig. 13, mid panel). The behaviour of the index evolves in the same way as the evolution of the flux up to the main peak. At the time of the main peak the flux index relationship changes to anti-correlated (Fig. 13, lower panel). After the second hump the flux index relationship changes to the behaviour before the main peak. The plotted spectra of the main peak are shifted to higher energies when the flux is higher (Fig. 14).

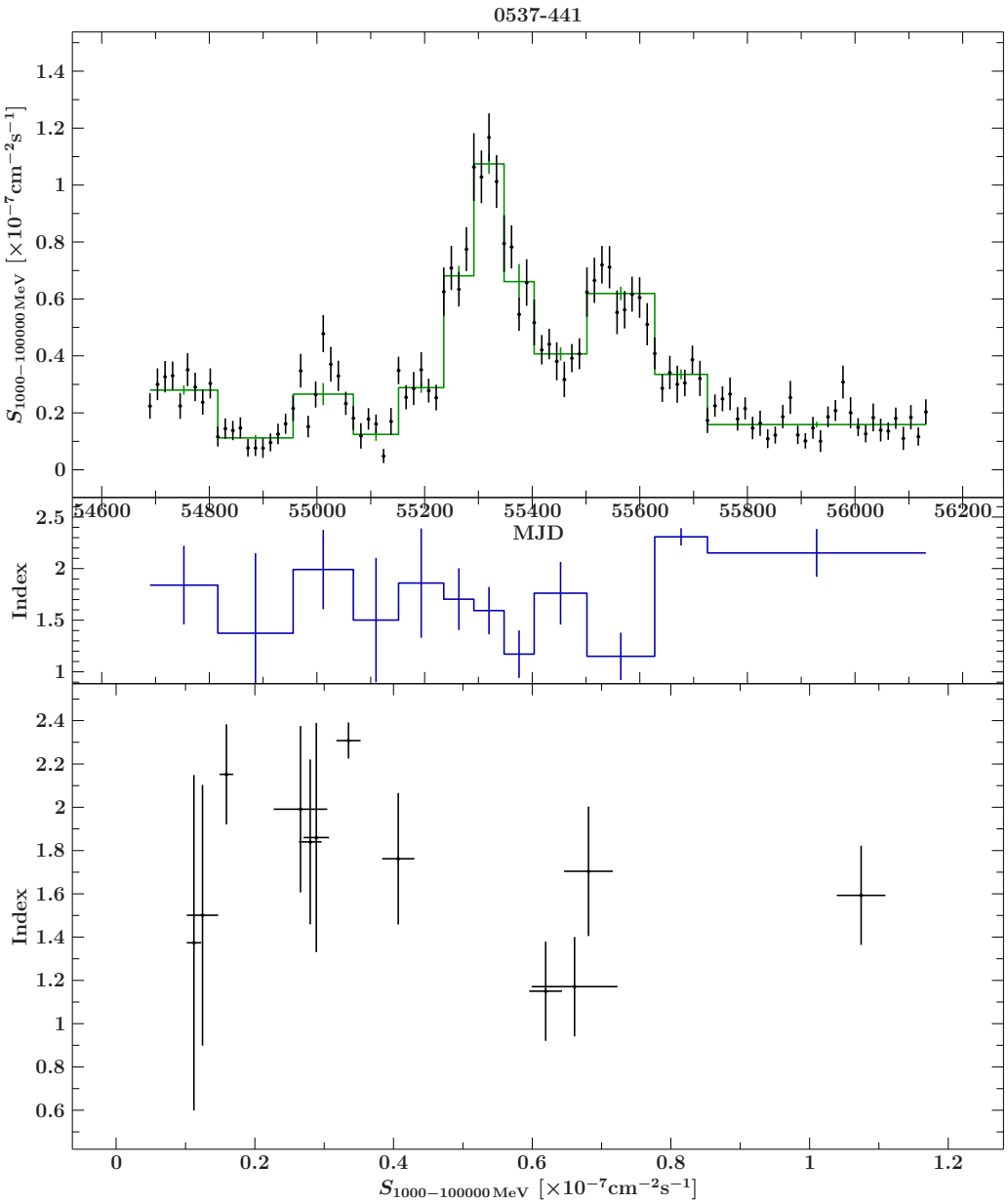

Figure 13: Upper panel: light curve of 0537-441 with the determined blocks (green). Mid panel: evolution of the spectral index over time resulted by the analysis of the block spectra. Lower panel: spectral index of the blocks plotted over their related mean flux of the block.

This can be summed up with the phrase, 'the brighter, the harder'. Another feature, beside the flux index relationship, is the decline of the spectral index in the block after the main peak, this may present a hint for lagging of the spectral index in this case, which might be evidence for a different or a special emission model.

The light curve of 0208-512 has two peaks, a smaller peak of 4 bins, 2 months and a larger peak of 13 bins and 6.5 months. The small peak is brighter than the larger one. The surrounded low flux time ranges are nearly on the same flux level (Fig. 15, upper panel). The low flux levels have a number of upper limits which are in the same range of the determined flux values of the low levels. The spectral index of the two peaks is lower than the one of the less active stages. The value of the first block is pretty uncertain with respect to the three bins of this

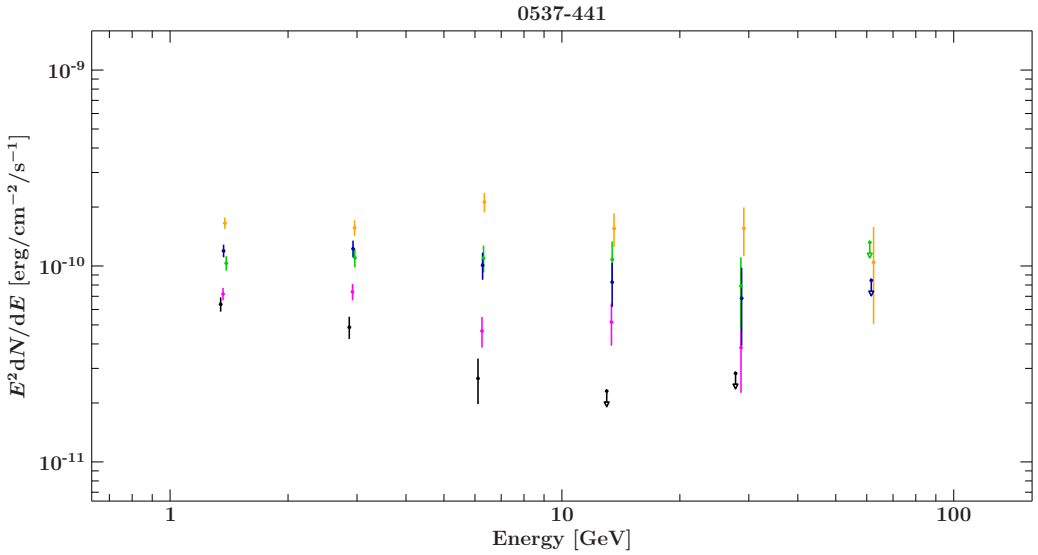

Figure 14: Block spectrum of the major peak of 0537-441 and the two blocks before and after the peak (From left to right in the light curve(black, blue, orange, green and magenta)).

block. The other values show more or less an anti-correlated connection of the flux and the index, which can be seen in a correlation-coefficient of $\rho = -0.506$. The source is part of both samples, the short flaring and the Bayesian blocks sample. In this context the smaller peak of 4 bins is associated as a short flare. The second peak rises in the same way but also contains bins with a low flux, this makes the peak broader and the mean flux is reduced. This peak is one example that demonstrates that the algorithm can only find one block through the size of the uncertainties. During the time range of the sample the source showed also flares in the optical and the infra-red wavelength (Chatterjee et al., 2013).

As contrasted with previous sources the source 0332-402 displays only one prominent flare which arises from a constant flux level and lasts a few bins, in this case 5 bins (Fig. 16, upper panel). The source owns some upper limits but these have no effect on the block representation. The spectral index evolution (Fig. 16, mid panel) shows an unexpected behaviour. It rises from a low index in the time of the peak to the maximum index and drops just little and stays above the index of the first low flux region although the flux drops back to the value before the flare. This may be effected by a change in the amount of the contribution of low energy γ-rays during and after the flare. Beside the Fermi and TANAMI monitoring the source was included in an infra-red monitoring campaign in 2011 (Nesci et al., 2013).

The source 0521-365 is also one of the Bayesian short flare samples. The light curve (Fig. 17, upper panel) has two constant areas in flux with no variations. These two rather less active time ranges are separated by one single flare. This flare is very short, the size is only one bin which corresponds to a maximum flare duration of 14 days. The spectral index (Fig. 17, mid panel) shows a constant behaviour. In the quiet time ranges the spectral index can be fitted to nearly the same value of $\Gamma \simeq 2.63$. In the flaring case the index drops to a value of $\Gamma \simeq 2.3$ but with a large error bar. This behaviour can be classified as anti-correlated with a correlation-coefficient $\rho = -0.993$, but for a more detailed conclusion more blocks are needed. The source shows a clear flare which is unusual during the light curve. The flare event was short and very powerful. After the flare in the γ-rays the source was part of an infra-red monitoring in 2011 (Nesci et al., 2013).

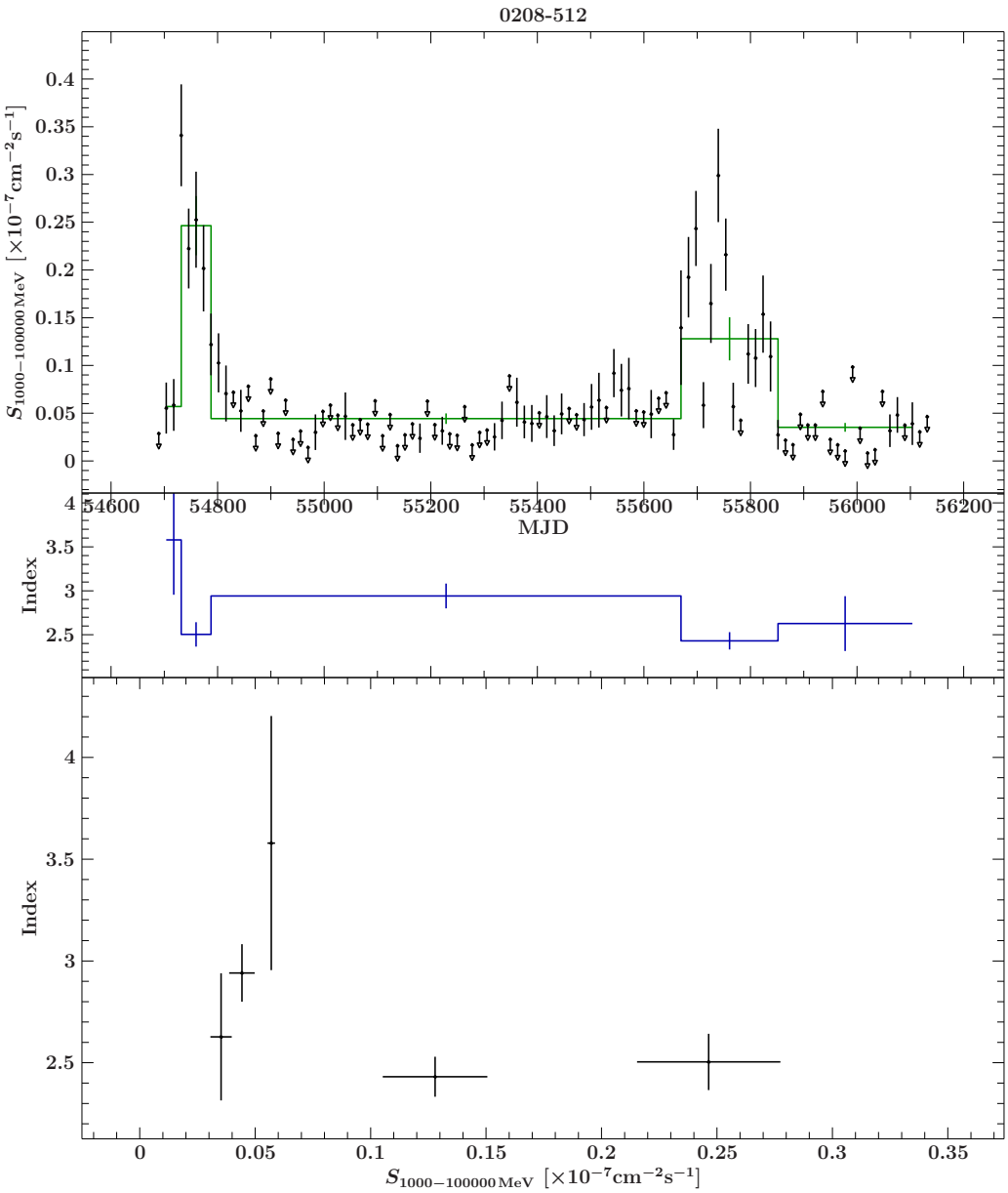

Figure 15: Upper panel: light curve of 0208-512 with the determined blocks (green). Mid panel: evolution of the spectral index over time resulted by the analysis of the block spectra. Lower panel: spectral index of the blocks plotted over their related mean flux of the block.

The source 1313-333 shows nearly the same behaviour as the source 0521. The light curve (Fig. 18, upper panel) has two constant time ranges but these ranges have many upper limits. The source is very weak in the γ-rays in the quiet stages, but the upper limits are of the same order as the flux points. The significant flare is of the size of 14 days and one bin. The flux of the flare is around 7 times greater than ground level flux. The evolution of the spectral index shows three different pictures. The first quiet range has an index of $\Gamma = 2.4$ and is around 0.3 lower than the index of the second time range. During the flare the spectral index shows the same behaviour as that of the source 0521, it decreases to $\Gamma = 2.2$. This is a hardening of the spectrum during the flare and the relationship seems anti-correlated with correlation-coefficient $\rho = -0.886$.

In contrast to the two sources described before, the source 1714-336 is different. The light curve

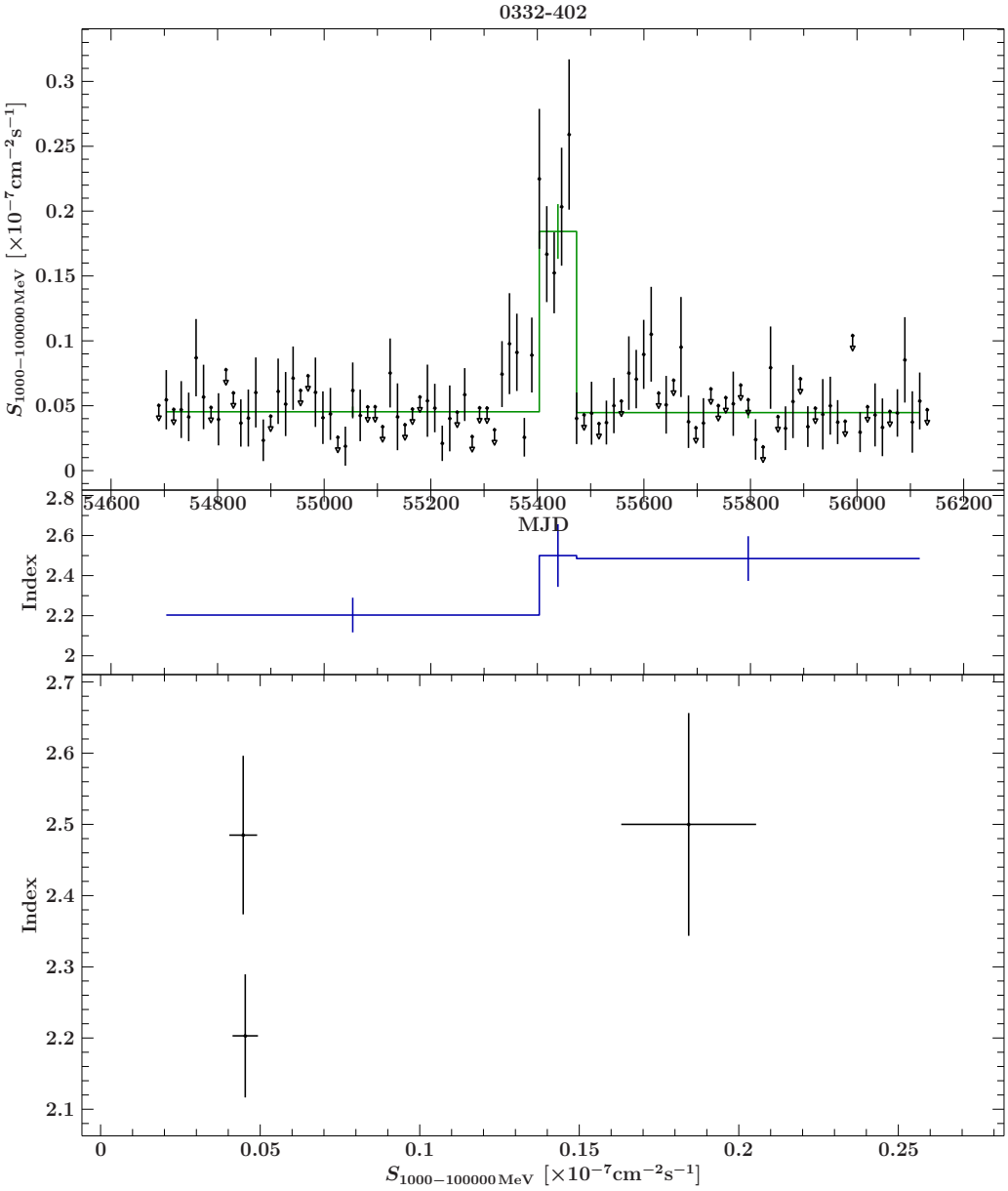

Figure 16: Upper panel: light curve of 0332-403 with the determined blocks (green). Mid panel: evolution of the spectral index over time resulted by the analysis of the block spectra. Lower panel: spectral index of the blocks plotted over their related mean flux of the block.

(Fig. 19, upper panel) displays that the source has a single flare which rises between two near constant flux ranges. The problem with this source is that many upper limits were calculated and many of them are much greater than the flux of the peak. This renders the mean flux of the quiet areas very uncertain. The spectral index evolves differently. The spectral index is softer in the flare and the flux index relationship shows a correlation, $\rho = 0.813$, not an anti-correlation like in the other source (Fig. 19, lower panel). This source is of a certain interest as it is in the source region of a detected neutrino event of the IceCube[8] detector (Krauß et al., 2014). According to the many upper limits and the certain interest, the reduction of the number of upper limits is one opportunity to get a more resolved picture of the source. The source is one part of the more detailed analysis in Sec. 4.3 concerning the upper limit problem.

[8]High energy neutrino telescope at the Amundsen-Scott South Pole Station

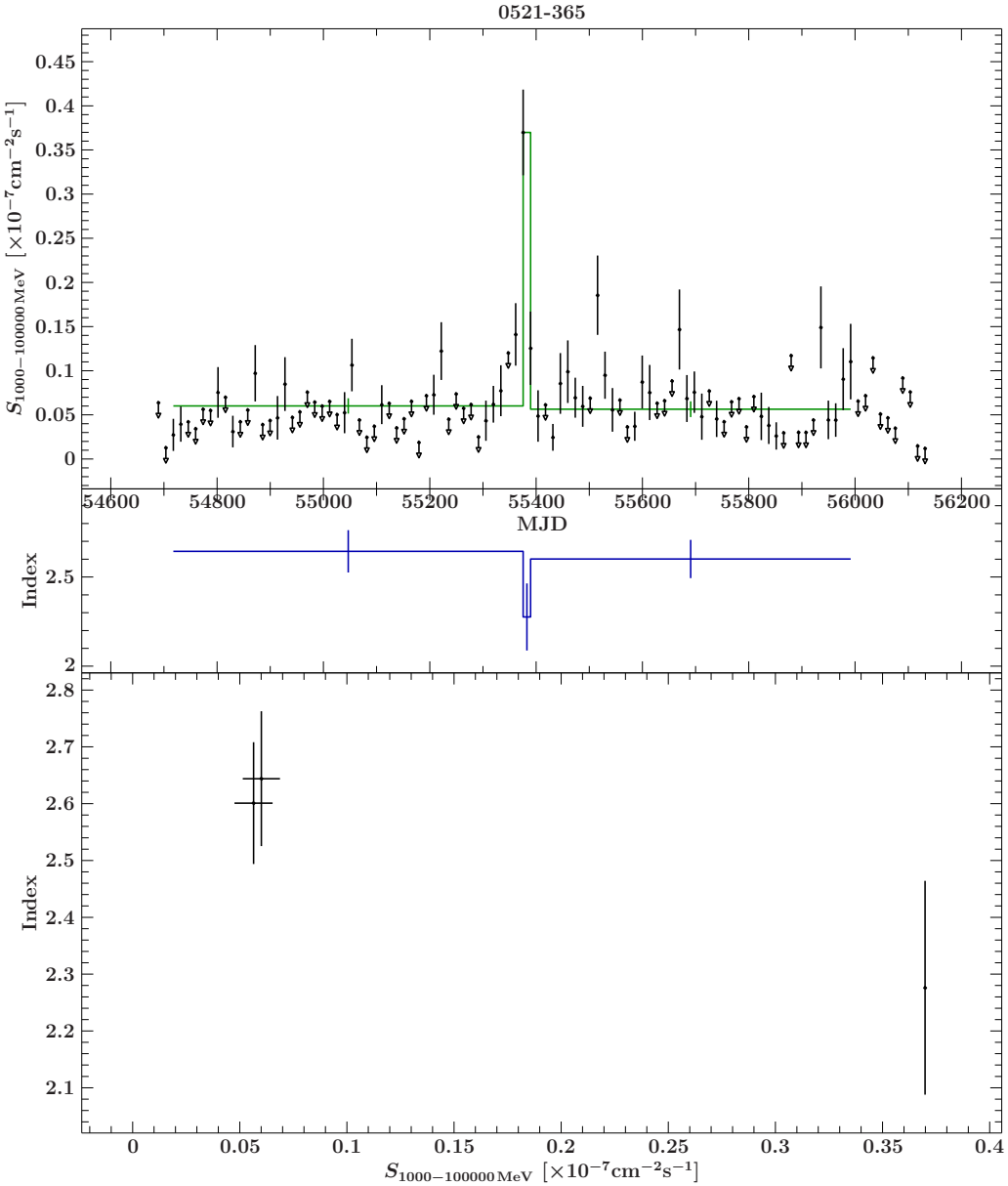

Figure 17: Upper panel: light curve of 0521-365 with the determined blocks (green). Mid panel: evolution of the spectral index over time resulted by the analysis of the block spectra. Lower panel: spectral index of the blocks plotted over their related mean flux of the block.

The source 2052-474 is a source with many upper limits. The light curve (Fig. 20, upper panel) has one peak raised from the ground level in the first block. Then the flux drops back to the ground level through an intermediate block. During the two blocks of the peak no upper limits were computed. The upper limits are part of the two major blocks which are considered as the ground level state. The spectral index evolution shows the well-known behaviour, when the source is brighter the index is lower. But in the peak block the spectral index drops to a value of $\Gamma = 0.6$ which is a very hard index and is not common for those sources. The result may depend on a bad fit in this block, low flux mostly corresponds to a low photon count rate from the source. Relating to the error of this value the highest index would be $\Gamma = 1.3$ which is still a hard index. The other spectral index values are in the common range and show the anti-correlated behaviour.

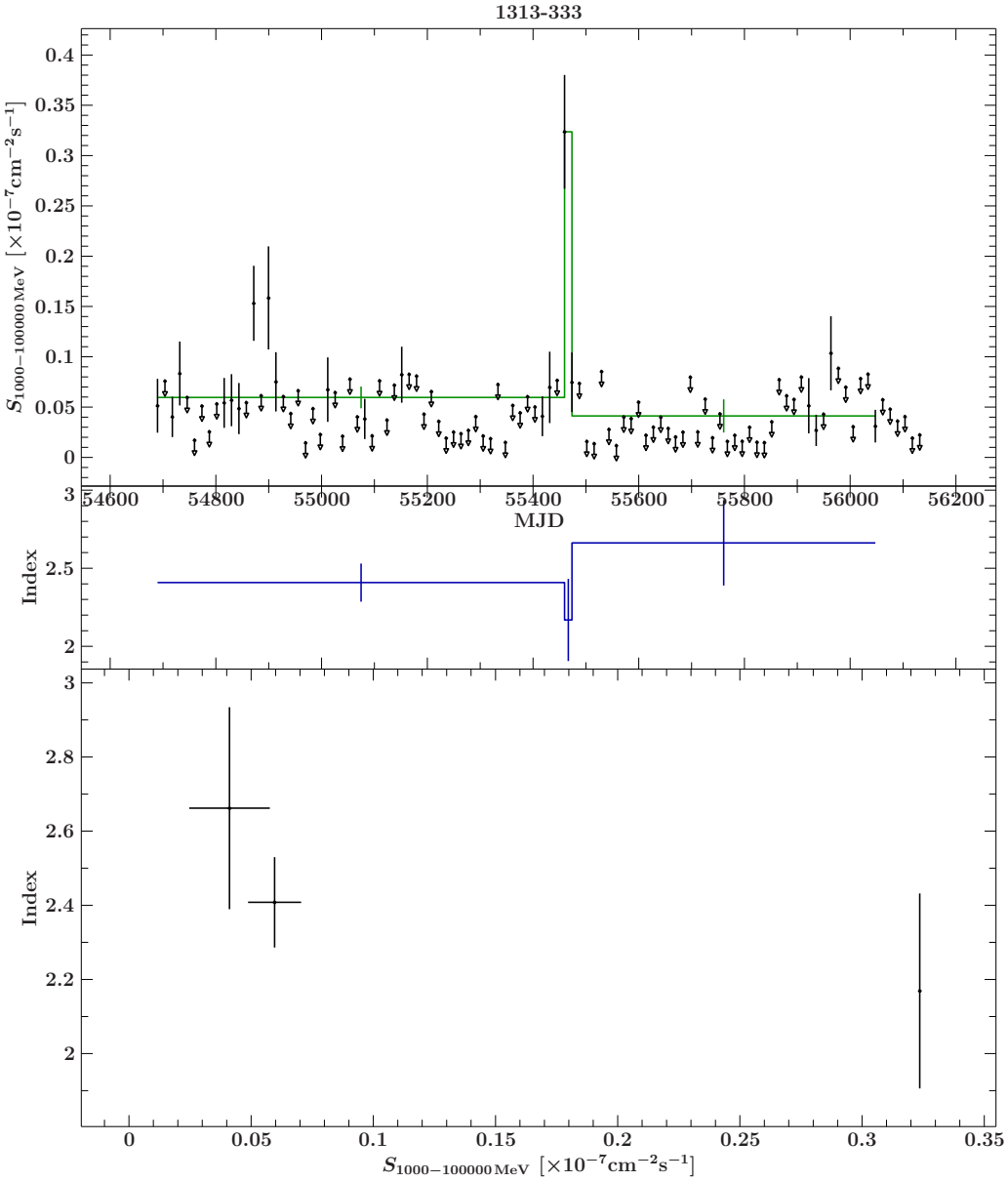

Figure 18: Upper panel: light curve of 1313-333 with the determined blocks (green). Mid panel: evolution of the spectral index over time resulted by the analysis of the block spectra. Lower panel: spectral index of the blocks plotted over their related mean flux of the block.

The source 2155-304 is sightly different from the sources presented before. The light curve (Fig. 21, upper panel) show variations in the light curve which are not detected by the algorithm. The four blocks demonstrate that three different long term flux levels can be detected. The second and the fourth block is the low level state, the first respects a high level and the third an intermediate level. The evolution of the spectral index (Fig. 21, mid panel) is nearly constant, the change of the index is just in the order of 0.1 during the time of the light curve. The source had prominent γ-ray flares in the past before the Fermi era (H.E.S.S. Collaboration et al., 2012). The large errors may be a reason for not detecting the visible variations. Enlarging the bin size or changing the energy range are possibilities to get a better picture of this source.

The other 12 sources were analysed in the same way. They contain sources of the Bayesian

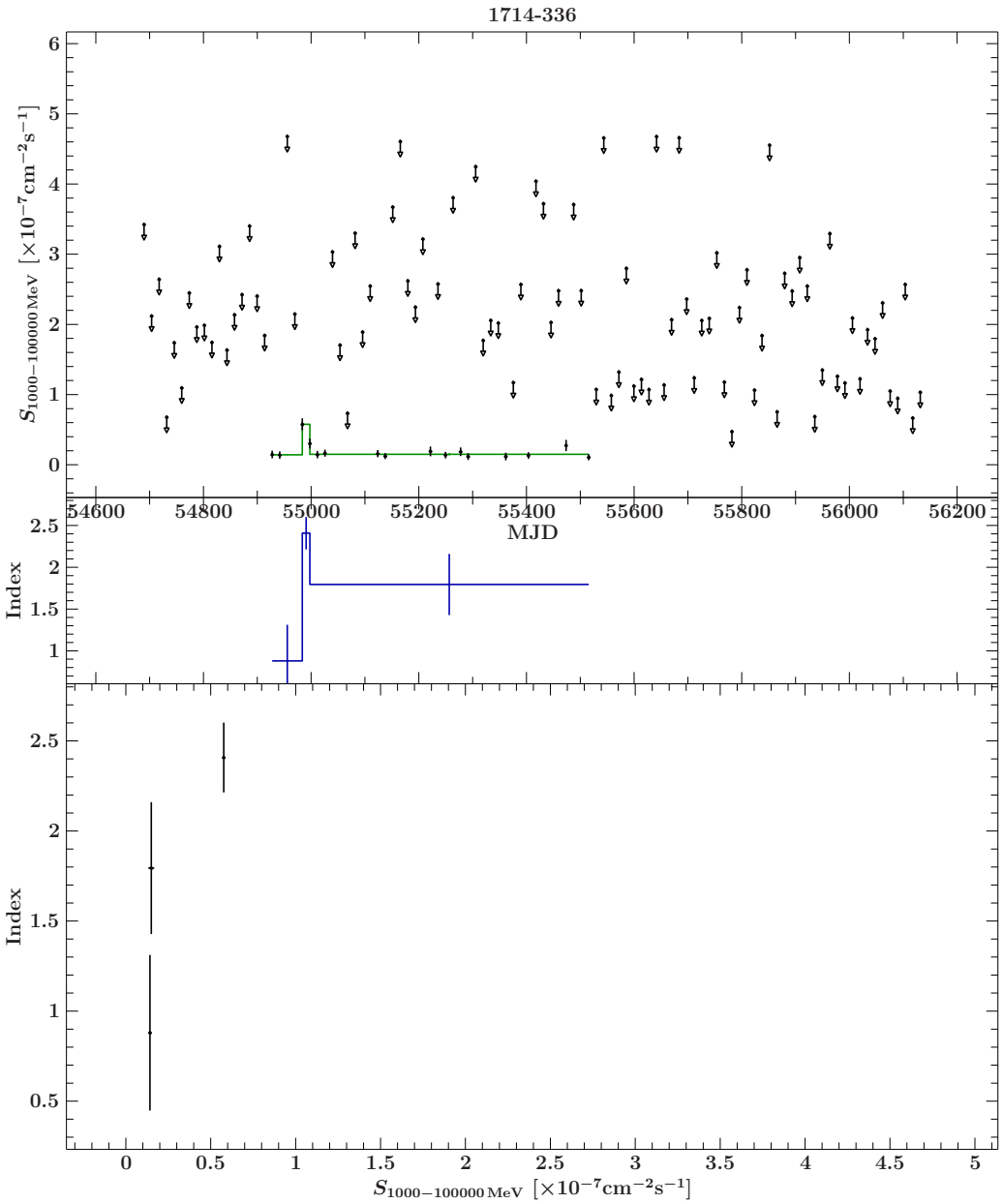

Figure 19: Upper panel: light curve of 1714-336 with the determined blocks (green). Mid panel: evolution of the spectral index over time resulted by the analysis of the block spectra. Lower panel: spectral index of the blocks plotted over their related mean flux of the block.

block sample and the short flare sample. The sources 0402-362, 1325-558, 1454-354, 1600-445, 1759-396, 2204-540, one half of these 12 sources have a high number of upper limits and the results of the analysis are less precise to get a further conclusion. In some cases a few blocks can be detected, in other cases only two blocks were found. The sources 2204-540 (Fig. 44), 2136-428 (Fig. 43), 1600-445 (Fig. 41), 1101-536 (Fig. 37) have only two blocks, in all cases one big block and small block mostly in the beginning of the light curves.
Three sources with many upper limits, 0402-362 (Fig. 34), 1325-558 (Fig. 38), 1454-354 (Fig. 40), have a flaring behaviour in their light curves in addition to this the sources 0244-470 (Fig. 33) have also a flare. Like the other flaring sources the sources have one single peak surrounded by two long time intervals with a constant low flux. The evolution of the spectral index in these sources is mainly constant. The values vary just about 0.2 to 0.3. The two general relationships

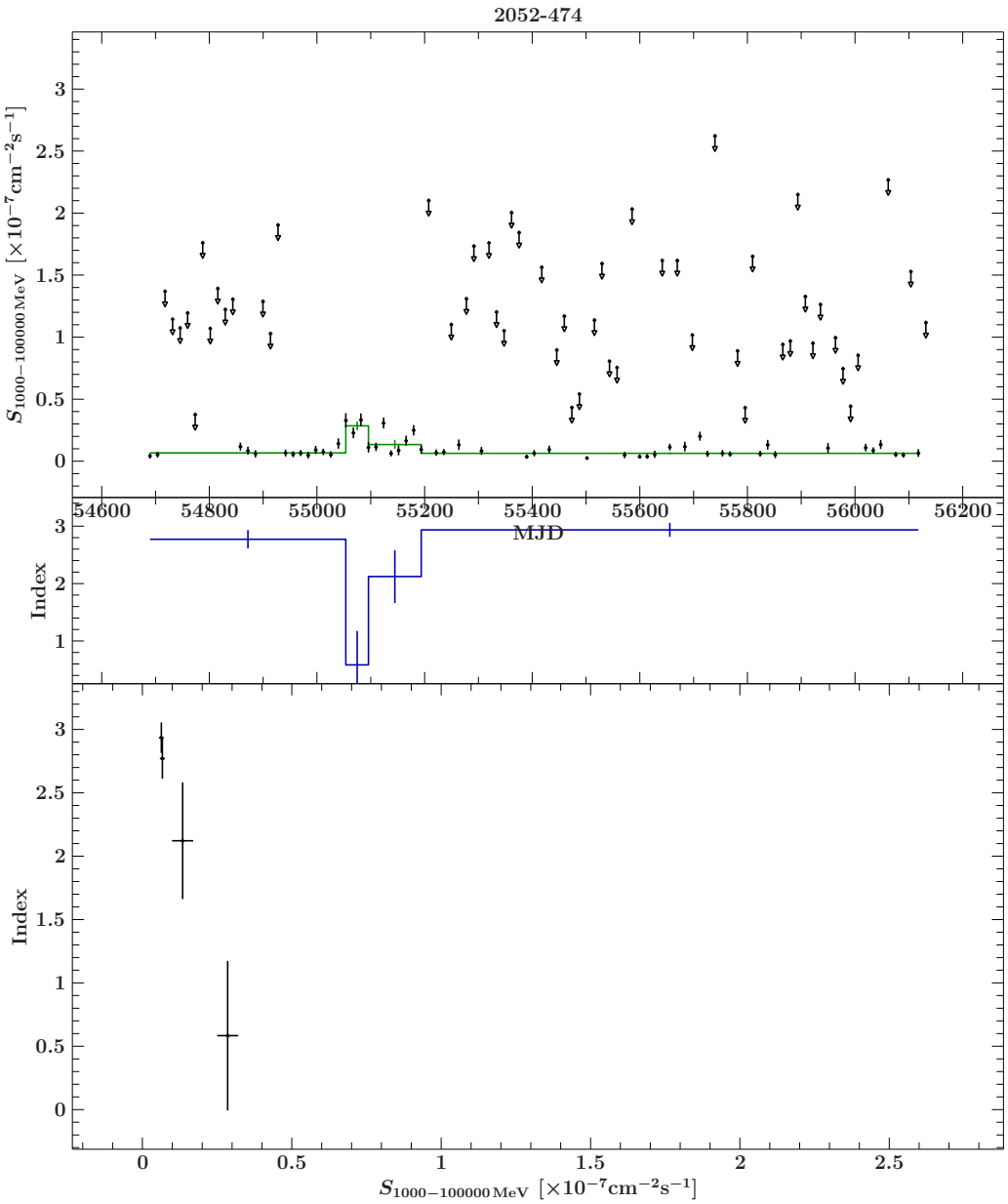

Figure 20: Upper panel: light curve of 2052-474 with the determined blocks (green). Mid panel: evolution of the spectral index over time resulted by the analysis of the block spectra. Lower panel: spectral index of the blocks plotted over their related mean flux of the block.

which are pointed out in the first 8 sources, the correlated and the anti-correlated behaviour of the spectral index and the flux, are not visible in these sources. The main behaviour is that there is no clear correlation between these two parameters.
Some sources, 0426-380 (Fig. 35), 1424-428 (Fig. 35), 1759-396 (Fig. 35) show more blocks than two or the three blocks in the flaring sources. Their light curve evolution is comparable to the light curve of 0537-441. Especially 0426-380 and 1424-428 with a low number of upper limits show good examples for sources with variation. The spectral index variation can be found and some hints for possible correlations of the flux and the index are given. 1759-396 has more upper limits but in a short time window some blocks with tiny variations could be detected. The spectral index seems anti-correlated with flux but the errors of the index are not small and can influence the picture of the relationship.

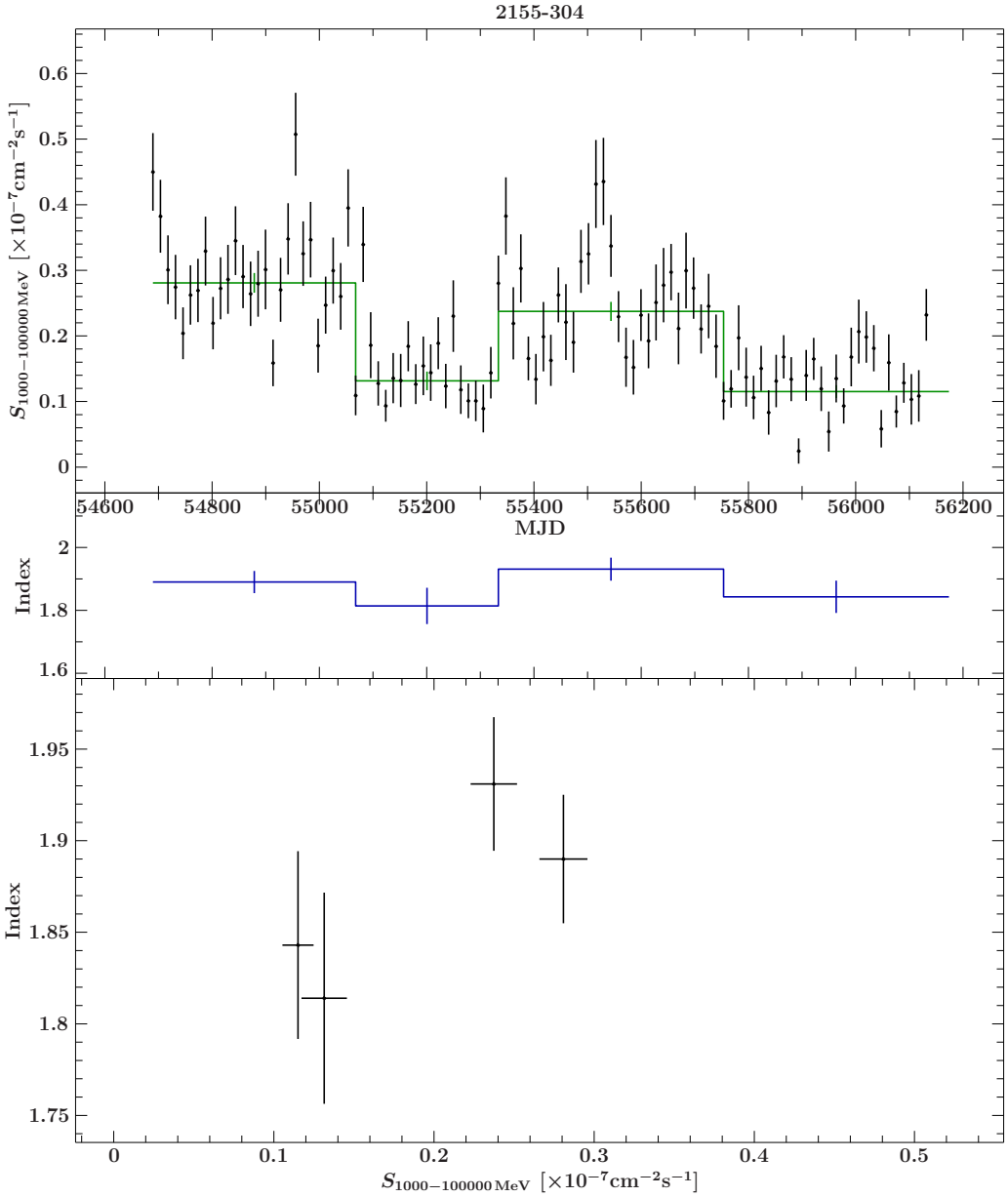

Figure 21: Upper panel: light curve of 2155-304 with the determined blocks (green). Mid panel: evolution of the spectral index over time resulted by the analysis of the block spectra. Lower panel: spectral index of the blocks plotted over their related mean flux of the block.

According to this the last investigated light curve of the source 0447-439 (Fig. 36) demonstrates that the light curve is similar to the light curve of 2155-304. Only four larger blocks with small variations were found through the algorithm.
The mentioned light curves with their spectral evolution can be find in the appendix.

Global Properties The individual source analysis can lead to a better understanding of the general system of blazars. The relationship of the flux and the spectral index show in some cases a correlated, in other cases an anti-correlated or uncorrelated behaviour. There is a trend for all the sources although, the different emission mechanism contribute in different rates. The spectral index of each is plotted over the determined flux of the block of each source in the sample in one diagram (Fig. 22). The spectral indices of the sources below a flux of

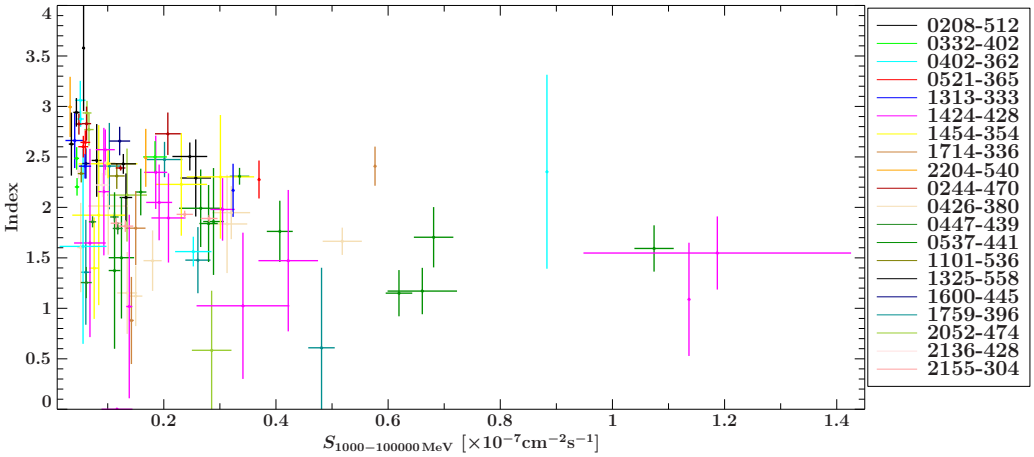

Figure 22: Global relationship of spectral index and flux for all 20 source of the Bayesian sample. Each spectral index of each block is plotted over corresponding mean flux of the block.

$S_{1-100\,\mathrm{GeV}} = 0.5 \cdot 10^{-7}\,\mathrm{cm}^{-2}\mathrm{s}^{-1}$ are distributed in the range of $\Gamma = 0.6$ to $\Gamma = 3.6$. The indices below $\Gamma = 1.5$ have large errors and are not very physical results for a spectral index of an AGN, this might be correlated with a fit in the block spectra concerning many upper limits and through this a low photon count rate in the raw data file of the block. The main population of the index is in the range of $\Gamma = 2.0$ to $\Gamma = 3.0$. The clearly decreases with increase of the flux, at a flux of $S_{1-100\,\mathrm{GeV}} = 0.1 \cdot 10^{-7}\,\mathrm{cm}^{-2}\mathrm{s}^{-1}$ the limit is $\Gamma = 3.0$ and decreases to $\Gamma = 2.0$ by a flux of $S_{1-100\,\mathrm{GeV}} = 0.5$. This feature can be combined with the anti-correlated evolution of the spectral index in respect to the flux, which is detected in some sources. The upper limit follows the trend of "the brighter, the harder", i.e. if the flux of the source rises the amount of high energy photons take a larger part in the spectrum of the source. The lower limit of the spectrum is nearly constant in the range of $\Gamma = 1.3$ to $\Gamma = 1.5$ if the few values which seem very uncertain and unphysical are neglected.
In the analysed energy band only 8 blocks reach a flux greater than $S_{1-100\,\mathrm{GeV}} = 0.5 \cdot 10^{-7}\,\mathrm{cm}^{-2}\mathrm{s}^{-1}$ and the spectral index is below $\Gamma = 2.0$ apart from one value of 0402-362 with a large uncertainty. The global result is that the upper limit of the spectral index declines during the rise of the flux. But the lower limit of the spectral index is of the same order during the most flux levels. Therefore low energy γ-rays are only the major part in some blocks with low flux, the higher the flux the more dominant are the high energy photons and lead to a shift of the spectrum to higher energies.

4.3 Upper Limit Problem

Some sources of the sample appear very weak in the γ-rays and in their light curve many upper limits were computed. The calculation of an upper limit is triggered by the calculated TS-value in the likelihood fit. If the TS-value fails on the TS threshold an upper limit will be calculated. Due to the neglect of upper limits in the Bayesian block script the number of bins per light curve are significantly reduced. The upper limit appearance in the source can be divided into two parts, the upper limits are of the dimension of the flux bins or they are one order or more above the calculated flux. In the first case the upper limits do not hide any peaks, only small variations on longer time scales. The second case is much more prominent to hide peaks, not bright flares. Those will push the TS statistic over the upper limits threshold and lead to a clear source detection in the flux bin. Small flares that rise from a flux level of the source where the source barely can be detected through the fit, might not reach the TS threshold and still an

upper limit is calculated.
In some bins of some sources the incoming photons are so few that the likelihood fit can not detect the source through the photon reconstruction and the calculated TS-value is negative. This is the fact when the model with an additional source is more probable than the model without. This is not affected by the choice of minimizer, all available minimizers of the Fermi tools have the same result in those cases and cannot detect the source. The light curve script ignores those bins and they get lost to analyse them.

There are two possible solutions to tackle this problem. The first solution is to extend the energy range and take the full energy range (100 Mev-300 GeV) of the LAT instrument and compute a new light curve and analyse it again. This method especially takes more soft γ-rays into account and the flux of the source is enhanced.
The other possibility is to switch off the upper limit calculation and compute the flux of the bin which is often related with a large error. As mentioned in Sec. 3.3, a larger error has an effect on the Bayesian analysis. This method is based on the light curve calculation employed by Böck (2012) in his PhD-thesis.
The two methods can be used together when the extent of the energy range only has a small effect on the increase of the number of upper limits, the light curve can also be computed without the upper limit calculation.

4.3.1 Results

Both methods were applied to five sources with many upper limits in their light curve in the best energy band. The sources 0402-362, 1325-558, 1714-336 and 2052-474 have light curves where the upper limits are not on the same level of flux as the bins that could be computed. This feature may hide some blocks.

The light curves show, as expected, more blocks in the full than in the good energy range. Furthermore the light curves without the upper limits calculation also have more blocks concerning more useful bins in the light curve itself and some very small calculated flux bins.
The light curves of 0402-362 change a bit. The full energy light curve has a more cleaner block representation. The most upper limits are gone, just a few at the start of the light curve are left over. The two flares are still there and three other flares appear in the light curve. The same result is given by the full energy light curve with no upper limits. There an extra block with a very low flux appears in the beginning. The good energy light curve without upper limits is an improvement as well, but only the small broad block after the major single bin flare appears there. For this source the analysis should be done with the full energy light curve, including the upper limits might not change much.

The good energy light curve of 1325-558 with no upper limits has five blocks, two more than in the light curve with upper limits. Before the peak the flux drops to almost zero in some bins, these values have small errors and the higher flux values are neglected by the algorithm. After, the peak drops to a low level and rises again to the plateau similar to the third block of the light curve with upper limits. The full energy light curve shows a new peak in the plateau after the first peak. The upper limits after the peak are evidence for the drop of the flux that can be seen in the light curve without the upper limits. This light curve also has some variations in the time range before the flare resulting from very low flux bins with small errors. The new peak may have to do with the broader energy range. Therefore the source is also analysed in the full energy range to determine its spectral properties. The results are pointed out in the following.

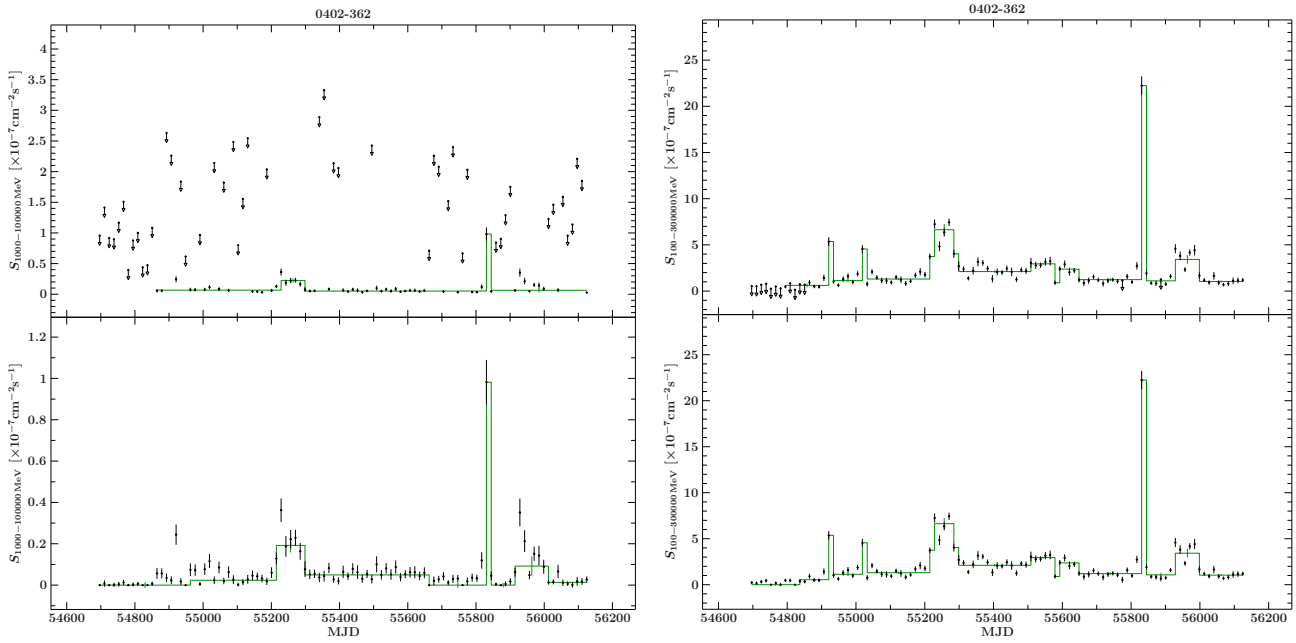

(a) 1-100 GeV (b) 0.1-300 GeV

Figure 23: Different light curves for 0402-362 with Bayesian blocks for the standard light curve (upper panel) and the light curve without upper limits (lower panel).

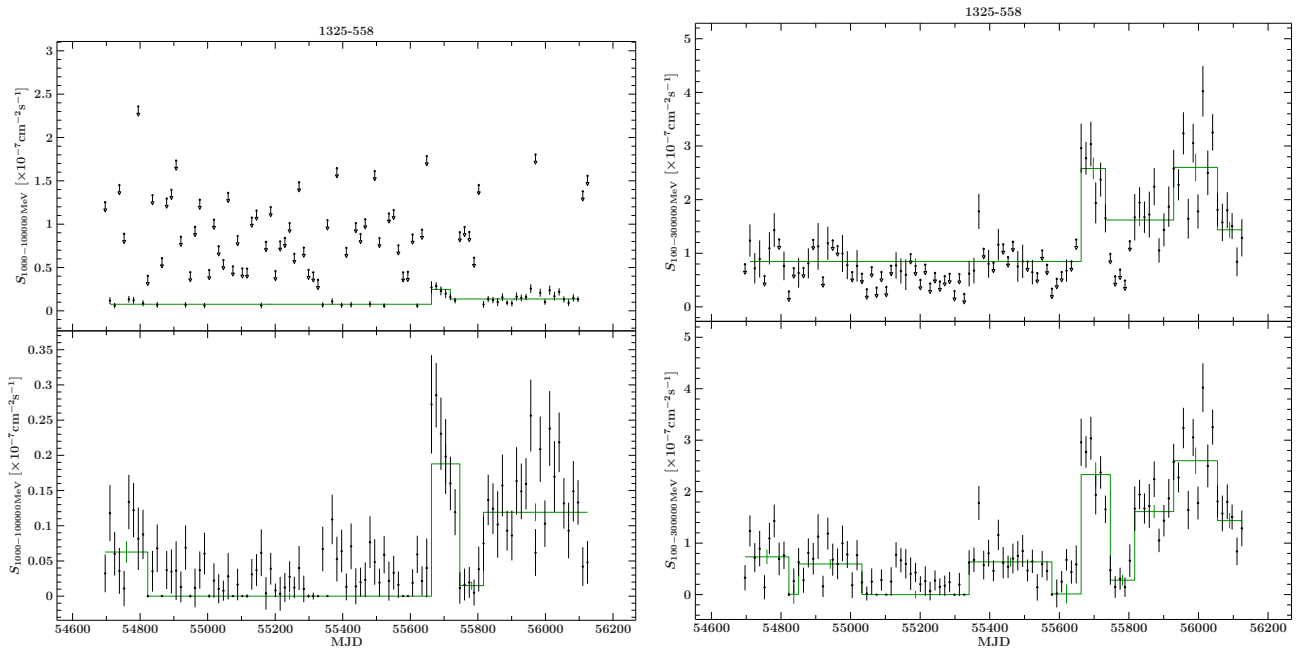

(a) 1-100 GeV (b) 0.1-300 GeV

Figure 24: Different light curves for 1325-558 with Bayesian blocks for the standard light curve (upper panel) and the light curve without upper limits (lower panel).

1714-336's light curves show all the prominent big single bin flare, only the rise of the flare changes a bit. The flux rises from a very low level to the block before the peak, this is effected by the existing upper limits in the original light curve. The full energy light curve has the same appearance of the flux evolution. In the last half, the light curve is dominated by upper limits. This leads, in the upper-limit-less version, to the finding of two additional bins. These bins are broad and the mean values are in the lower flux levels. The source is also analysed in concern of

the spectral properties especially in the block before the flare. The spectral parameters should be the same caused by not changing anything in the light curve depending on the energy range.

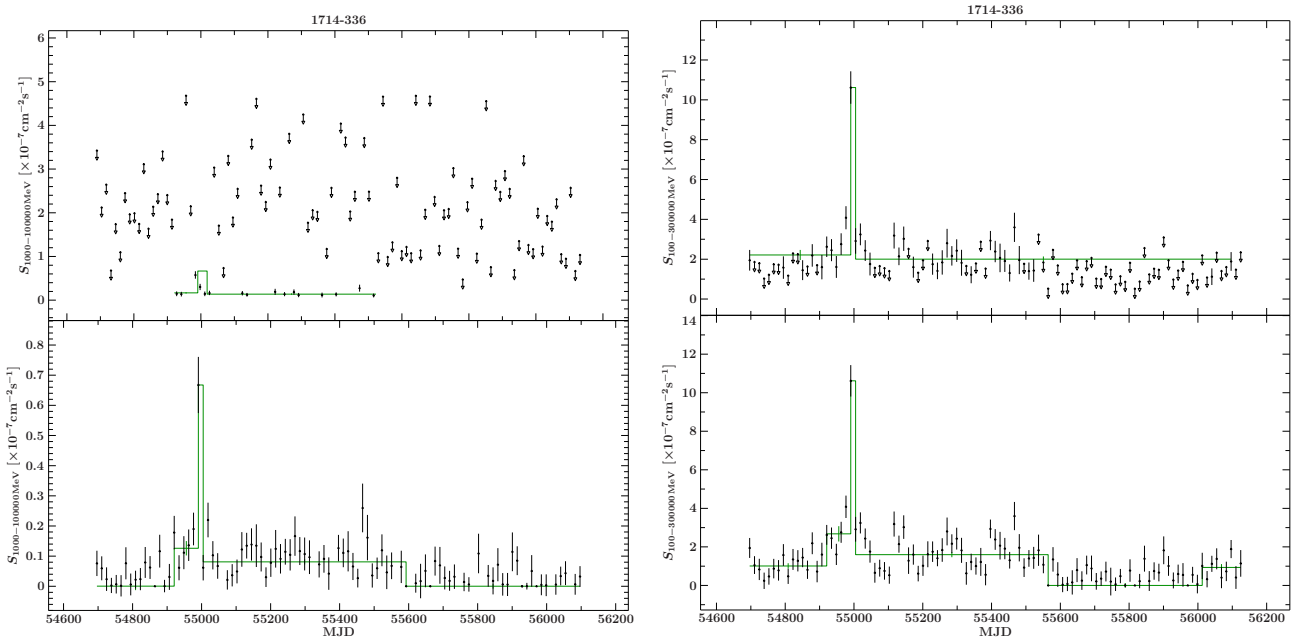

(a) 1-100 GeV (b) 0.1-300 GeV

Figure 25: Different light curves for 1714-336 with Bayesian blocks for the standard light curve (upper panel) and the light curve without upper limits (lower panel).

The light curve of 2052-474 without upper limits still has the flare and the after-flare block before the flux is back on the ground level. The ground level is disturbed by three blocks, where the algorithm is dominated by flux points near zero. The full energy light curve has also the flare and the after flare block. Beside this a pre-flare appears, which might be effected by softer γ-rays. In the second half, the two different alternating ground levels are visible. In the full energy light curve without upper limits the influence of neglecting the upper limits is pointed out. There, a small peak appears after the lower block created by the newly calculated two upper limits. In this case the two new bins have a lower flux and the algorithm determines a probability for two new blocks, the dip and the peak in the light curve.

The spectral properties of the two sources 1325-558 and 1714-336 were analysed for the four different light curves.
The relationship of flux and spectral index in 1325-558 is in the most cases pretty even. The spectral index in the good energy range without upper limits is in the range of $\Gamma = 2 - 3$ only two bins with large errors are not in this range. A correlation or anti-correlation is not seen. The same picture is shown in the full energy range with upper limits. The spectral index just changes around 0.3 and a clear relationship between flux and spectral index is not pointed out. The evolution of the relationship changes only in the full energy range without upper limits, where the spectral index changes also around 0.3 but the values for higher fluxes are lower than the values for a lower flux. This might be evidence for an anti-correlated behaviour ($\rho = -0.745$), but it has to be taken into account that this is a result of a calculation without upper limits an the uncertainties are not small in this case.
The spectral evolution of 1714-336 has a correlated behaviour, when the flux increases the spectral index increases. This feature is always there in the good energy range without upper limits, where some index values with large errors appear concerning the low flux of the block.

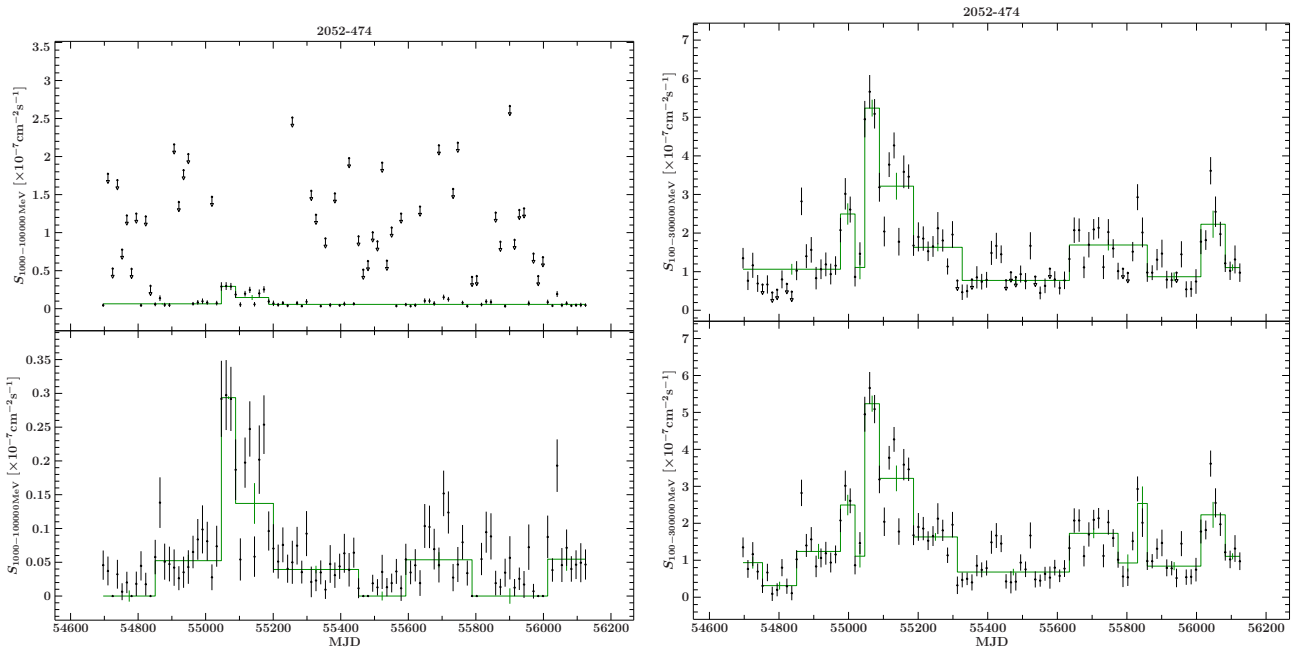

(a) 1-100 GeV (b) 0.1-300 GeV

Figure 26: Different light curves for 2052-474 with Bayesian blocks for the standard light curve (upper panel) and the light curve without upper limits (lower panel).

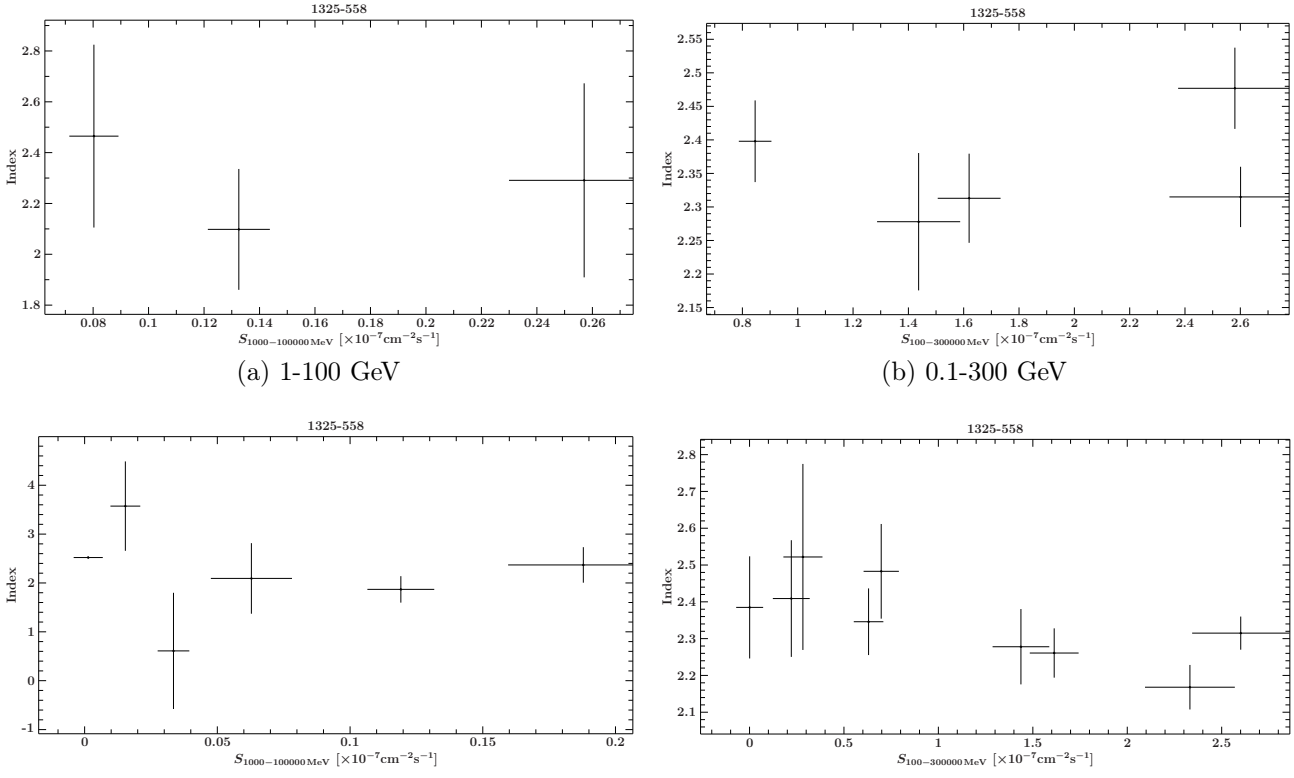

(a) 1-100 GeV (b) 0.1-300 GeV

(c) 1-100 GeV(no UL) (d) 0.1-300 GeV(no UL)

Figure 27: Spectral index over flux for the different light curves of 1325-558

In addition to this the feature is there in the light curve of the full energy range. In contrast to the good energy light curve the index values are grater than $\Gamma = 2.2$ and the spectral index of the peak has very large error. The only change of the correlated behaviour can be found in the

full energy range without upper limits, the correlation-coefficient becomes negative ($\rho = -0.23$). When the very high index point with the large error is neglected. Than the spectral index on the lower flux levels is higher than during the intermediate flux levels and rises again in the peak bin. This leads to to different connections. First an anti-correlated behaviour between the low and the intermediate flux level. Second a correlation connection between the intermediate and the high flux level. This might be caused by a change of the emission model or the dominant emission process.

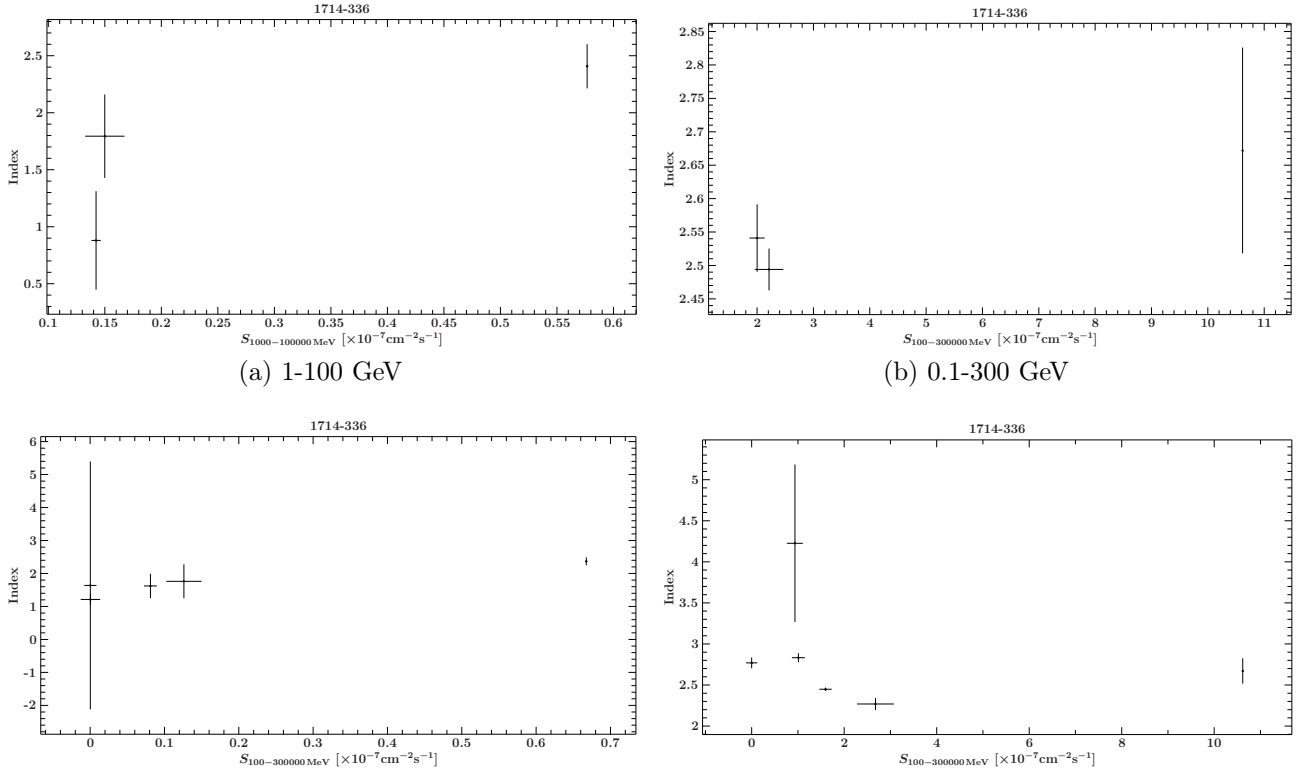

(a) 1-100 GeV

(b) 0.1-300 GeV

(c) 1-100 GeV(no UL)

(d) 0.1-300 GeV(no UL)

Figure 28: Spectral index over flux for the different light curves of 1714-336.

It is shown that the upper limit problem can be solved through these methods, by applying one or the two together. A change of the energy range is the best opportunity to get a more detailed picture of the time evolution of the AGN sources, which are faint in the good energy interval. In addition to this the not calculation should only be used when the source in the full energy range still has a large number of upper limits. Furthermore, in the case of 1325-558 the method with no upper limits show its quality. After peak the flux drops and rises again, only without upper limits this drop can be represented by a block through the algorithm.

4.3.2 Block Light Curve

The light curves generated by the script uses the fixed spectral properties for each source taken from the 2FGL-catalogue. The spectral properties are fixed over the entire time range of the light curve. But this is not true the spectral properties fluctuate during the time range as it can be seen in Sec. 4.2.2. The results of the source analysis with the Bayesian block algorithm can be used to recalculate the light curve taking the different spectral properties of each block into account.
The results of the block spectrum is used as the input spectrum for the new calculation of a light curve with a time range, which corresponding to the the time width of the block. When

this is done the block light curves can be combined to the full light curve and can be compared to the standard light curve.
An other possibility is not to fix the spectral properties during the standard light curve computation. For example, the spectral index is handled like a free parameter and is fitted in each bin. This method is only useful with bright sources like 0537-441. In faint sources an additional free parameter increases the uncertainties and leads to bad results.

0537-441 The source 0537-441 is a bright source and the computation of a light curve with the spectral index as a free parameter is possible. The compression of the standard light curve and the free index light curve show that the changes in the light curve are not large. But the flux in the two major peaks is reduced in respect to the change of the spectral index during these peaks. The decrease of the second is stronger in the free index light curve (Fig. 29a).
The block light curve show the same picture, the peak fluxes are reduced but the general shape of the light curve is still there. Beside this in some cases the flux is computed higher in the first drop and during the pre-flare (Fig. 29b).

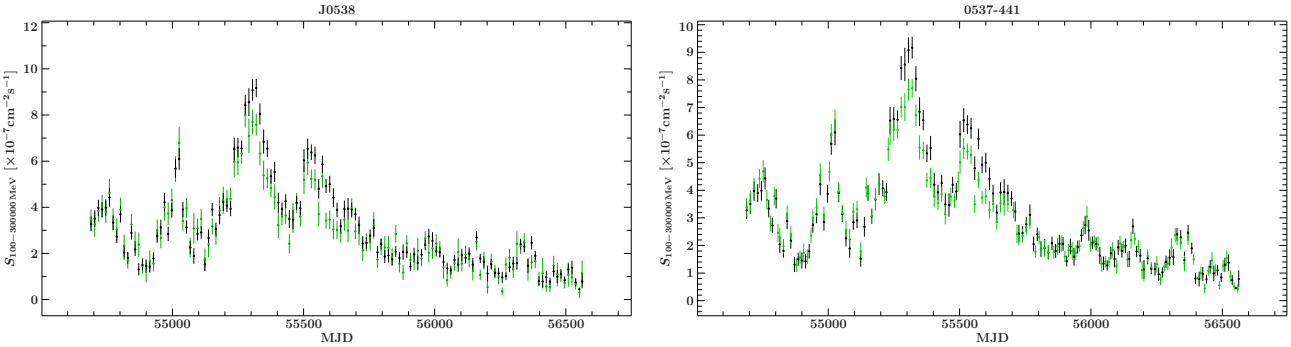

(a) (b)

Figure 29: Comparison between the standard light curve (black) and the recalculated light curve (green) of a calculation with a free fitted spectral properties (left) and the results of the Bayesian analysis (right).

The results of the two light curves point out that the standard light curve show the real time evolution of the flux, but some flux values are over- or under-calculated in some cases during great changes of the spectral properties. The standard light curve is a good starting point to study the time evolution of the flux. A more detailed picture can be reached through a Bayesian analysis of the standard light curve and the calculation of a Bayesian block light curve.

1325-558 The advantage of the block in the source 1325-558 is to limit the upper limits to a lower flux and reduce the total number of those. In the good energy range only the block light curve based on the standard light curve without upper limits can limit some upper limits to lower flux values. The other block light curve enlarges some upper limits instead. The flux before the peak at 56680 MJD is limited to flux values below the peak flux. This is done to around 200 days before the peak. But also some bins in the block light curve of the standard light curve without upper limits can not be calculated due to negative TS-values (Fig. 30).
Nevertheless the full energy light curves show nearly the same flux evolution. The block light curve based on the light curve with upper limits has higher flux values than the standard light curve. Opposed to this the flux based on the light curve without upper limits is lower than the standard flux and some upper limit calculations could be prevented. A new block after peak is the results of one computed flux bin. In the standard light curve only upper limits were

calculated in this new block, thus the block is non-existent.
The advantages are very small for this source but the single flux bin in the dip of the light curve can give us a better block representation where blocks are hidden by upper limits.

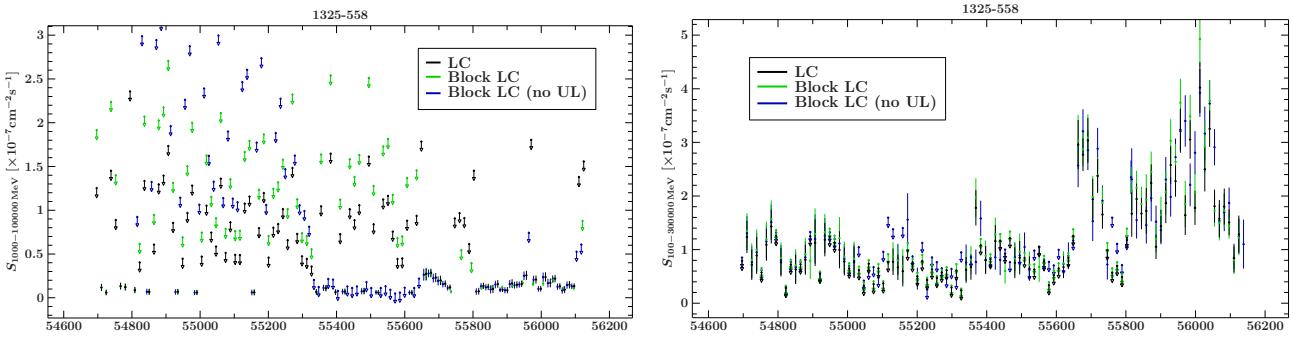

(a) $1 - 100\,\mathrm{GeV}$ (b) $0.1 - 300\,\mathrm{GeV}$

Figure 30: Comparison between the standard light curve (black) and the recalculated light curve of the analysis with upper limits (green) and without (blue).

1714-336 In the good energy range the free index light curve appears very strange, some bins are fitted very badly, some upper limits are around a factor of 2000 greater than the flux of the peak in the standard light curve (Fig. 31). In contrast the full energy free index light curve is better looking. The flux evolution and the upper limits appear just like in the standard light curve. But some holes in the light curve are clearly visible, the source cannot be detected in these bins. This is caused by the free spectral parameters, as they enlarge the uncertainties and reduce the TS-values to negative values, if the TS-values are already very low.

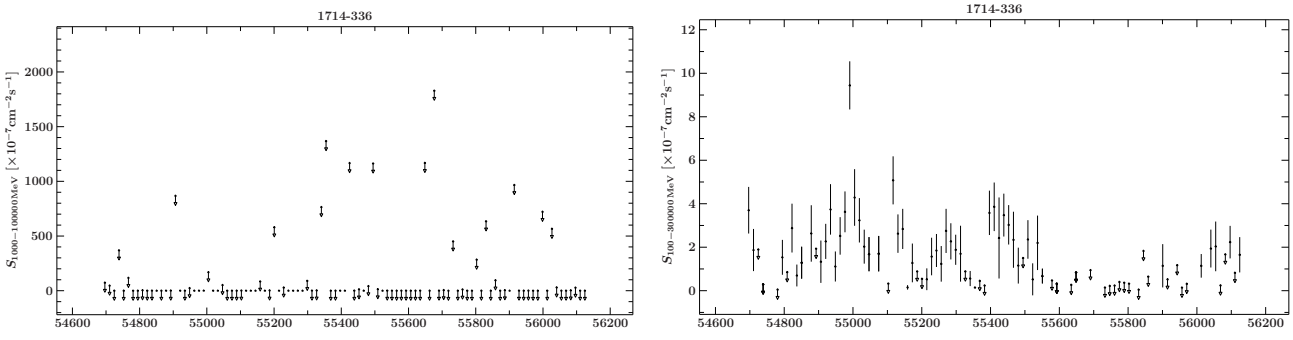

(a) (b)

Figure 31: Comparison of the different light curve calculated with a free spectral index in an energy range of $1 - 100\,\mathrm{GeV}$ (left) and $0.1 - 300\,\mathrm{GeV}$ (right).

The block light curve can be calculated in all cases, good and full energy range, with and without upper limits. The computed light curve show that the improvements in these light curve are the decrease of the upper limit values. Especially the good energy light curves have many upper limits which are still larger than the main single peak but the global values are reduced by a factor of 5 (Fig. 32). In the full energy range some flux bins show a change in their values and a few upper limits in the standard light curve can be calculated as a normal flux bin. The number of upper limits is still large but the results illustrate that the effects are based on the low count rate of source photons and not on the fixed spectral parameters.

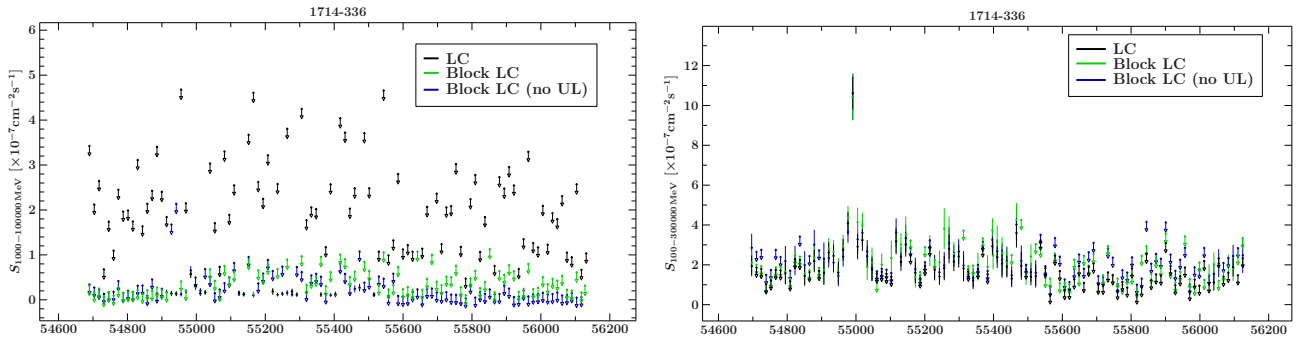

(a) $1 - 100\,\mathrm{GeV}$ (b) $0.1 - 300\,\mathrm{GeV}$

Figure 32: Comparison between the standard light curve (black) and the recalculated light curve of the analysis with upper limits (green) and without (blue).

5 Conclusion

The method of Bayesian blocks is a well known technique for analysing data sets in respect of variation. The Bayesian algorithm determines the constant parts of a data set and represents them via blocks. The blocks added together result in a histogram-like representation of the data set. In this thesis the general Bayesian approach is described (Sec. 2.2) and the algorithm of Scargle et al. (2013) is used. The improvement of the new algorithm (Scargle et al., 2013) in comparison to the former algorithm of Scargle (1998) is that the new code can handle Gaussian distributed data sets. The old code can only handle Poisson distributed data, whereas the new code can handle both. The old algorithm is the basis of many different functions that analyse astrophysical data sets, e.g. the Fermi science tool *gtburstfit* or the sitar-function of ISIS. Although there are good tools available, they only handle Poisson distributed data.
The Fermi light curves are not Poisson distributed data, their statistics are governed by the Gaussian distribution. Therefore the old tools are useless for this kind of data, whereas the new algorithm can handle them and the opportunity is given that the Fermi light curve can be investigated systematically with the Bayesian block method. In the case of Poisson distributed data the new algorithm works as well as the old one (Sec. 3.1). Both the new ISIS-function *bayesian_blocks* and the sitar-function were tested on the same light curve.

The examination of the bin size of a Fermi light curve (Sec. 3.2) and of the different internal and external parameters (Sec. 3.3) pointed out that the algorithm is very sensitive to the uncertainty σ of data binning. The increase of the bin size leads to the increase of the number of determined blocks (Tab. 3). This is correlated with the small decrease of the errors, which can be seen in Fig. 12 and Tab. 6. When the errors change only around 10%, one block appears or disappears. The influence of the *ncp_prior* of the block number can not be found when the bin size is changed. The *ncp_prior* has only an influence on the block number when the number of bins per light curve is constant. This value is not independent. Between the number of bins, *ncp_prior* and the false positive rate a relation exists (Fig. 8 and Eq. 2.18) and renders an independent parameter examination difficult (Sec. 3.3). The best agreement is achieved on using the default values, the *ncp_prior*-function (Eq. 2.18) with a false positive rate of 0.05 in the case of Gaussian distributed data. For the Poisson data a different *ncp_prior*-function (Eq. 2.11) is available, which allows a more defined parameter setup.

With this new algorithm the 55 sources of the TANAMI-project with association in the 2FGL-catalogue were analysed (Tab. 8). In 20 sources variations were found and the light curves were further analysed. Nine of these 20 sources are members of the short flare selection, selected by (Müller, 2014). These short flare sources were proposed as candidates for possible neutrino emission for the ANTARES-project.
The Bayesian analysis of the twenty light curves show that the sources are variable. Four different types of sources according to their variation properties can be determined. There are some sources like 0521-365 (Fig. 17) and 1714-336 (Fig. 19) with a strong single peak in the light curve where the spectral components also change. Beside the single peak sources there also sources with more than one major peak like 0537-441 (Fig. 13) and 1454-354 (Fig. 40). In these sources the evolution of the spectral components shows a flux related behaviour. In addition to the strongly variable sources there are more quiet sources detected through the algorithm.

Some have just two blocks like 2204-540 (Fig. 44) or more blocks with little changes in the mean flux values like 2155-304 (Fig. 21). Nearly all sources have variations in their spectral index over time. Especially the sources with peaks show two examples for a relation between the spectral index Γ and the flux. The sources show that a correlated (e.g. 1714-336) and anti-correlated (e.g. 0521-365) behaviour can be seen.
A global evolution of the spectral properties is seen in Fig. 22; the upper limit of the spectral index decreases when the flux rises from $\Gamma = 3$ at a flux of $S_{1-100\,\mathrm{GeV}} = 0.1 \cdot 10^{-7}\,\mathrm{cm}^{-2}\mathrm{s}^{-1}$ to a spectral index below $\Gamma = 2$ over a flux of $S_{1-100\,\mathrm{GeV}} = 0.5 \cdot 10^{-7}\,\mathrm{cm}^{-2}\mathrm{s}^{-1}$. A similar evolution of the upper limit can not be seen, at low fluxes the spectral indices have large uncertainties due to less good fits of the single block spectra.

Many light curves (e.g. 1325-558 and 1714-336) have a large number of upper limits, which are neglected in the Bayesian analysis. To avoid a small number of bins per light curve, some light curves are calculated in a larger energy range and without upper limits (Sec. 4.3) The results of the four sources show that a larger energy range reduces the upper limits and more blocks can be found with the algorithm. Not calculating the upper limits produces even more blocks, but some blocks exist only because of very small flux points in the light curves. The best method in sources with many upper limits is to enlarge the energy. If this is not enough the upper limit calculation should be switched off.
The results of the Bayesian analysis can be used to recalculate the light curve with respect to the change of the spectral index. The standard Fermi light curve is computed with a fixed spectral index over the whole time range of the light curve, but this not the reality of the spectral index evolution. Especially the recalculation of 0537-441 shows that the peak fluxes were calculated higher in the standard light curve and the peaks appear a bit smoother during the rise and decline (Fig. 29b). The method of recalculation is able to give better assessment of upper limits for sources where the upper limits are about one magnitude higher than the highest computed flux point. In the cases of 1325-558 and 1714-336 some small improvements could be reached in the recalculated light light curve, some upper limits were computed lower and a few flux points could be calculated in addition. Especially for 1325-558 the Bayesian block representation was improved.

In this thesis it is shown that the Bayesian analysis of Fermi light curves is a good technique to analyse variations of light curves and spectral properties of given source samples. This method can also be applied to other wavelength bands to provide a Bayesian multi-wavelength light curve analysis in order to study multi-wavelength correlations and get a better picture of the whole AGN emission system itself.
Additionally, the Bayesian analysis demonstrated that the search for short flaring sources can be supported by Bayesian blocks, if a defined block size, e.g. two flux bins per block, is added as the second short criterion.
The Bayesian analysis is based only on the statistical issues concerning the input data and their given uncertainties.

Appendix

Light Curves

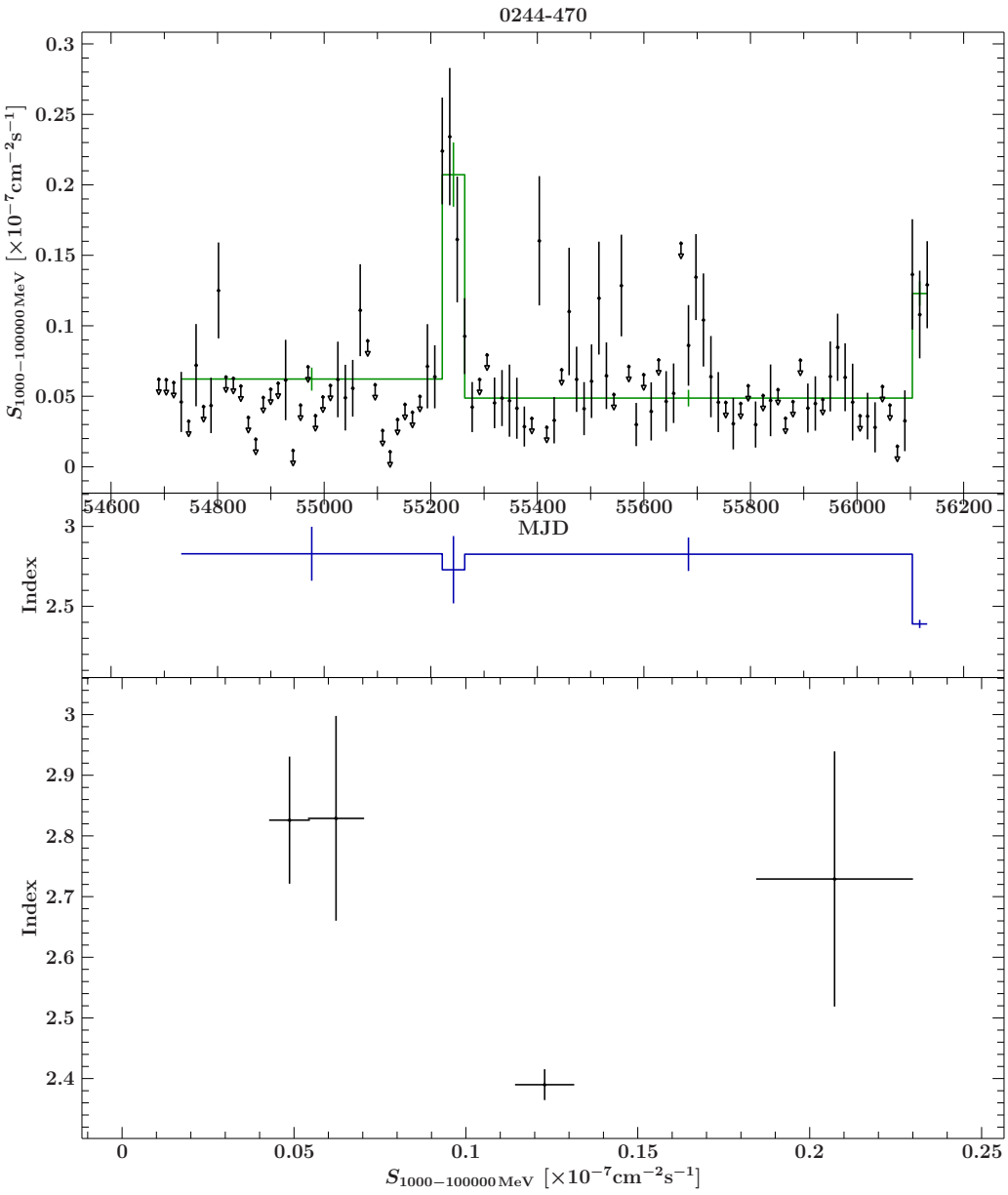

Figure 33: Upper panel: light curve of 0244-470 with the determined blocks (green). Mid panel: evolution of the spectral index over time resulted by the analysis of the block spectra. Lower panel: spectral index of the blocks plotted over their related mean flux of the block.

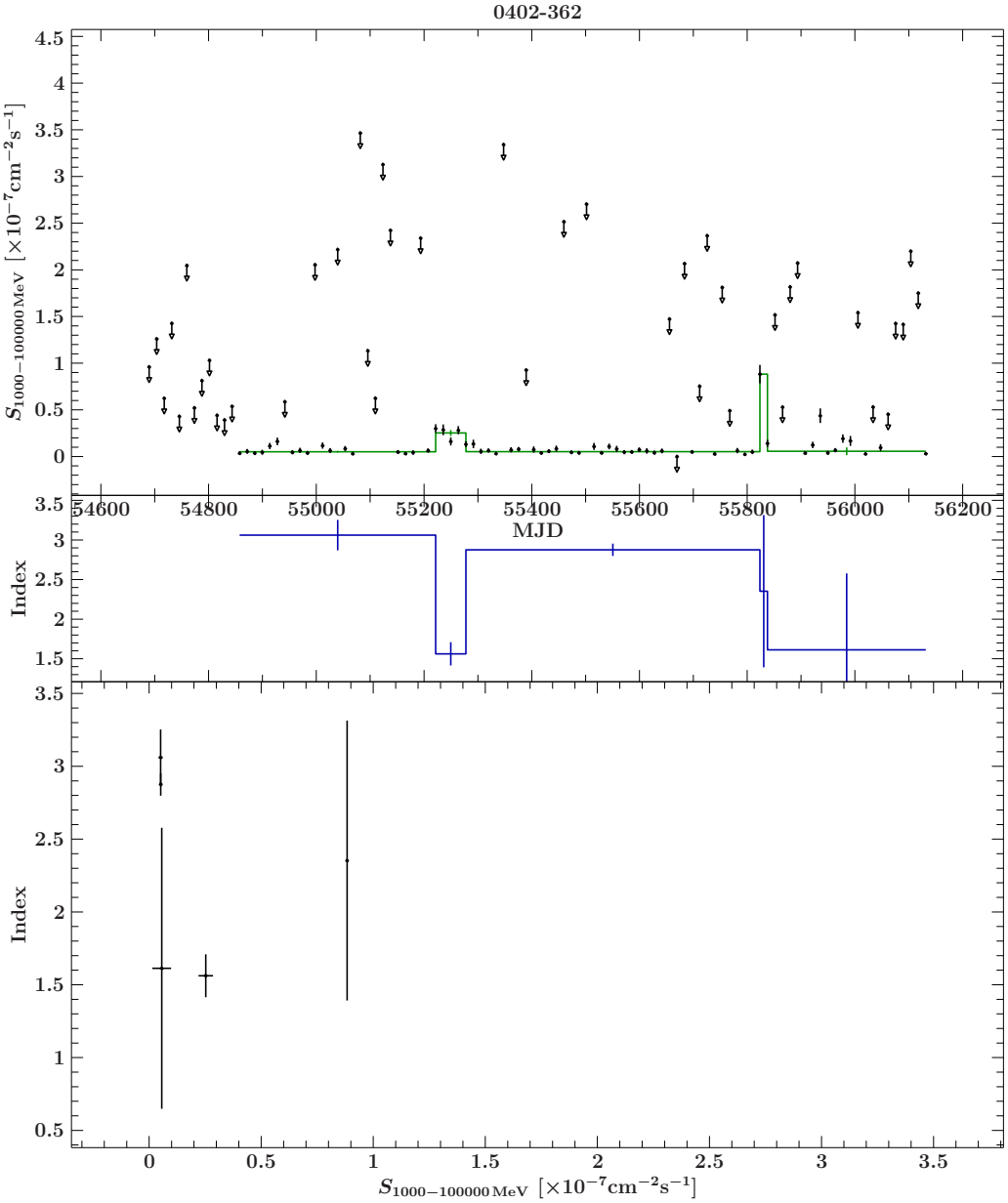

Figure 34: Upper panel: light curve of 0402-362 with the determined blocks (green). Mid panel: evolution of the spectral index over time resulted by the analysis of the block spectra. Lower panel: spectral index of the blocks plotted over their related mean flux of the block.

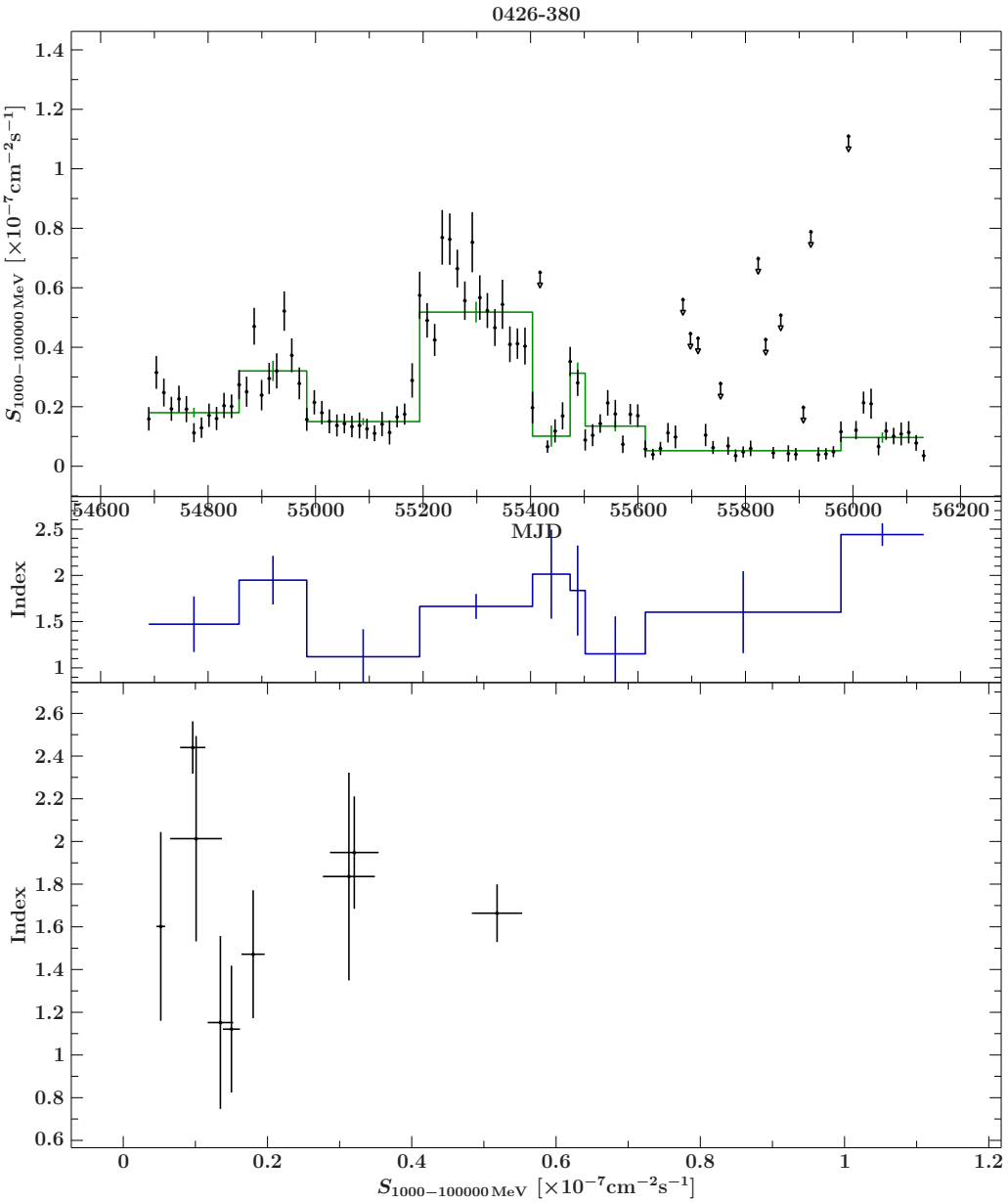

Figure 35: Upper panel: light curve of 0426-380 with the determined blocks (green). Mid panel: evolution of the spectral index over time resulted by the analysis of the block spectra. Lower panel: spectral index of the blocks plotted over their related mean flux of the block.

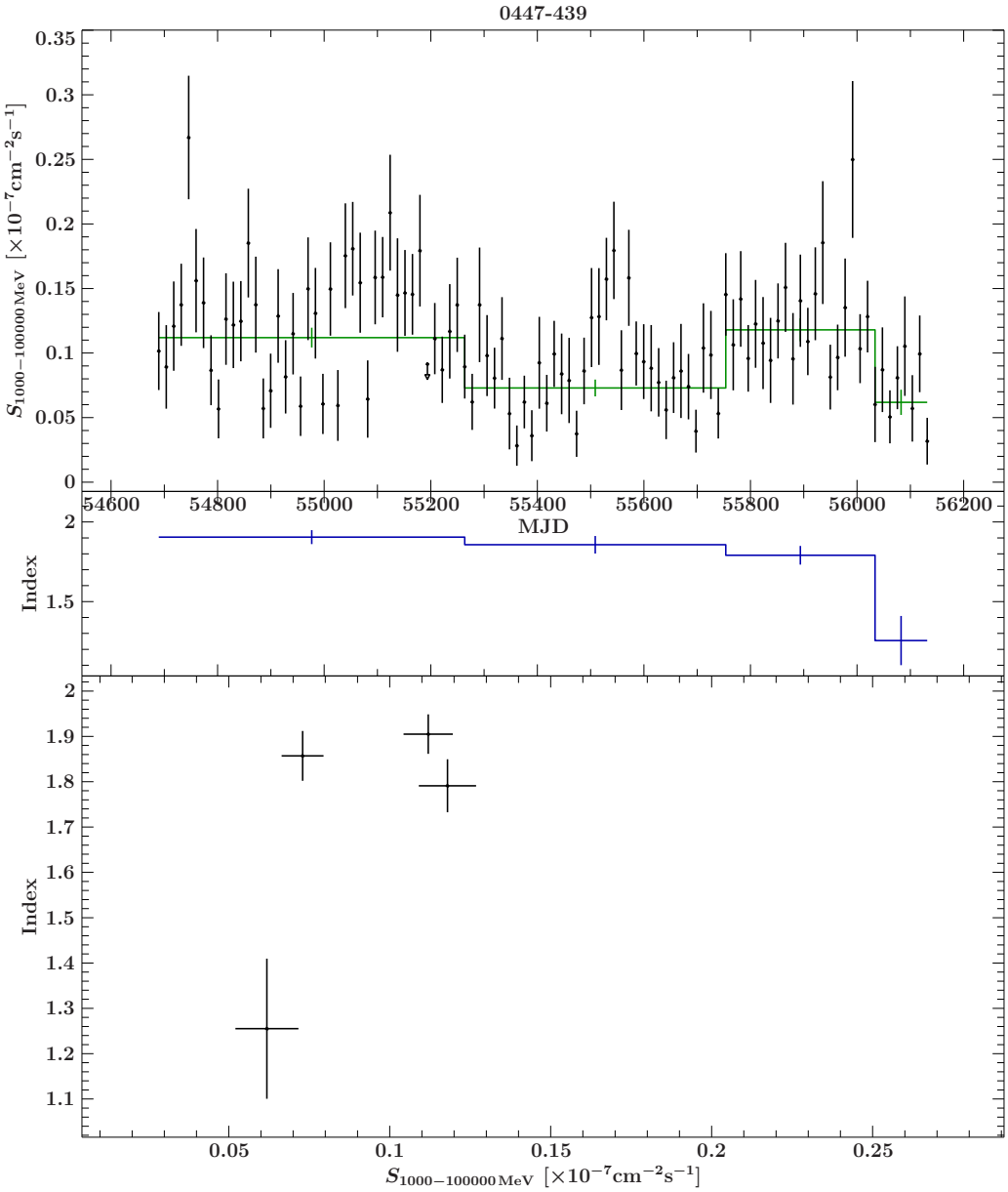

Figure 36: Upper panel: light curve of 0447-439 with the determined blocks (green). Mid panel: evolution of the spectral index over time resulted by the analysis of the block spectra. Lower panel: spectral index of the blocks plotted over their related mean flux of the block.

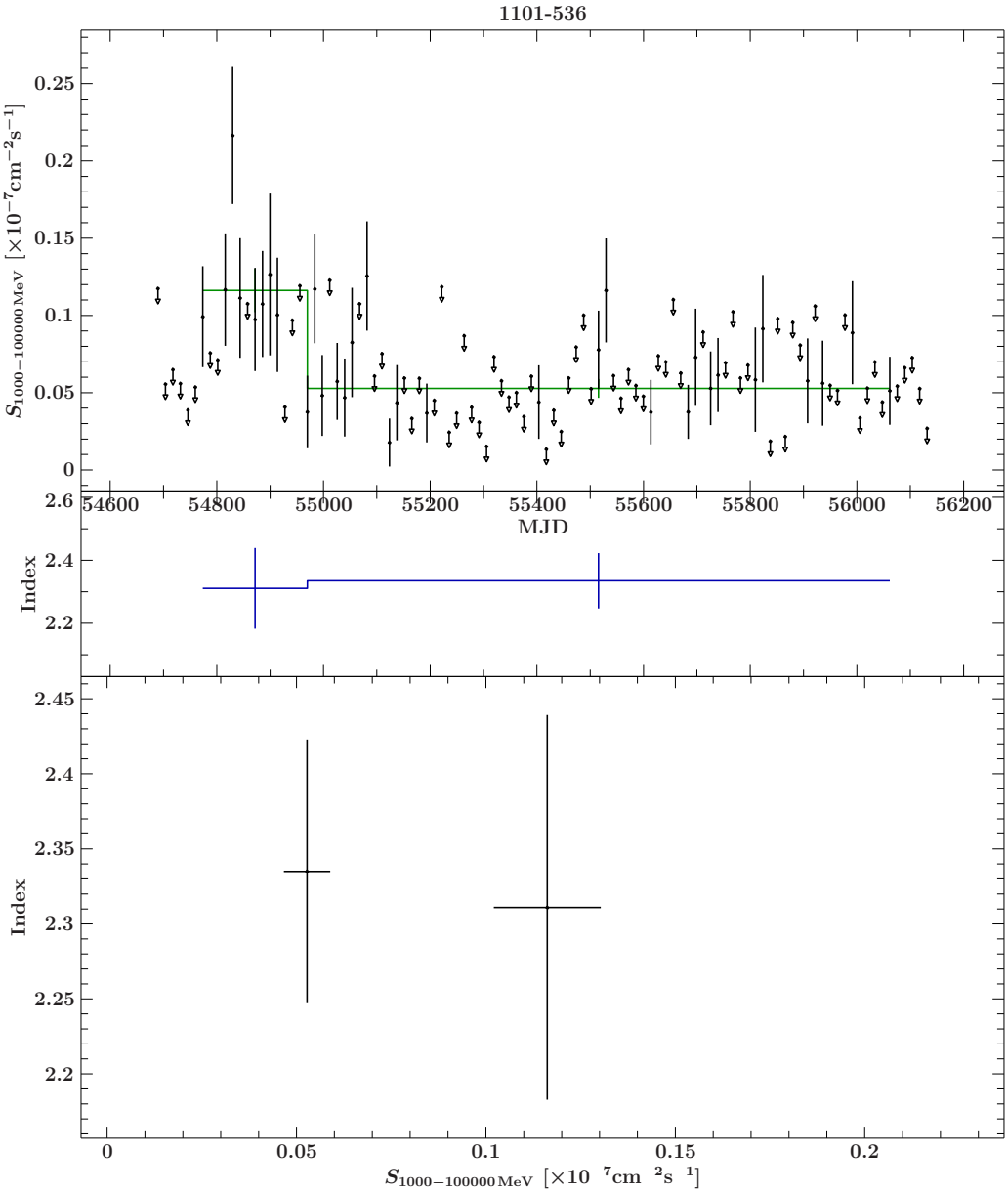

Figure 37: Upper panel: light curve of 1101-536 with the determined blocks (green). Mid panel: evolution of the spectral index over time resulted by the analysis of the block spectra. Lower panel: spectral index of the blocks plotted over their related mean flux of the block.

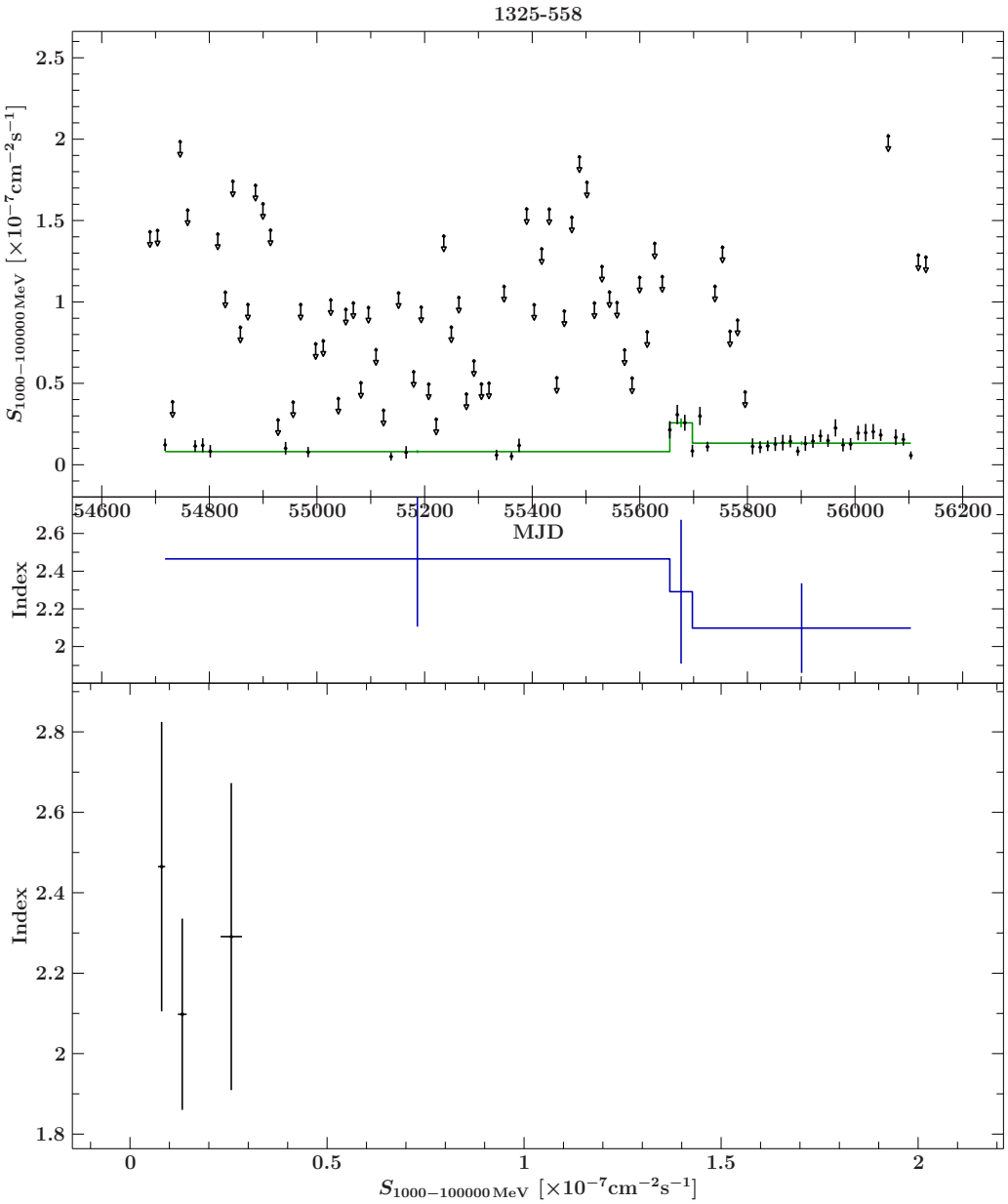

Figure 38: Upper panel: light curve of 1325-558 with the determined blocks (green). Mid panel: evolution of the spectral index over time resulted by the analysis of the block spectra. Lower panel: spectral index of the blocks plotted over their related mean flux of the block.

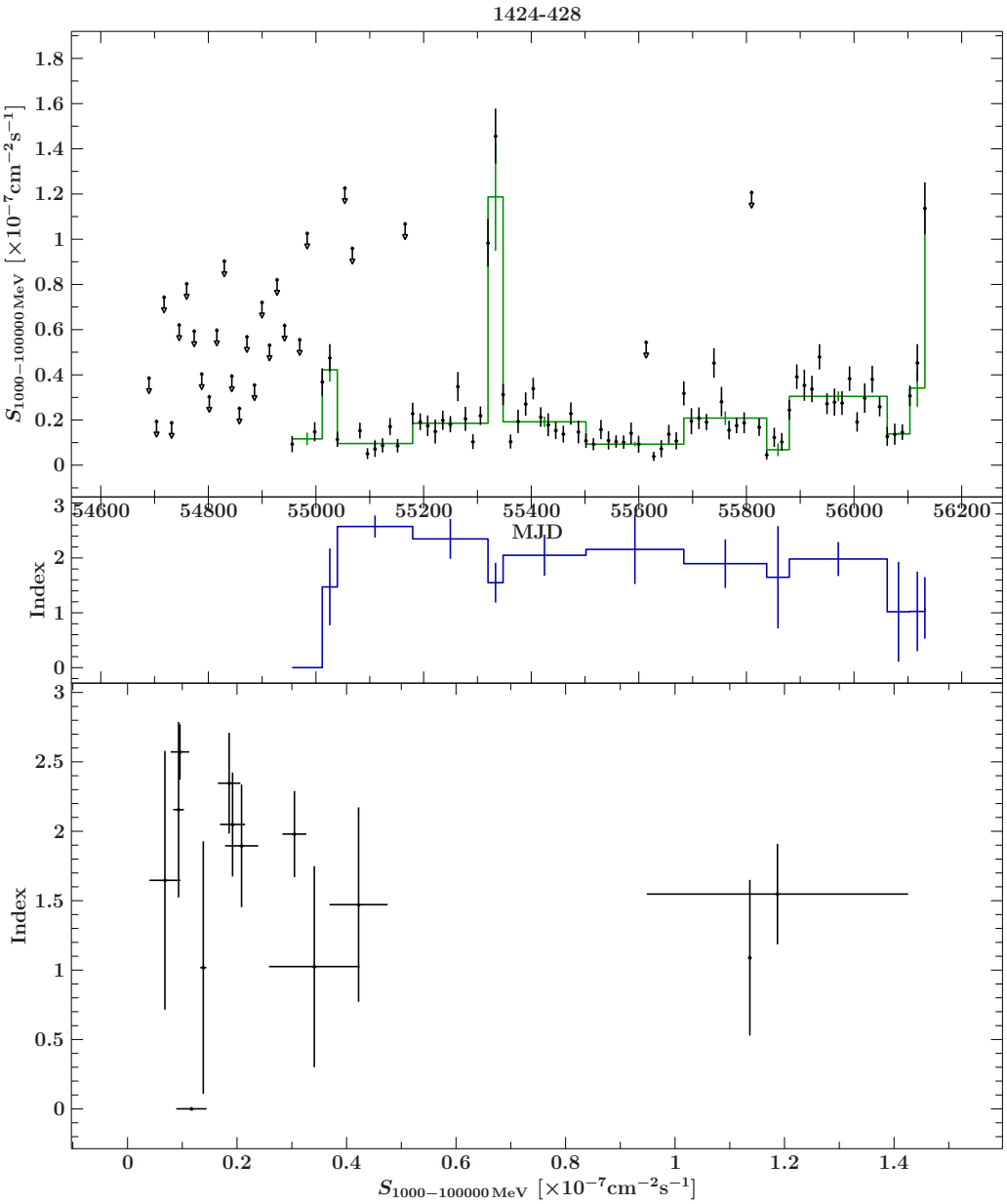

Figure 39: Upper panel: light curve of 1424-428 with the determined blocks (green). Mid panel: evolution of the spectral index over time resulted by the analysis of the block spectra. Lower panel: spectral index of the blocks plotted over their related mean flux of the block.

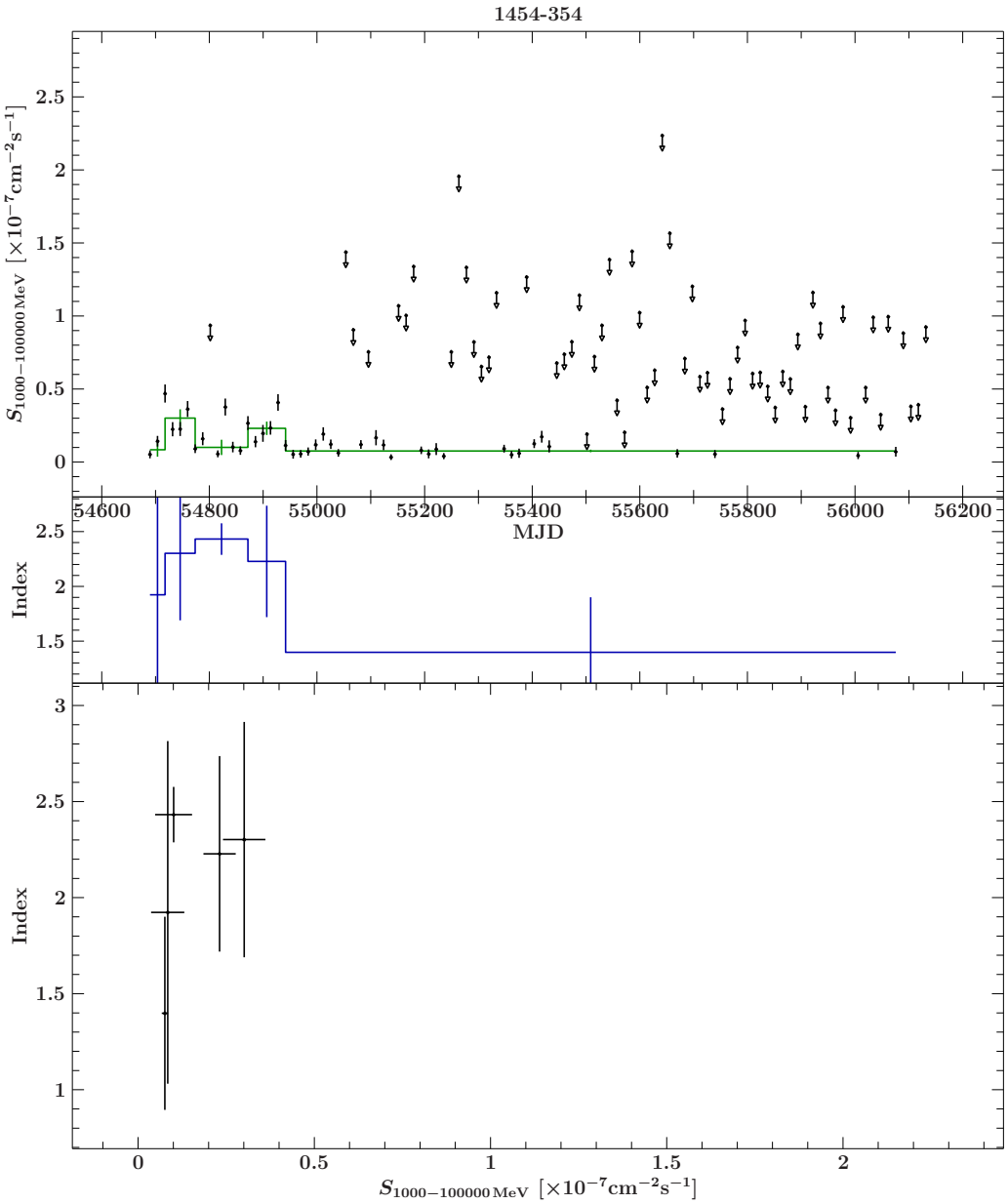

Figure 40: Upper panel: light curve of 1454-354 with the determined blocks (green). Mid panel: evolution of the spectral index over time resulted by the analysis of the block spectra. Lower panel: spectral index of the blocks plotted over their related mean flux of the block.

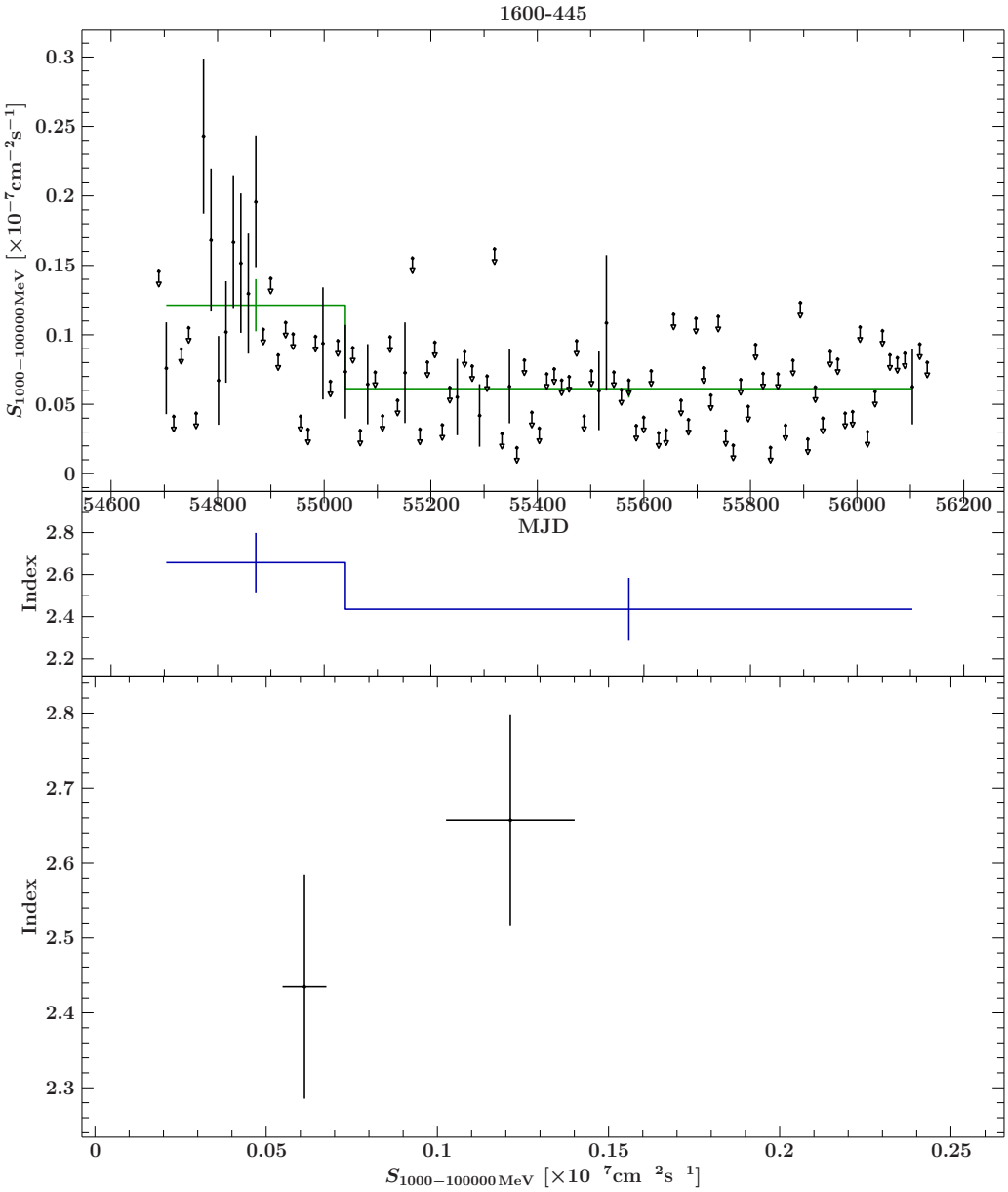

Figure 41: Upper panel: light curve of 1600-445 with the determined blocks (green). Mid panel: evolution of the spectral index over time resulted by the analysis of the block spectra. Lower panel: spectral index of the blocks plotted over their related mean flux of the block.

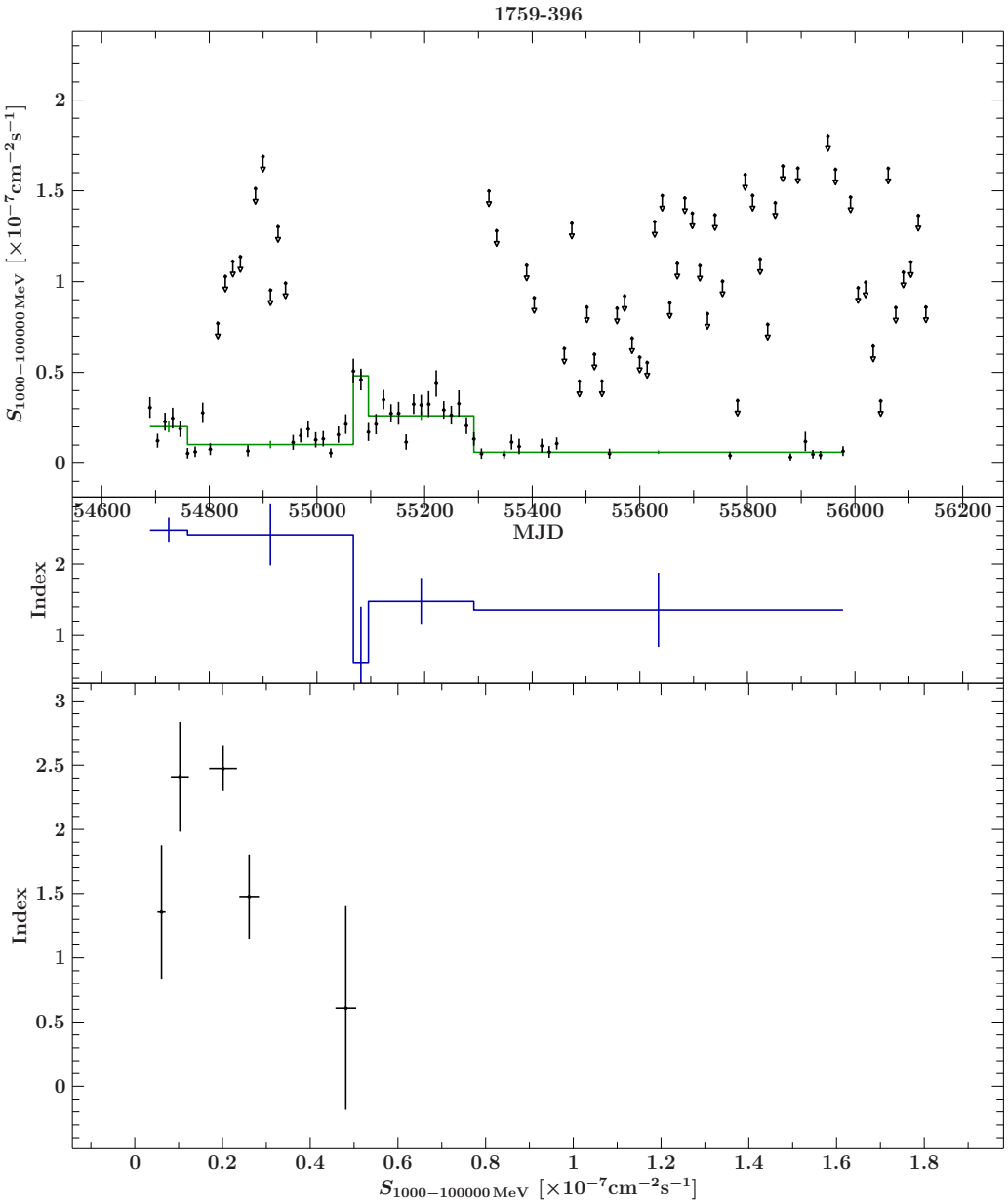

Figure 42: Upper panel: light curve of 1759-396 with the determined blocks (green). Mid panel: evolution of the spectral index over time resulted by the analysis of the block spectra. Lower panel: spectral index of the blocks plotted over their related mean flux of the block.

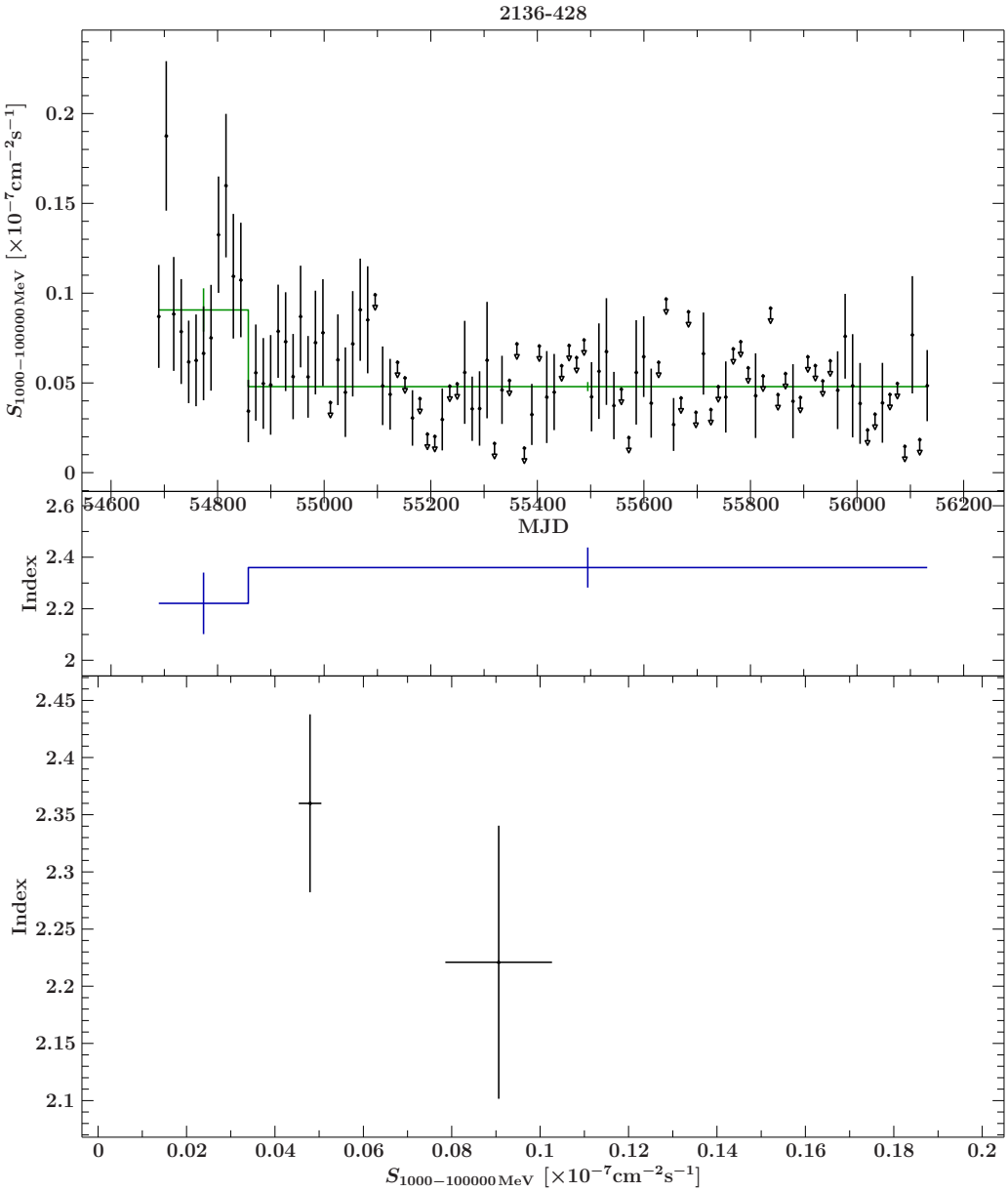

Figure 43: Upper panel: light curve of 2136-428 with the determined blocks (green). Mid panel: evolution of the spectral index over time resulted by the analysis of the block spectra. Lower panel: spectral index of the blocks plotted over their related mean flux of the block.

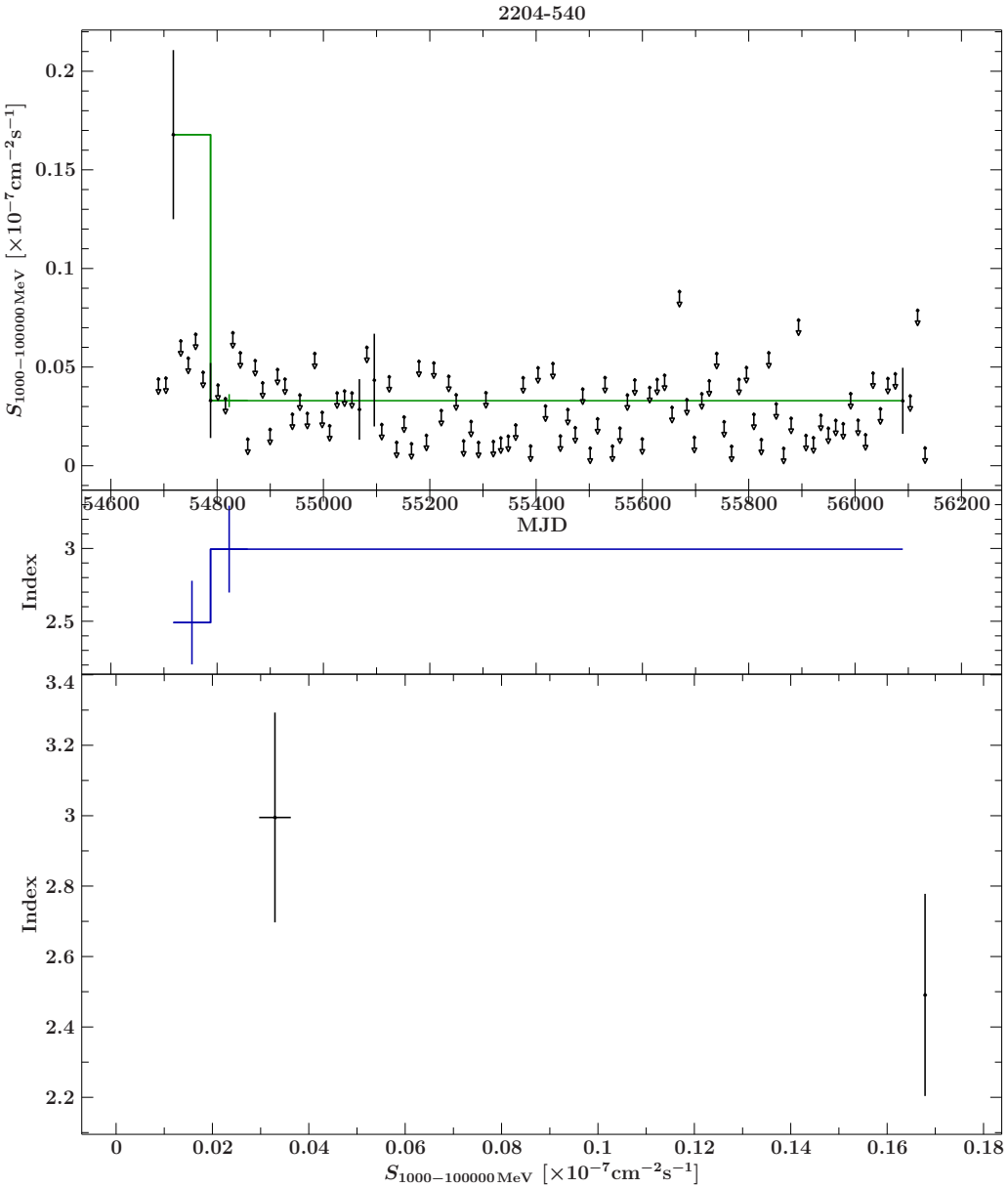

Figure 44: Upper panel: light curve of 2204-540 with the determined blocks (green). Mid panel: evolution of the spectral index over time resulted by the analysis of the block spectra. Lower panel: spectral index of the blocks plotted over their related mean flux of the block.

References

R. Antonucci. Unified models for active galactic nuclei and quasars. *Annual Review of Astronomy and Astrophysics*, 31:473–521, 1993. doi: 10.1146/annurev.aa.31.090193.002353.

W. B. Atwood, A. A. Abdo, M. Ackermann, W. Althouse, B. Anderson, M. Axelsson, L. Baldini, J. Ballet, D. L. Band, G. Barbiellini, and et al. The Large Area Telescope on the Fermi Gamma-Ray Space Telescope Mission. *The Astrophysical Journal*, 697:1071–1102, June 2009. doi: 10.1088/0004-637X/697/2/1071.

W. Bethe, H. & Heitler. On the stopping of fast particles and on the creation of positive electrons. *Proc. R. Soc. Lon. A*, 1934.

G. R. Blumenthal and R. J. Gould. Bremsstrahlung, Synchrotron Radiation, and Compton Scattering of High-Energy Electrons Traversing Dilute Gases. *Reviews of Modern Physics*, 42: 237–271, 1970. doi: 10.1103/RevModPhys.42.237.

M. Böck. *Observations of Active Galactic Nuclei from Radio to Gamma-rays*. PhD thesis, Friedrich-Alexander-Universität Erlangen-Nürnberg, 2012.

M. Boettcher. *Relativistic Jets from Active Galactic Nuclei*. Wiley, 2012.

S. Buson, F. Longo, S. Larsson, S. Cutini, J. Finke, S. Ciprini, R. Ojha, F. D'Ammando, D. Donato, D. J. Thompson, R. Desiante, D. Bastieri, S. Wagner, M. Hauser, L. Fuhrmann, M. Dutka, C. Müller, M. Kadler, E. Angelakis, J. A. Zensus, J. Stevens, J. M. Blanchard, P. G. Edwards, J. E. J. Lovell, M. A. Gurwell, A. E. Wehrle, and A. Zook. Unusual flaring activity in the blazar PKS 1424-418 during 2008-2011. *Astronomy & Astrophysics*, 569:A40, Sept. 2014. doi: 10.1051/0004-6361/201423367.

R. Chatterjee, K. Nalewajko, and A. D. Myers. Implications of the Anomalous Outburst in the Blazar PKS 0208-512. *The Astrophysical Journal Letters*, 771:L25, July 2013. doi: 10.1088/2041-8205/771/2/L25.

A. H. Compton. A quantum theory of the scattering of x-rays by light elements. *Phys. Rev.*, 21:483–502, May 1923. doi: 10.1103/PhysRev.21.483. URL `http://link.aps.org/doi/10.1103/PhysRev.21.483`.

H. D. Curtis. Descriptions of 762 Nebulae and Clusters Photographed with the Crossley Reflector. *Publications of Lick Observatory*, 13:9–42, 1918.

B. L. Fanaroff and J. M. Riley. The morphology of extragalactic radio sources of high and low luminosity. *Monthly Notice of the Royal Astronomical Society*, 167:31–36, May 1974.

E. A. Fath. The spectra of some spiral nebulae and globular star clusters. *Lick Observatory Bulletin*, 5:71–77, 1909. doi: 10.5479/ADS/bib/1909LicOB.5.71F.

H.E.S.S. Collaboration, A. Abramowski, F. Acero, F. Aharonian, A. G. Akhperjanian, G. Anton, A. Balzer, A. Barnacka, U. Barres de Almeida, Y. Becherini, and et al. A multiwavelength view of the flaring state of PKS 2155-304 in 2006. *Astronomy & Astrophysics*, 539:A149, Mar. 2012. doi: 10.1051/0004-6361/201117509.

B. Jackson, J. D. Scargle, D. Barnes, S. Arabhi, A. Alt, P. Gioumousis, E. Gwin, P. Sangtrakulcharoen, L. Tan, and T. T. Tsai. An Algorithm for Optimal Partitioning of Data on an Interval. *ArXiv Mathematics e-prints*, Sept. 2003.

H. Karttunen. *Fundamental Astronomy 5th Edition*. Springer, Berlin Heidelberg New York, 2007.

E. Y. Khachikian and D. W. Weedman. An atlas of Seyfert galaxies. *The Astrophysical Journal*, 192:581–589, Sept. 1974. doi: 10.1086/153093.

F. Krauß, M. Kadler, K. Mannheim, R. Schulz, J. Trüstedt, J. Wilms, R. Ojha, E. Ros, G. Anton, W. Baumgartner, T. Beuchert, J. Blanchard, C. Bürkel, B. Carpenter, T. Eberl, P. G. Edwards, D. Eisenacher, D. Elsässer, K. Fehn, U. Fritsch, N. Gehrels, C. Gräfe, C. Großberger, H. Hase, S. Horiuchi, C. James, A. Kappes, U. Katz, A. Kreikenbohm, I. Kreykenbohm, M. Langejahn, K. Leiter, E. Litzinger, J. E. J. Lovell, C. Müller, C. Phillips, C. Plötz, J. Quick, T. Steinbring, J. Stevens, D. J. Thompson, and A. K. Tzioumis. TANAMI blazars in the IceCube PeV-neutrino fields. *Astronomy & Astrophysics*, 566:L7, June 2014. doi: 10.1051/0004-6361/201424219.

J. H. Krolik. *Active Galactic Nuclei : From the Central Black Hole to the Galactic Environment*. Princeton University Press, Princeton, 1999.

K. Mannheim, T. Stanev, and P. L. Biermann. Neutrinos from flat-spectrum radio quasars. *Astronomy & Astrophysics*, 260:L1–L3, July 1992.

A. Markowitz, M. Krumpe, and R. Nikutta. First Statistical Tests for Clumpy Tori Models: Constraints from RXTE monitoring of Seyfert AGN. In *The X-ray Universe 2014*, page 129, July 2014.

A. P. Marscher and W. K. Gear. Models for high-frequency radio outbursts in extragalactic sources, with application to the early 1983 millimeter-to-infrared flare of 3C 273. *The Astrophysical Journal*, 298:114–127, Nov. 1985. doi: 10.1086/163592.

T. A. Matthews and A. R. Sandage. Optical Identification of 3c 48, 3c 196, and 3c 286 with Stellar Objects. *The Astrophysical Journal*, 138:30, July 1963. doi: 10.1086/147615.

J. R. Mattox, D. L. Bertsch, J. Chiang, B. L. Dingus, S. W. Digel, J. A. Esposito, J. M. Fierro, R. C. Hartman, S. D. Hunter, G. Kanbach, D. A. Kniffen, Y. C. Lin, D. J. Macomb, H. A. Mayer-Hasselwander, P. F. Michelson, C. von Montigny, R. Mukherjee, P. L. Nolan, P. V. Ramanamurthy, E. Schneid, P. Sreekumar, D. J. Thompson, and T. D. Willis. The Likelihood Analysis of EGRET Data. *The Astrophysical Journal*, 461:396, Apr. 1996. doi: 10.1086/177068.

C. Meegan, G. Lichti, P. N. Bhat, E. Bissaldi, M. S. Briggs, V. Connaughton, R. Diehl, G. Fishman, J. Greiner, A. S. Hoover, A. J. van der Horst, A. von Kienlin, R. M. Kippen, C. Kouveliotou, S. McBreen, W. S. Paciesas, R. Preece, H. Steinle, M. S. Wallace, R. B. Wilson, and C. Wilson-Hodge. The Fermi Gamma-ray Burst Monitor. *The Astrophysical Journal*, 702:791, Sept. 2009. doi: 10.1088/0004-637X/702/1/791.

A. Mücke and R. J. Protheroe. A proton synchrotron blazar model for flaring in Markarian 501. *Astroparticle Physics*, 15:121–136, Mar. 2001. doi: 10.1016/S0927-6505(00)00141-9.

C. Müller. *High-Resolution Observations of Active Galactic Nuclei in the Southern Hemisphere*. PhD thesis, Friedrich-Alexander-Universität Erlangen-Nürnberg, 2014.

C. Müller, F. Krauss, M. Kadler, J. Trüstedt, R. Ojha, E. Ros, J. Wilms, M. Böck, M. Dutka, B. Carpenter, and the TANAMI collaboration. The TANAMI Program: Southern-Hemisphere AGN on (Sub-)parsec Scales. *ArXiv e-prints*, Jan. 2013.

R. Nesci, G. Tosti, T. Pursimo, R. Ojha, and M. Kadler. Near-infrared and gamma-ray monitoring of TANAMI gamma-ray bright sources. *Astronomy & Astrophysics*, 555:A2, July 2013. doi: 10.1051/0004-6361/201321094.

P. L. Nolan, A. A. Abdo, M. Ackermann, M. Ajello, A. Allafort, E. Antolini, W. B. Atwood, M. Axelsson, L. Baldini, J. Ballet, and et al. Fermi Large Area Telescope Second Source Catalog. *The Astrophysical Journal Supplement*, 199:31, Apr. 2012. doi: 10.1088/0067-0049/199/2/31.

R. Ojha, M. Kadler, M. Boeck, F. Hungwe, C. Mueller, J. Wilms, E. Ros, and the TANAMI Team. The TANAMI Program. *ArXiv e-prints*, June 2010.

B. M. Peterson. *AN INTRODUCTION TO ACTIVE GALACTIC NUCLEI*. CAMBRIDGE UNIVERSITY PRESS, 1997.

E. E. Salpeter. Accretion of Interstellar Matter by Massive Objects. *The Astrophysical Journal*, 140:796–800, Aug. 1964. doi: 10.1086/147973.

J. D. Scargle. Studies in Astronomical Time Series Analysis. V. Bayesian Blocks, a New Method to Analyze Structure in Photon Counting Data. *The Astrophysical Journal*, 504:405–418, Sept. 1998. doi: 10.1086/306064.

J. D. Scargle, J. P. Norris, B. Jackson, and J. Chiang. Studies in Astronomical Time Series Analysis. VI. Bayesian Block Representations. *The Astrophysical Journal*, 764:167, Feb. 2013. doi: 10.1088/0004-637X/764/2/167.

M. Schmidt. 3C 273 : A Star-Like Object with Large Red-Shift. *Nature*, 197:1040, Mar. 1963. doi: 10.1038/1971040a0.

C. K. Seyfert. Nuclear Emission in Spiral Nebulae. *The Astrophysical Journal*, 97:28, Jan. 1943. doi: 10.1086/144488.

C. M. Urry and P. Padovani. Unified Schemes for Radio-Loud Active Galactic Nuclei. *Publications of the Astronomical Society of the Pacific*, 107:803, Sept. 1995. doi: 10.1086/133630.

L. Woltjer. Emission Nuclei in Galaxies. *The Astrophysical Journal*, 130:38, July 1959. doi: 10.1086/146694.

Acknowledgement

At first i would like to thank my supervisors Jörn Wilms and Matthias Kadler for the opportunity and the support to write my thesis in the field of astrophysics. I appreciate Felica Krauß and Cornelia Müller for helping me with the Fermi/LAT analysis and helpful advises.
I also thank the people of the Remeis observatory for the wonderful pleasant and inspiring environment. The same applies to the working group of Matthias Kadler in Würzburg.
I would like to say 'thank you' to my friends and family, especially my parents, for their support during this thesis and my whole study.

Erklärung

Hiermit bestätige ich, dass ich diese Arbeit selbstständig und nur unter Verwendung der angegebenen Hilfsmittel angefertigt habe.

Erlangen, den 23. Januar 2015

Christoph Bürkel